Winter 1993

Kinetics and mechanism of iron oxidation in apoferritin

Shujun Sun
University of New Hampshire, Durham

Order Number 9420576

Kinetics and mechanism of iron oxidation in apoferritin

Sun, Shujun, Ph.D.

University of New Hampshire, 1993

U·M·I

300 N. Zeeb Rd.
Ann Arbor, MI 48106

KINETICS AND MECHANISM OF IRON OXIDATION IN APOFERRITIN

By

SHUJUN SUN
B.S., Zhengzhou University, 1981
M.S., Zhengzhou University, 1984

DISSERTATION

Submitted to the University of New Hampshire
in Partial Fulfillment of
the Requirements for the Degree of

Doctor of Philosophy

in

Chemistry

December, 1993

This Dissertation has been examined and approved.

Dissertation director, N. Dennis Chasteen
Professor of Chemistry

Howard R. Mayne
Associate Professor of Chemistry

Thomas M. Laue,
Associate Professor of Biochemistry

Kenneth. K. Andersen, Professor of Chemistry

W. Rudolf Seitz, Professor of Chemistry

November 22, 1993
Date

DEDICATION

To my parents for their love.

To my beloved son, Kyle.

ACKNOWLEDGEMENTS

I would like to take this opportunity to express my gratitude to those who have been involved in my graduate study and thesis research at UNH. First and foremost, my deepest appreciation goes to Dr. N. Dennis Chasteen for his support, innovative ideas and expert professional guidance, as well as for his invaluable help in the preparation of the present thesis. Thanks to John Grady for his constant technical help and valuable suggestions throughout these years. I am grateful to Pam Proulx-curry for her enthusiastic assistance in the performance of the liquid helium EPR experiments. I also benefited a lot from many conversations with her. The encouragement and understanding of Yu Chen Barret, Stephen Hattan and Wenge Wang during some difficult times are very much appreciated. My gratitude also goes to Kathleen S. Gallagher for her assistance and time in the use of the Bruker NMR. In addition, many thanks go to Dr. Howard R. Mayne for his patient instruction and advice. Also, thanks to Xiaoyong Sun for helping me come to UNH. Finally, I am deeply indebted to Ed Wong since he has been so supportive, understanding and patient all this time.

I wish to thank Dr. Paolo Arosio and Dr. Sonia Levi for providing some of the samples for my thesis work.

TABLE OF CONTENTS

LIST OF TABLES

LIST OF FIGURES

ABBREVIATIONS

A2	rHF with the nucleation site mutated (E61A, E64A, E67A)
222	rHF with the ferroxidase site mutated (E62K, H65G, E27A)
DMSO	dimethylsulfoxide
EPPS	N-(2-hydroxyehtyl)piperazine-N'-3-propane sulfonic acid
EPR	electron paramagnetic resonance
ESEEM	electron spin echo envelope modulation
HEPES	4-(2-hydroxyethyl)-1-piperazineethanesulfonic acid
HLF	human liver ferritin
HoSF	horse spleen ferritin
MES	2-(N-morpholino)ethanesulfonic acid
MOPS	3-(N-morpholino)-propanesulfonic acid
NTA	nitrilotriacetate
PAGE	polyacrylamide gel electrophoresis
rHF	recombinant human H-chain apoferritin
rLF	recombinant human L-chain apoferritin
S1	rHF with both the ferroxidase and nucleation sites mutated (E62K, H65G, E27A, E61A, E67A, D42A, K86Q)
SDS	sodium dodecyl sulfate
SOD	superoxide dismutase
SSP	sheep spleen ferritin
TGA	thioglycolic acid

ABSTRACT

KINETICS AND MECHANISM OF IRON OXIDATION
IN APOFERRITIN

By

Shujun Sun
University of New Hampshire, December, 1993

The enzymatic activity of horse spleen apoferritin in iron(II) oxidation was examined using microelectrode oximetry. The reaction exhibits saturation kinetics with respect to both Fe^{2+} and O_2. The kinetics are discussed in terms of two mechanisms, one involving monomeric and the other dimeric iron protein complexes. In both instances Fe^{2+} oxidation occurs in 1-electron steps. At increments of 50 Fe^{2+}/protein or less, all of the iron is oxidized via the protein ferroxidase site(s), independent of the amount of core already present. The results of these studies emphasize the role of the protein shell in all phases of core growth.

A detailed study of the kinetics of iron(II) oxidation by molecular oxygen in natural and recombinant human apoferritins has also been carried out to understand the ferroxidase activity of the protein shell and the function of the H and L subunits during iron uptake in ferritins.

Zn^{2+} was shown to be a noncompetitive inhibitor of Fe^{2+} oxidation in rHF but a mixed inhibitor in HLF. These different forms of Zn^{2+} inhibition in the two proteins and the higher than expected activity of HLF based on its H-chain composition as well as differences in their enzyme kinetic parameters suggest that H and L-chains cooperate in modulating the ferroxidase activity of the apoferritin even though the L-subunit lacks a ferroxidase site itself.

Additionally, the intermediate species produced in the process of ferritin reconstitution from apoferritin, Fe^{2+} and dioxygen, have been investigated using fast-mixing and stir-mixing freeze-quench techniques and EPR spectroscopy. The intermediate species found include the previously defined monomeric Fe^{3+}-protein complex ($g'= 4.3$), the mixed-valence Fe^{2+}-Fe^{3+} intermediate ($g'= 1.87$) and the free radical, as well as a new radical with axial magnetic symmetry. Interaction of Fe^{2+} with the monomeric Fe^{3+}-protein complex was demonstrated. A 1:1 relationship between the monomeric Fe^{3+}-protein complex and the mixed-valence species was observed within the first second of reaction. The temperature-dependent properties of the new radical suggest that it may be associated with an iron center and may be a tryptophan-centered radical in the Fe^{2+}/Fe^{3+}/apoprotein system.

INTRODUCTION

IRON AND FERRITIN

Iron is the fourth most prevalent element and the most abundant transition metal in the Earth's crust (Subcommittee on Iron, 1979). Because of its abundance and versatile chemistry, iron has been an important element for almost all forms of life, whether they are prokaryote or eukaryote (Subcommittee on Iron, 1979). Iron is widely present in biological materials with various critical functions (Williams, 1982; 1985; 1989; 1990). Proteins containing iron-heme moieties are very important in metabolic functions. For example, hemoglobin and myoglobin can transport and store dioxygen (Judson, 1979; Voet, 1990), cytochrome P-450 functions to activate oxygen's insertion into a C-H bond (Mathews & van Holde, 1990), while cytochromes act as a conduit for electron transfer (Naqui et al., 1986). Other iron-containing proteins have enzymatic functions, such as ribonucleotide reductase, nitrogenase and aconitase as well as a group of proteins designated as iron flavoproteins (Subcommittee on Iron, 1979). Iron deficiency in a human body has serious deleterious effects, including specific tissue changes, metabolic defects, as well as functional abnormalities (Dallman, 1974; Subcommittee on Iron, 1979).

Iron occurs in water solution as inorganic or organic Fe^{2+} or Fe^{3+} complexes. The aqueous chemistries of Fe^{2+} and Fe^{3+} are quite different, especially in the neutral pH range. Fe^{2+}, being very unstable at pH 7, readily reacts with dioxygen to form the superoxide and subsequently the reactive hydroxyl radical (Burkitt & Gilbert, 1991; Crichton, 1979). These radicals can be damaging to cell constituents, like nucleic acids and proteins (Loeb et al., 1988). However, Fe^{3+}, the stable state of iron at physiological pH, forms insoluble rustlike hydrous ferric oxide, and is therefore not available for red blood cells or other biological processes.

The need for iron in many physiological processes, the low solubility of Fe^{3+} and the toxicity of excess intracellular iron in cells have led to the production of the iron scavenger protein ferritin in all eukaryotic cells (Clegg et al., 1980; Theil, 1987; 1989; Harrison et al., 1991). Ferritins possess several aspects of iron biochemistry. They sequester iron inside a protein shell as a hydrous ferric oxide mineral. Up to 4500 Fe atoms can be packed into one ferritin molecule. The ferritin molecule, therefore, solublizes an otherwise insoluble mineral. The physiological roles of ferritin are iron storage and detoxification. The iron stored in ferritin is available for other cells such as the synthesis of heme, while the excess intracellular iron can be detoxified and transferred by ferritin. For example, the iron generated from the old

red blood cells in a human body is detoxified and converted by macrophages to iron in ferritin where it is slowly delivered to apotransferrin. The iron carried by transferrin is then delivered to immature red cells. In this process ferritin helps to recycle iron from old red blood cells to young ones (Theil, 1987). Iron can also be released from ferritin and utilized by mitochondria for the synthesis of heme protein (Ulvik, 1982). In vivo, ferritin responds to fluctuations in incoming iron as well as to pathological changes in iron metabolism. The biosynthesis of both apoferritin and ferritin is known to be stimulated and regulated by iron (La Cross and Linder, 1980; Clegg, et al., 1980; Leibold & Guo, 1992).

STRUCTURE OF FERRITIN

Ferritin Shell

All ferritin molecules consist of a protein shell which is composed of 24 subunits. Figure 1A shows the three dimensional structure of horse spleen ferritin (Harrison et al., 1986). The shape of the ferritin is approximately spherical with inner and outer diameters of 76 and 122 Å, respectively (Harrison et al., 1991). The subunit consists of five α-helices in which four of them are composed of two antiparallel helix pairs (AB & CD). There is a short turn in each helix pair, but B and C are connected by a longer loop. The fifth helix E is located at one end of the four

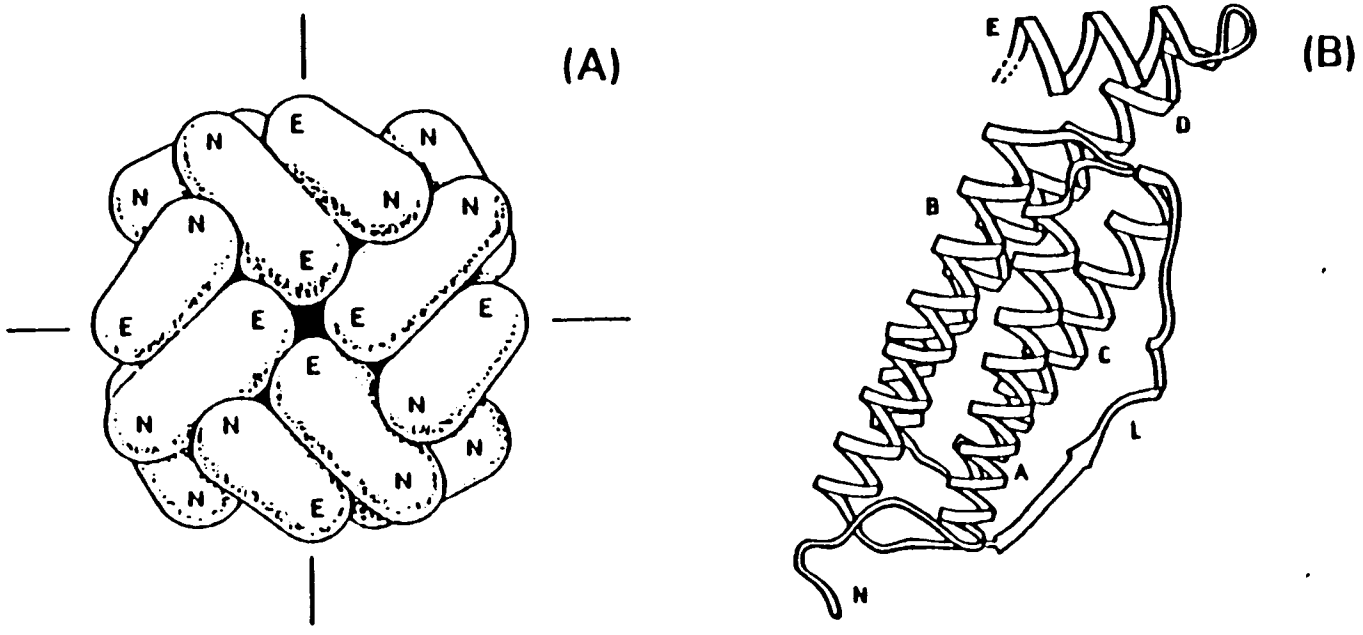

Figure 1. (A) Schematic representation of the horse spleen ferritin molecule, illustrating the symmetrical arrangement of 24 subunits. Each subunit is shown as a sausage-like building block, where N represents the N-terminal of the polypeptide chain and E shows the location of E helix in a subunit; (B) Ribbon diagram of the alpha carbon backbone of a subunit (Ford et al., 1984).

α-helix bundle (Fig. 1B). The protein coat is highly symmetrical with six 4-fold channels and eight 3-fold channels. The 3-fold channels formed by the interaction of three subunits are hydrophilic channels composed of carboxylate residues such as Asp-127 and Glu-130 (Fig. 2B). Metal-binding sites have been detected in these channels suggesting that the 3-fold channels might be important for transport of iron in and out of the protein (Rice et al., 1983; Harrison et al., 1985; 1986). The interactions of four subunits create six 4-fold channels with conserved hydrophobic amino acid side chains such as leucines (Fig. 2A).

The 24 subunits of the ferritin shell are not identical. Naturally occurring ferritins consist of mixtures of two different polypeptide chains, known as H and L, with apparent molecular weights of 21,000 and 19,000 g/mole respectively according to their relative mobilities on SDS-PAGE (Arosio et al., 1978). Each organ contains ferritins with a range of H and L compositions. For example, horse spleen ferritin consists of 84% L-subunit, while sheep spleen ferritin has only 34% L-subunit. Generally speaking, heart, brain and red cell ferritins are H rich, and liver and spleen ferritins are L rich (Arosio et al., 1978).

The H and L polypeptide chains of human ferritin contain 178 and 174 amino acid residues respectively. Variations in subunit primary structure, both within and

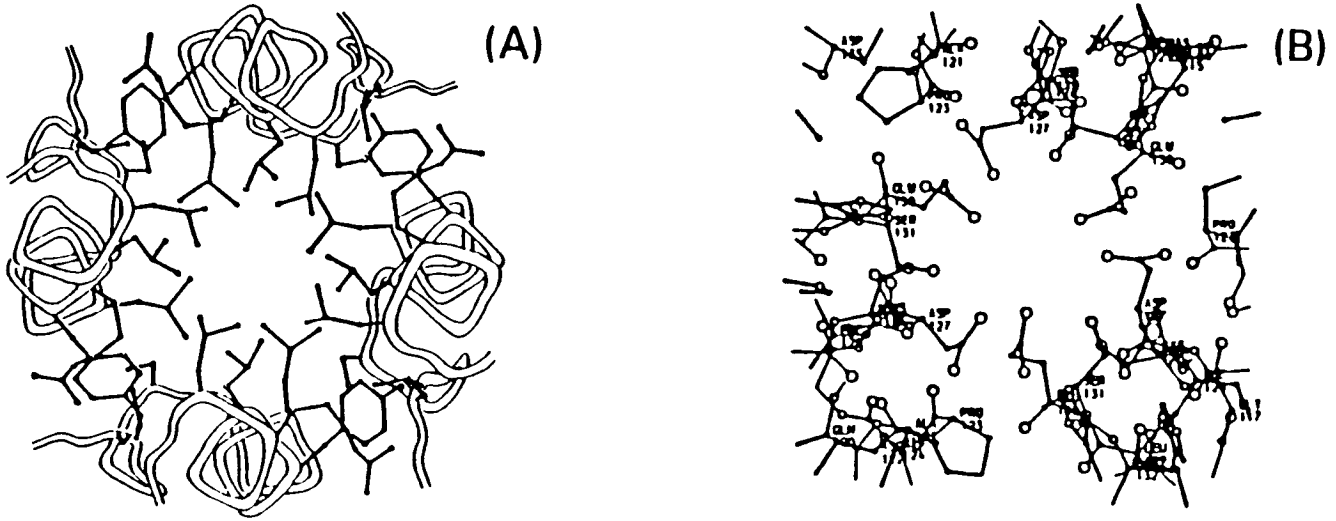

Figure 2. (A) Schematic diagram of horse spleen apoferritin in the region of a 4-fold axis. This channel is surrounded by 12 leucine residues; (B) View of the 3-fold axis which is lined with aspartates, glutamates, and serines (Ford et al., 1984).

between species, has been established. There is overall 80% homology in the amino acid sequences of human, rat and horse L-subunits, while the H-chains of human, rat and chicken show 90% identity (Harrison et al., 1985; Murray et al., 1987; Stevens et al., 1987). Nevertheless, the homology in amino acid sequence between H and L subunits from the same species is much smaller, approximately 55 % (Harrison et al., 1985).

Both L and H homopolymers fold and pack in the 24-mer protein shell in essentially the same way as heteropolymers do. Recently, the x-ray structure determination of the H homopolymer of human liver ferritin (Lawson et al., 1991), the recombinant rat L-ferritin (Thomas et al., 1988), as well as several site-directed mutants of the H-chain ferritin (Yewdall et al., 1990) have been completed. These ferritins have approximately the same conformation and quaternary structures as horse spleen ferritin. However, the 4-fold channel in human recombinant H-chain ferritin (rHF) is surrounded by four histidines (cavity side) and eight leucines (Fig. 3A) (Harrison et al., 1991) in contrast to horse spleen ferritin and rat L chain ferritin where they are surrounded by 12 leucines, rendering them more hydrophobic. The four histidines surrounding the 4-fold channel in rHF have been inferred as a metal ion binding site (Harrison et al., 1991). The three-fold channels of human rHF are hydrophilic in nature which is common to all ferritins.

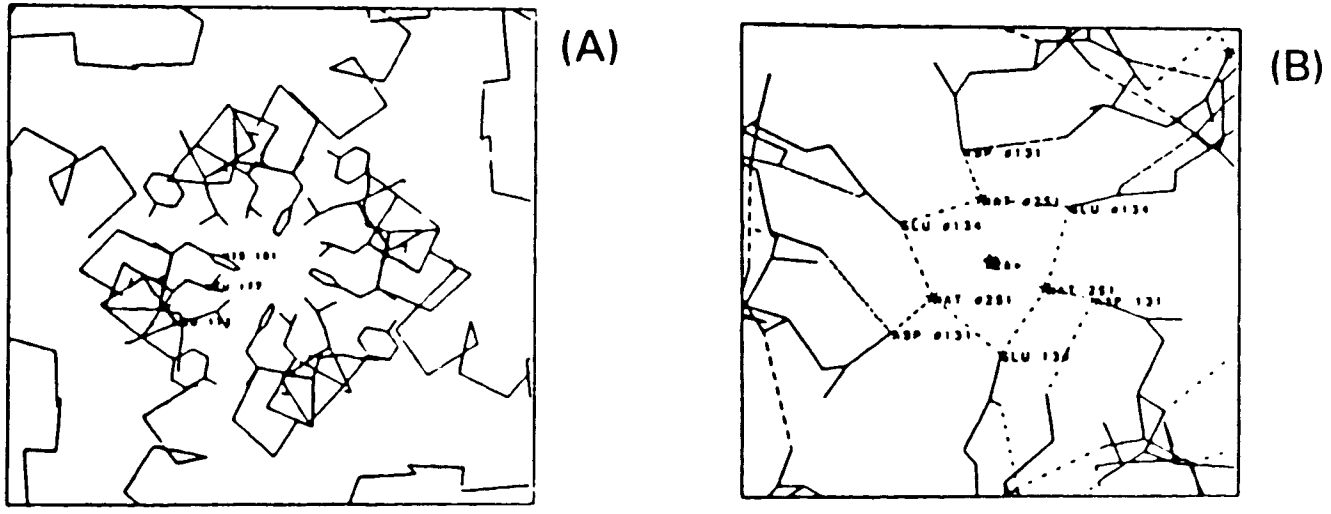

Figure 3. Stereo view of 4-fold channel (A), or a 3-fold channel (B) of human rHF. The 4-fold axis is lined with four histidines and eight leucines (A) Similar to horse spleen ferritin, the 3-fold axis of human rHF is surrounded by glutamates and aspartates (B) (Harrison et al., 1991).

Iron Core

Ferritin sequesters and stores iron inside its cavity. The iron core is in contact with the protein shell at several points between the iron-protein interface (Harrison & Lilley, 1989). The ferritin iron core is known to be the ferrihydrite mineral but with a molecular formula of $(FeOOH)_8(FeO.H_2PO_4)$ (Granick, 1946; Towe, 1981). The iron/phosphate ratios vary with different samples and with the sizes of the iron core. Higher proportions of phosphate have been found in horse spleen ferritin with low iron contents (Treffry & Harrison, 1978). The crystal structure of the horse spleen ferritin core is not uniform, containing both crystalline and disordered regions, probably caused by the uneven distribution of phosphate. Some areas of the crystal are typical of the mineral ferrihydrite, similar to the product obtained by heating ferric nitrate solutions (Theil, 1983). The disorder of the crystal structure increases with increasing the amount of phosphate (Treffry et al., 1978; 1987). The poor crystallinity associated with high phosphate content suggests that some of the hydroxyls of the ferric oxyhydroxide are replaced by phosphate. The role of phosphate in the mechanism of iron core formation has been investigated (Huang et al., 1993, Cheng & Chasteen, 1991). Phosphate, present on the surface of the mineral iron core, may function as an Fe^{2+} binding site and then promote Fe^{2+} oxidation to Fe^{3+} (Huang et al., 1993). While the ferritin shell provides nucleation sites in the early

stage of iron deposition, the role of the protein in the later stages of core development remains unclear.

Ferritin Reconstitution

Ferritin can be reconstituted from its apoferritin shell, Fe^{2+} and an oxidant such as dioxygen (Harrison et al., 1967). Attempts to reassemble ferritin from subunits and an iron core are not successful giving only apoferritin (Harrison & Gregory, 1968). Also, ferritin cannot be reconstituted from apoferritin and Fe^{3+} due to the strong tendency of Fe^{3+} to polymerize at physiological pH (Treffry & Harrison, 1979). Fe^{2+} oxidation and Fe^{3+} nucleation and hydrolysis are two basic steps forming the iron core of ferritin, and the protein shell is involved in both processes. Properties of the cores formed *in vitro* are very similar to native; therefore, the same mechanisms are likely to occur also *in vivo* (Theil, 1987).

Fe(II) Oxidation

Iron oxidation is catalyzed by the protein shell during the early stage of core formation (Macara et al., 1973; Bryce & Crichton, 1973; Bakker & Boyer, 1986). However, only the H-chains of ferritin are responsible for the catalytic activities of the protein shell. A ferroxidase site on the H subunit of human liver ferritin has been located by x-ray crystallography of rHF (Lawson et al., 1992) and further identified by site-directed mutagenesis

(Lawson et al., 1989). Figure 4A shows the position of the ferroxidase site which is located within a bundle of four α helices of a H-subunit with three amino acid residues as ligands: Glu-27 (helix A), Glu-62 and His-65 (helix B) (Lawson et al., 1992). A schematic picture of the ferroxidase center in H-chain as well as the equivalent region of the L-chain are illustrated in Figure 5 (Harrison, et al, 1991). It can be seen that the L-chain lacks a ferroxidase site. Although the L chain ferritin does not possess any ferroxidase activity, it is still capable of accumulating iron, though at a much slower rate than H-chain ferritin.

Fe^{3+} Nucleation

Currently, it is well known that the ferritin shell provides ferroxidase sites for Fe^{2+} oxidation. Thus, once the Fe^{3+} is formed, it should immediately leave the ferroxidase site for the nucleation site on the inner surface of the protein shell. The putative nucleation site includes three glutamate residues (Glu- 61, 64 and 67). The three ligands are conserved in both H and L subunits of ferritins from all mammalian species.

A variety of experimental observations have provided evidence for the involvement of the protein shell in Fe^{3+} core nucleation. These include (1) EPR signals of the Fe^{3+}-protein complex at low Fe/protein ratios and of the mixed-valence Fe^{2+}-Fe^{3+} dimer associated with the protein shell

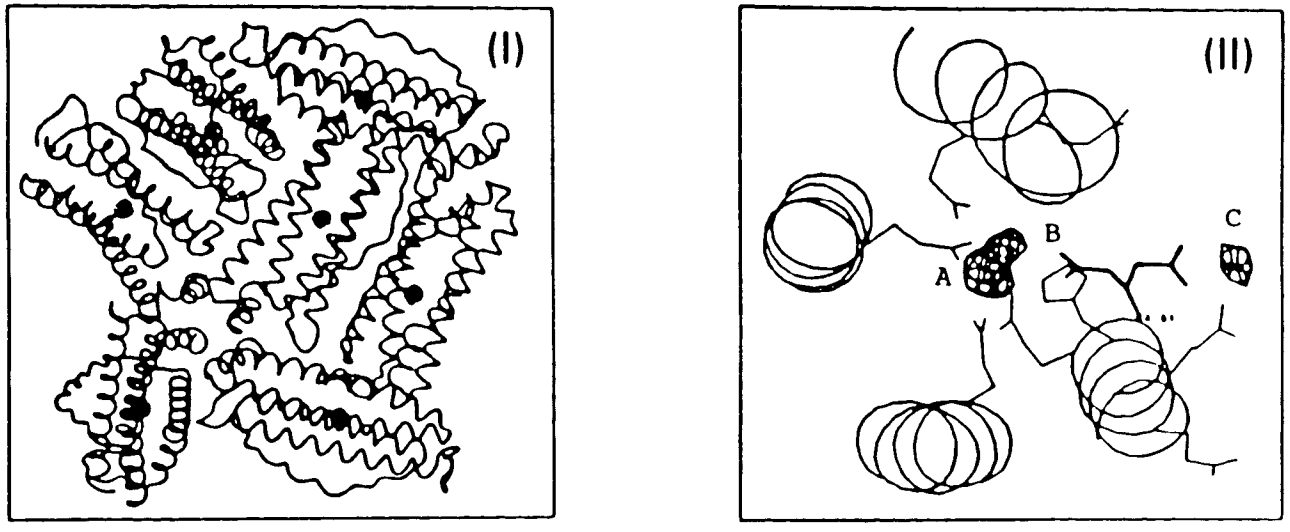

Figure 4. (I) partial ribbon diagram of the outer surface of human rHF. The spheres represent the ferroxidase sites which are located roughly at the central positions of the subunit; (II) Stereo view of the center of a subunit of human rHF illustrating the three metal ion binding sites A, B, C (Lawson et al., 1991).

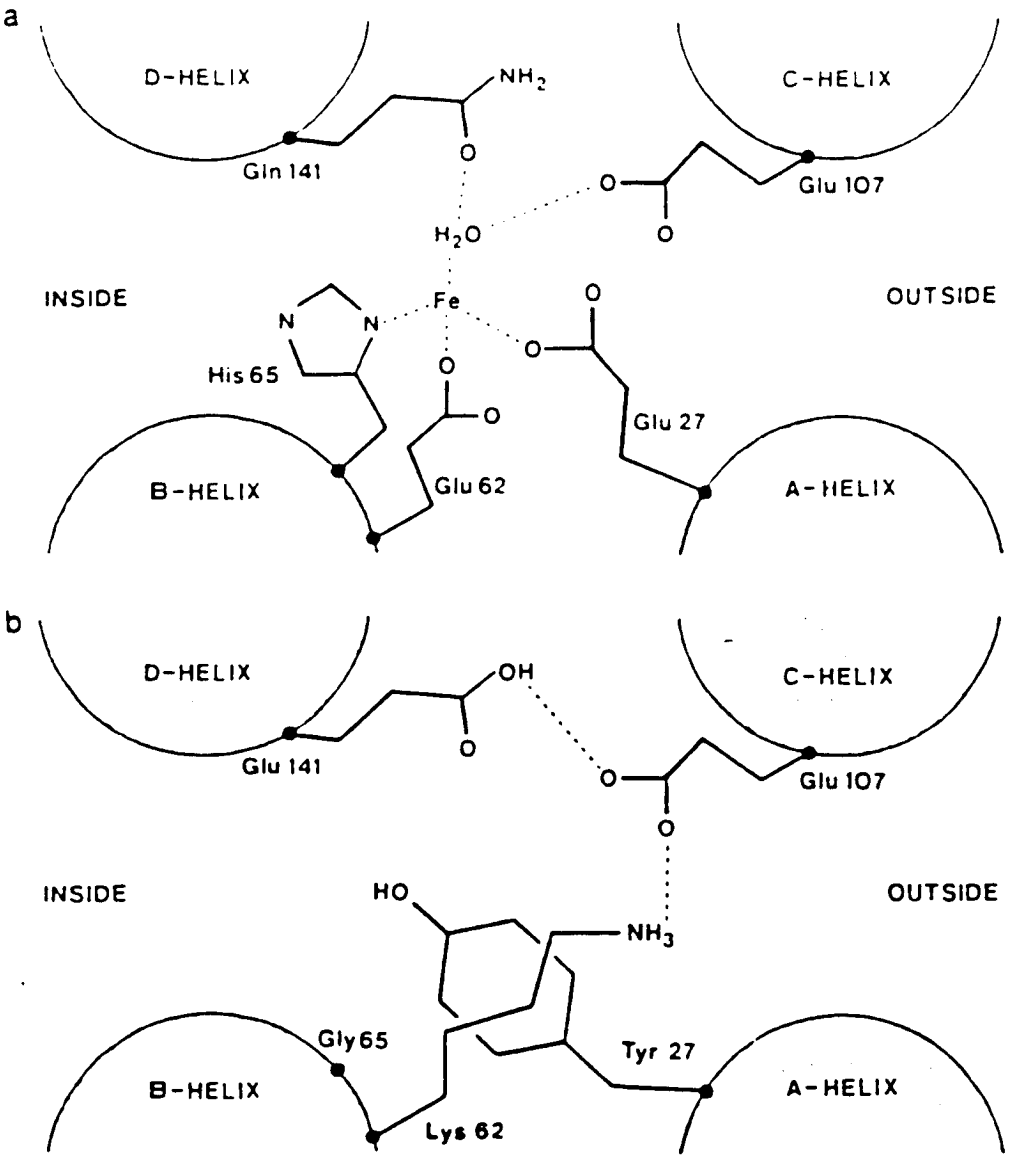

Figure 5. Schematic illustration of the ferroxidase site of human rHF (a), and the similar region of horse spleen light-chain ferritin (b) (Harrison et al., 1991).

(Chasteen et al., 1985; Hanna et al., 1991); (2) the initial UV-absorption species formed from single Fe^{3+} bound by ferritin shell (Treffry & Harrison, 1984); (3) EXAFS spectra of small Fe^{3+} clusters connected to protein carboxyl side chains (Yang et al., 1987); (4) Various Fe^{3+}-protein species detected by Mossbauer spectroscopy, such as isolated Fe^{3+}, Fe^{3+}-Fe^{3+} dimers, small and large Fe^{3+} clusters (Bauminger et al., 1989; St. Pierre et al., 1986); (5) Fe^{3+}-tyrosinate complex during biomineralization of bullfrog H-subunit ferritin examined by UV and resonance Raman spectroscopies (Waldo et al., 1993). Although the locations of the Fe^{3+} binding sites and the nature of the ligands of these spectroscopically active Fe^{3+}-protein species are not clear, they are possible intermediate species which may facilitate the final Fe^{3+} nucleation at the putative nucleation sites inside the protein cavity.

The Molecular Mechanism of Iron Uptake

Two possible entries by which Fe^{2+} may travel to the protein ferroxidase center have been proposed (Harrison et al, 1991). One is the three-fold channels which are known to bind metal ions, the other is the one-fold channel in the H-subunit of rHF which is closer to the ferroxidase site (12 Å) than the three-fold channel (50 Å) (Harrison et al, 1991). However, the precise pathways by which Fe^{2+} travels to the ferroxidase center remains undefined.

X-ray crystallography of Tb(III)-rHF showed three

Tb(III) binding sites, site A (Glu-27, Glu-62, His-65), site B (Glu-61, Glu-62, Glu-107) and site C (Glu-61, Glu-64) (Fig. 4B). Site A and site C are the putative ferroxidase and nucleation sites respectively. Site A and site B are very close to each other and share a common ligand, Glu-62, while Glu-61 is common to both site B and Site C which is located on the inner surface of the protein shell. The Fe^{3+} formed at the ferroxidase site is postulated to move from site A to the nucleation site C via site B (Harrison et al, 1991). However, this hypothesis still needs to be confirmed by further iron binding studies.

Kinetics of Ferritin Reconstitution

Two kinetic models for the Fe^{2+} oxidation and Fe^{3+} deposition in ferritin have been proposed. In the crystal growth model (Macara et al., 1972; Harrison et al., 1974), apoferritin facilitates only the early stage of iron oxidation and deposition, and once an iron core is formed inside the protein cavity, late arriving Fe^{2+} is oxidized and deposited directly on the surface of the iron core. However, the protein-catalysis model proposed by Crichton postulates that the protein shell functions as a ferroxidase during the entire process of iron uptake in ferritin (Bryce & Crichton, 1973). Both of the proposed models are based on the observations of color development during iron oxidation, as monitored spectroscopically. But color changes may not accurately represent the iron oxidation reaction (Rohrer et

al., 1987).

To date, the ferroxidase activity of apoferritin has been well established, especially during the early stage of iron oxidation. Nevertheless, detailed kinetic and mechanistic studies of iron oxidation in apoferritin have not been performed due to the lack of an accurate assay of the reaction. This thesis focuses on the kinetics and mechanism of iron oxidation in apoferritins, including the well characterized horse spleen apoferritin (Chapter I), human liver apoferritin, recombinant H and L chain human ferritin, and site-directed mutants as well as sheep spleen apoferritin (Chapter II). An oxygen micro-electrode has been used to directly monitor the iron oxidation reaction. Detailed reaction mechanisms have been elaborated based on the experimental results. In addition, some intermediate species produced during the iron oxidation and deposition in apoferritin have been investigated using the fast-mixing freeze quench technique as well as EPR spectroscopy (Chapter III).

CHAPTER I

FERROXIDASE KINETICS OF HORSE SPLEEN APOFERRITIN

INTRODUCTION

As an iron storage protein, the ferritin shell plays an integral part in iron core formation. Iron(II) complexation by the protein followed by oxidation to Fe^{3+} at protein "ferroxidase" sites appears to be key steps in the oxidative deposition of iron in ferritin (Bakker & Boyer, 1986; Harrison et al., 1986; Levi et al., 1989; Lawson et al., 1989, 1991). Subsequent formation of the polynuclear iron core occurs at nucleation sites which may be the same as or distinct from these ferroxidase sites (Harrison et al., 1986). Although the ferroxidase activity of ferritin appears to be central to its function, detailed studies of the kinetics of iron oxidation in ferritin have been precluded previously by a lack of knowledge of the stoichiometric equations for iron(II) oxidation and the need for an accurate assay of the reaction. Color development during core formation traditionally has been used to follow the progress of the iron oxidation reaction but it is now known that color changes can occur even in the absence of iron oxidation (Rohrer et al., 1987).

The stoichiometric equations for iron oxidation in

ferritin have been recently determined by ^{16}O mass spectrometry in conjunction with ^{57}Fe Mössbauer spectroscopy (Xu & Chasteen, 1991). For apoprotein molecules to which small increments of iron(II) (24 Fe/protein) are added, two Fe^{2+} are oxidized per O_2 consumed with H_2O_2 being the product of dioxygen reduction, *viz*,

$$2Fe^{2+} + O_2 + 4H_2O \longrightarrow 2FeOOH_{core} + H_2O_2 + 4H^+. \qquad (1.1)$$

The above reaction presumably occurs at protein ferroxidase sites (Xu & Chasteen, 1991). However, when larger increments of iron are added (240 - 960 Fe/protein), the stoichiometry of iron(II) oxidation increases to four Fe^{2+} oxidized per O_2 reduced according to equation 1.2,

$$4Fe^{2+} + O_2 + 6H_2O \longrightarrow 4FeOOH_{core} + 8H^+ \qquad (1.2)$$

where in this instance oxidation evidently occurs on the surface of the growing mineral core.

With knowledge of the stoichiometric equations in hand, it is now possible to carry out detailed kinetic studies of the oxidative deposition of iron in ferritin with the goal of elucidating some of the salient features of the reaction mechanism. In the present work, the kinetics of iron oxidation was followed *directly* by electrode oximetry, enabling the rate law for the reaction to be determined. The results demonstrate that horse spleen ferritin behaves

as an enzyme, exhibiting saturation kinetics with respect to the substrates Fe^{2+} and O_2. The protein has a pH optimum for ferroxidase activity near 7.0. Significantly, the data show that protein ferroxidase sites are involved in iron oxidation at all stages of iron accumulation by the protein (up to 1200 Fe/protein) provided that iron is introduced to the protein in small increments ($\leq$ 50 Fe^{2+}/protein), a finding in accord with the protein catalysis model of iron deposition in ferritin (Crichton & Roman, 1978). However, at higher increments (~ 160 Fe^{2+}/protein) some iron(II) oxidation occurs by an alternate pathway which appears to involve oxidation on the surface of the mineral core as predicted by the crystal growth model for core formation (Marcara et al., 1972, 1973).

MATERIALS AND METHODS

Horse spleen ferritin, 3 X crystallized/cadmium free, was obtained from Boehringer Mannheim GmbH. The apoferritin was prepared by dialysis against thioglycolic acid as previously described (Hanna et al., 1991). The concentration of apoferritin on a subunit basis was measured on a Cary 219 spectrophotometer using a molar absorptivity $\epsilon_{280\,nm}$= 1.95 x 10^4 $M^{-1}cm^{-1}$ per subunit (Heusterspreute & Crichton, 1981). All protein concentrations stated throughout refer to the concentration of the 24mer. Iron was added to apoferritin as a freshly prepared 0.100 M ferrous sulfate heptahydrate (J.T. Baker Co.) in 0.05 M HCl. Potassium superoxide solutions of nominally 0.1 M concentration were prepared by dissolving of solid KO_2 (Aldrich Chemical Co., Inc.) in 0.1 M dicyclohexyl-18-crown-6 ether (Aldrich) in dimethyl-sulfoxide (Oldfield & Allerhand, 1975) and used immediately. Bovine liver catalase (EC 1.11.1.6) and bovine erythrocyte superoxide dismutase[1.1] (EC 1.15.1.1) were purchased from Boehringer Mannheim and employed as previously described (Xu & Chasteen, 1991). The amounts of H- and L-subunits in horse spleen ferritin were determined to be 16% H and 84% L from the integrated peak areas of densitometer scanned Coomassie blue R250 stained bands of 17.5% SDS polyacrylamide gels (Adelman et al., 1975; Arosio et al., 1978).

Reconstituted ferritin samples containing up to 1200

Fe/protein were prepared by gradually adding microliter quantities of 0.100 M $FeSO_4 \cdot 7H_2O$, with stirring, to 4.2 μM apoferritin in 0.1 M NaCl, 75 mM Mops buffer, pH 7.05 followed by stirring in air for ~ 1 hr. The samples then stood overnight at 4 ^{o}C before being used.

Kinetic measurements of iron oxidation were performed with an MI-730 rapid response oxygen microelectrode (6 s for 90% response) and a OM-4 oxygen meter, both purchased from Microelectrodes Inc. of Londonderry, New Hampshire. The meter output was recorded on a strip chart recorder. Figure 1.1 shows the experimental setup. The 0.45 mL sample cell was made from acrylic and consisted of two halves which screwed together to eliminate any gas head space. The two halves were sealed together with an "O" ring. The top of the cell had a port machined to close tolerance to accommodate the snugly-fitted oxygen electrode. The side of the cell had a small port to just accommodate a syringe needle through which iron(II) and other reagents or samples could be added or removed. The diffusion of molecular oxygen in or out of the cell over a period of 30 minutes was insignificant. Prior to each experiment, the oxygen meter was calibrated with air-saturated buffer and a freshly-made anaerobic solution of 1 M $Na_2S_2O_4$ (Aldrich) at 20^{o}C. Initial rates of oxygen consumption were based on the decrease in dissolved O_2 concentration in the first 12 seconds of the reaction. In a typical experiment, around 15 % of Fe^{2+} has been oxidized at this time. The reaction was initiated by

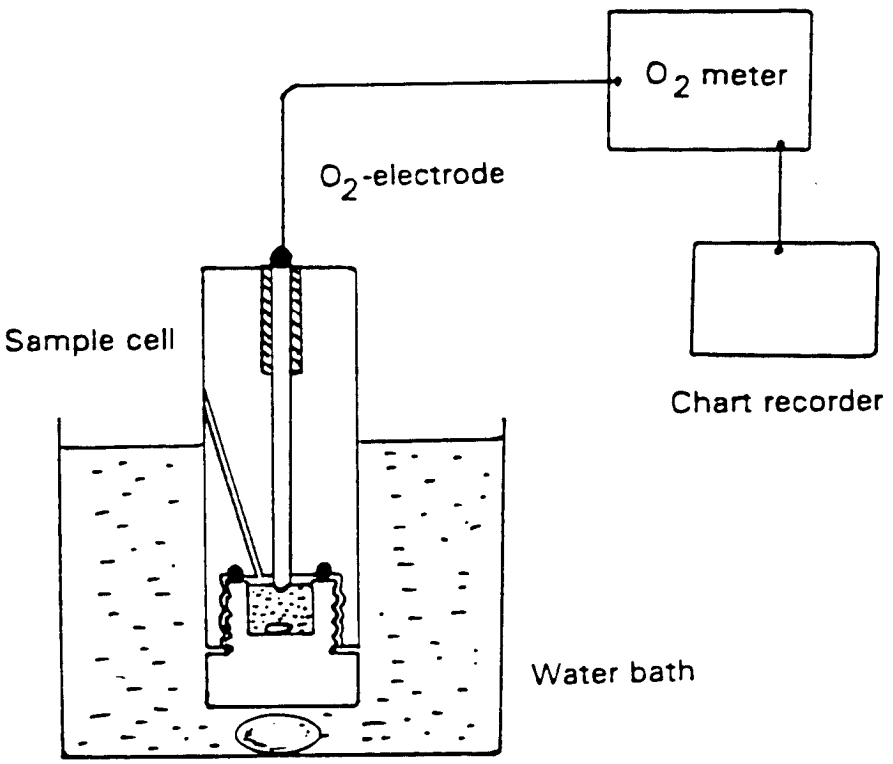

Figure 1.1. Experimental setup for the kinetic measurement.

the microliter syringe addition of ferrous sulfate solution to the cell.

To test the system, the reaction of Fe^{2+} oxidation in the presence of nitrilotriacetate (NTA) was employed. The rate of oxidation of Fe^{2+} in 2.0 mM NTA, 50 mM Mes, pH 6.28 was measured at 20 °C. The first order plots with respect to Fe^{2+} concentration (Fig. 1.2) and O_2 concentration (Fig. 1.3) were obtained with an apparent rate constant of 4.6 $\pm$ 0.1 $mM^{-1}min^{-1}$ (77 $M^{-1}s^{-1}$), a result in accord with the published rate law and rate constant (Kurimura *et al*, 1968).

In the zinc inhibition studies, 0.100 M reagent grade $ZnSO_4 \cdot 7H_2O$ (Mallinckrodt Chemical Works)) was added to 4.2 μM apoprotein and incubated for 1 hr at ~20 °C prior to addition of the iron(II) as 0.100 M ferrous sulfate.

Rate, Michaelis and inhibition constants for apoferritin were derived from nonlinear and linear least-squares fits of the various kinetic data using the software program MINSQ (Micromath Scientific Software) which employs a modification of the Levenberg-Marquardt technique.

In the Cr^{3+} inhibition experiments, a stock solution of $\approx$ 0.2 M Cr^{2+} was first prepared by dissolving 0.12 g of metal chromium in 10 ml of 2 M HCl under strictly anaerobic condition, then 2.0 - 5.0 μl of the stock Cr^{2+} solution were introduced to 2.0 ml of 8.3 μM deoxygenated apoferritin solution in 0.2 M mops buffer, pH 7.2. After incubating the mixture for about 5 minutes, the mixture was exposed to air and the rate of iron oxidation was determined using the

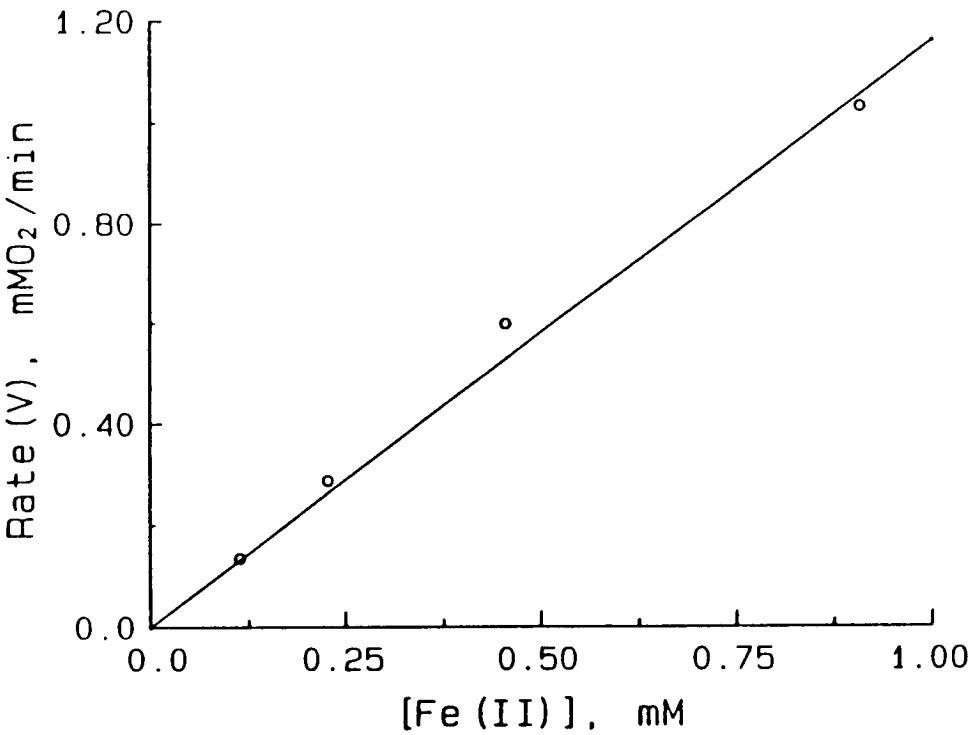

Figure 1.2. First order plot with respect to Fe^{2+} concentration for the oxidation of Fe^{2+}-NTA. Conditions: [NTA] = 2.0 mM, [Mes] = 50 mM, $[O_2]_0$ = 0.26 mM, pH = 6.28, 20 ^{0}C. File name: "91my29a"

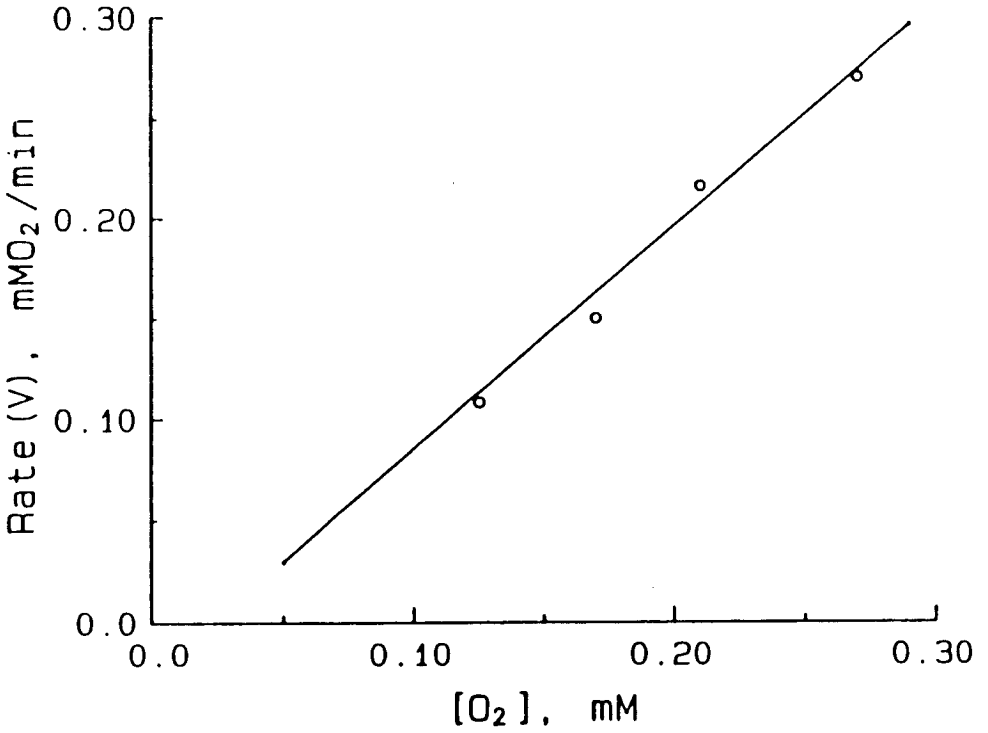

Figure 1.3. First order plot with respect to O_2 concentration for the oxidation of Fe^{2+}-NTA. Conditions: [NTA] = 2.0 mM, [Mes] = 50 mM, $[Fe^{2+}]_0$ = 0.23 mM, pH = 6.28, 20 ^{0}C. File name: "91my29b"

oxygen electrode. At the end of iron oxidation, the Fe^{3+}-protein-Cr^{3+} solution was transferred from the oxygen electrode cell to an EPR tube, and the EPR spectrum at g' 4.3 was measured on E-4 EPR spectrometer.

Stoichiometry studies were performed by adding a certain amount of freshly prepared 0.100 M $FeSO_4.7H_2O$ to a series of oxygenated 0.44-8.4 μM protein solutions. The Fe/protein ratios range from 10/1 to 960/1.

RESULTS

The Rate Law.

Figure 1.4 shows typical dissolved oxygen uptake curves when ferrous sulfate is added to buffer (curve A) or to apoferritin in buffer (curve B). It is evident that the presence of apoferritin greatly accelerates the rate of iron(II) oxidation and oxygen consumption. The oxygen concentration decreases rapidly in the presence of the protein, reaching a plateau when all of the iron(II) has been oxidized. From the oxygen consumed in the reaction, the stoichiometry of iron oxidation can be calculated.[1.1] A value of 2 Fe^{2+} oxidized per molecule of oxygen consumed was generally obtained from the oxygen uptake experiments in accord with the reported stoichiometry given by equation 1.1 (Xu & Chasteen, 1991).

The initial rate of oxygen consumption plotted as a function of Fe^{2+} concentration is shown in Figure 1.5. Saturation kinetics is observed, suggesting a mechanism in which the Fe^{2+} complexes with the protein prior to oxidation. The inset of Figure 1.5 shows the corresponding Lineweaver-Burk plot which is linear as expected for saturation kinetics. The dependence of the initial rate on the apoferritin concentration was also investigated and it was found to be simple first order in protein concentration (Fig. 1.6).

Figure 1.7 illustrates the effect of dissolved dioxygen

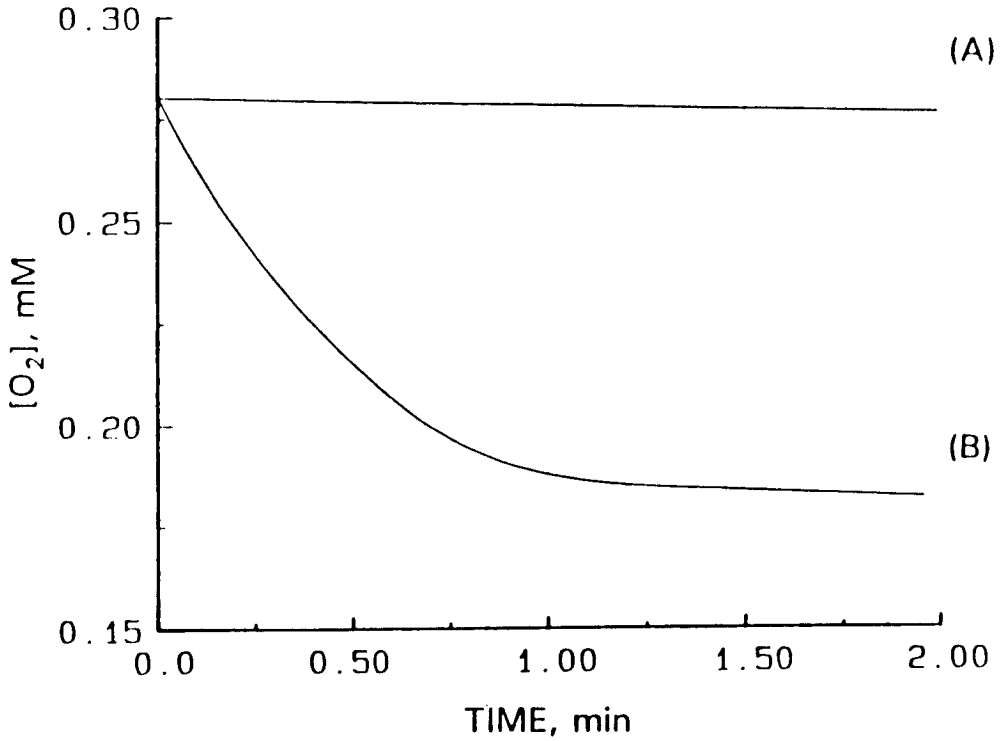

Figure 1.4. Oxygen consumption versus time for the oxidation of Fe(II) in the absence (A) and in the presence (B) of apoferritin. Conditions: [apoferritin] = 8.3 μM, $[Fe^{2+}]_o$ = 0.22 mM, in 0.10 M NaCl, 50 mM Mops, pH 7.05, 20 °C. File name: "Jan161 (A) and Jan162 (B)"

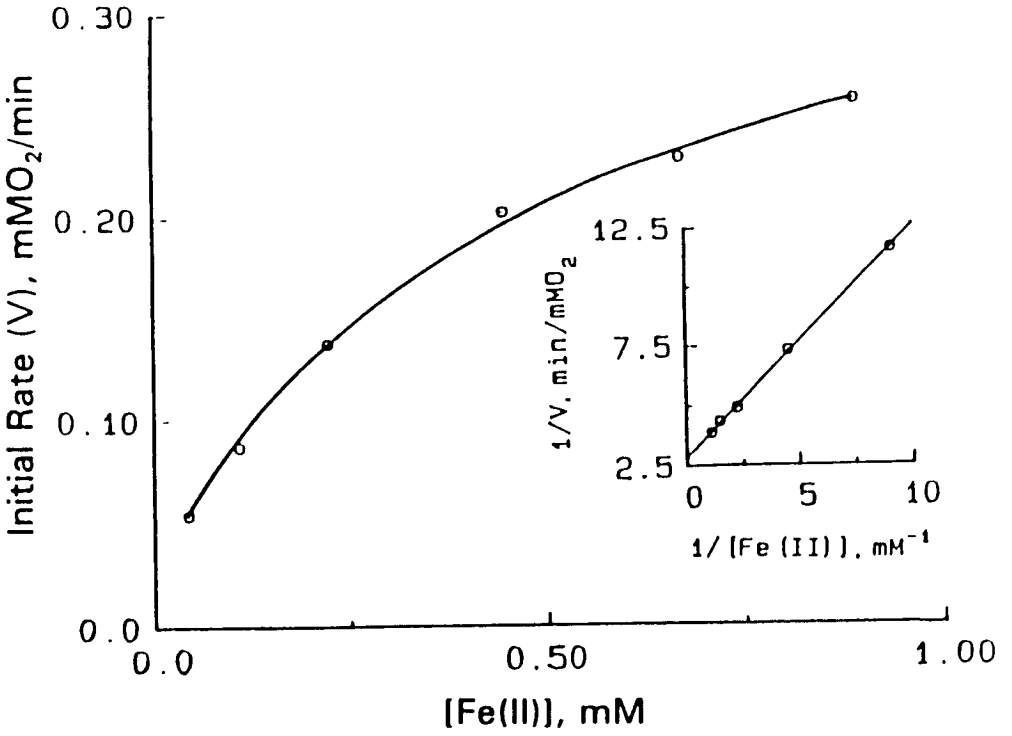

Figure 1.5. Rate of O_2 consumption as a function of iron(II) concentration. Inset: Lineweaver-Burk plot with the least-squares straight line shown. The outlier data point at low iron(II) concentration was omitted from the fit. Conditions: [apoferritin] = 8.3 μM, $[O_2]_o$ = 0.28 mM, in 0.1 M NaCl, 50 mM Mops, pH 7.05, 20 °C. File name: Sep012 and Sep013 (inset)"

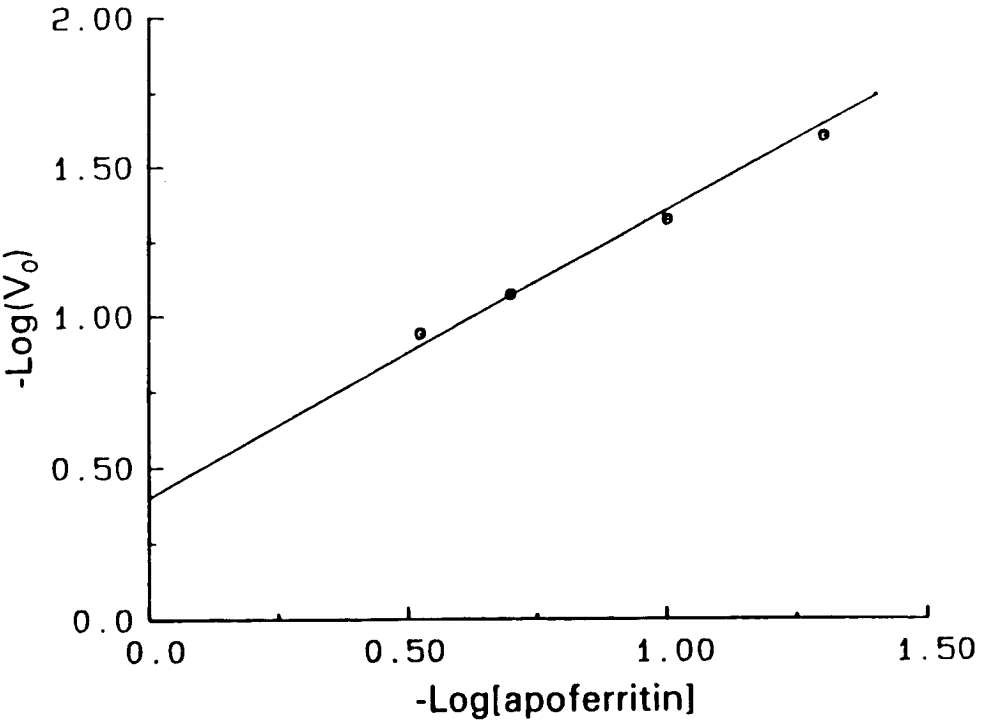

Figure 1.6. First order plot with respect to apoferritin for iron oxidation in horse spleen ferritin. Conditions: $[Fe^{2+}]_0$ = 0.22 mM, $[O_2]_0$ = 0.28 mM, in 0.1 M NaCl, 50 mM Mops, pH 7.05, 20 ^{0}C. File name: "Sep071"

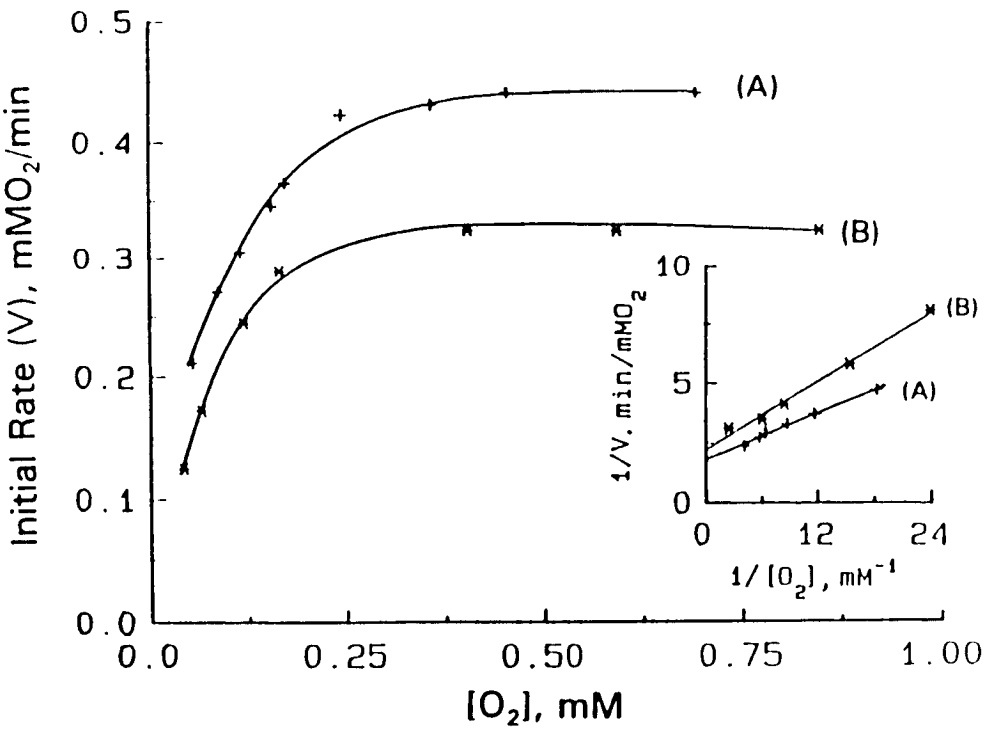

Figure 1.7. Rate of O_2 consumption as a function of O_2 concentration at two different iron(II) concentrations, (A) 0.67 mM Fe^{2+} and (B) 0.44 mM Fe^{2+}. Inset: Lineweaver-Burk plots with the least-squares straight lines shown. The points on the plateau are not included in these plots. Conditions: iron(II)/apoferritin ratio = 43, in 0.1 M NaCl, 50 mM Mops, pH 7.05, 20 °C. File name: "Jul113 (A), Jul111 (B), Aug123 (inset, A), and Aug121 (inset, B)"

concentration on the initial rate of oxygen uptake at two different Fe^{2+} concentrations. Saturation kinetics with respect to oxygen concentration is observed in both instances. The corresponding linear Lineweaver-Burk plots are shown in the inset.

Saturation kinetics with respect to both [Fe^{2+}] and [O_2] concentrations and first-order kinetics with respect to protein concentration can be explained by the following enzyme catalyzed mechanism (Mechanism I) or by Mechanism II described later in this section for iron oxidation in apoferritin. First we consider Mechanism I and the supporting experimental evidence.

MECHANISM I

$$\text{Iron(II) binding:} \quad P + Fe^{2+} \underset{k_{-1}}{\overset{k_1}{\rightleftarrows}} Fe^{2+}\text{-}P \qquad (1.3)$$

$$\text{Dioxygen binding:} \quad Fe^{2+}\text{-}P + O_2 \underset{k_{-2}}{\overset{k_2}{\rightleftarrows}} Fe^{2+}(O_2)\text{-}P \qquad (1.4)$$

$$\text{Iron(II) oxidation:} \quad Fe^{2+}(O_2)\text{-}P \xrightarrow{k_3} Fe^{3+}\text{-}P + O_2^- \qquad (1.5)$$

$$\text{Iron(III) formation:} \quad Fe^{3+}\text{-}P + 2H_2O \xrightarrow{k_4} FeOOH_{core} + P + 3H^+ \qquad (1.6)$$

$$\text{Fate of superoxide:} \quad 2O_2^- + 2H^+ \xrightarrow{k_5} H_2O_2 + O_2 \qquad (1.7)$$

or

$$2H^+ + O_2^- + Fe^{2+}\text{-}P \xrightarrow{k_{5'}} Fe^{3+}\text{-}P + H_2O_2 \qquad (1.7')$$

Reactions 1.3 and 1.4 correspond to Fe^{2+} and O_2 binding at the active site designated here by P. Once the ternary $Fe^{2+}(O_2)$-P complex is formed, the Fe^{2+} is rapidly oxidized in a one-electron transfer (reaction 1.5) to produce superoxide, O_2^-, and Fe^{3+}-P. The Fe^{3+} formed in reaction 1.5 is rapidly hydrolyzed and migrates to core in reaction 1.6, freeing up the ferroxidase site P to bind Fe^{2+} once again in reaction 1.3.

Reactions 1.7 and 1.7′ account for the fact that H_2O_2 is a product of iron(II) oxidation and give the required stoichiometry of 2 Fe^{2+} oxidized per O_2 consumed in the overall reaction (equation 1.1) (Xu & Chasteen, 1991). In reaction 1.7, superoxide disproportionates via the dismutase reaction to produce H_2O_2 and O_2, whereas in reaction 1.7′ a second Fe^{2+} is oxidized by superoxide at the active site to produce Fe^{3+}-P and H_2O_2. Inclusion of either reaction 1.7 or 1.7′ in the mechanism leads to the rate equations 1.8 or 1.8′ in double reciprocal form (Appendix I).

$$1/V = (2/[P]_o)\{1/k_1[Fe^{2+}] + (k_{-2}+k_3)/k_2k_3[O_2] + 1/k_3\} \qquad (1.8)$$

or

$$1/V = (1/[P]_o)\{2(k_{-2}+k_3)/k_1k_3[Fe^{2+}] + 2(k_{-2}+k_3)/k_2k_3[O_2] + 1/k_3\} \qquad (1.8')$$

Both equations 1.8 and 1.8′ predict saturation kinetics with respect to $[Fe^{2+}]$ and $[O_2]$ as is observed experimentally (Figs. 1.5 and 1.7). To determine whether

reaction 1.7 or 1.7′ is the dominant reaction for H_2O_2 production, iron(II) oxidation experiments were carried out using superoxide directly. Curve A in Figure 1.8 shows the production of O_2 by the dismutase reaction when KO_2 was added aerobically to the apoprotein in buffer in the absence of iron(II) (Materials and Methods). The same curve was obtained with buffer alone or with the holoferritin in buffer (data not shown).

In contrast, curve B of Figure 1.8 shows the O_2 concentration profile obtained when KO_2 was added anaerobically to Fe^{2+}-apoferritin. It can be seen that the O_2^- rapidly undergoes the dismutation reaction 1.7; the O_2 so produced is then consumed by reaction with the Fe^{2+}.[1,3] From these results it is clear that O_2 is the primary oxidant of the Fe^{2+}. (If O_2^- had preferentially reacted with the Fe^{2+}-P complex, no O_2 would have been produced, opposite from what is observed.) Reaction 1.7′, if it occurs at all, must do so to a minor extent. Accordingly, equation 1.8 as well as its reciprocal form, equation 1.9, were used to analyze the iron and oxygen saturation curves. In these equations $[P]_o$ was taken either as the

$$V = \frac{\frac{1}{2}k_1k_2[P]_o[Fe^{2+}][O_2]}{k_2[O_2] + k_1(k_3+k_{-2})/k_3[Fe^{2+}] + k_1k_2/k_3[Fe^{2+}][O_2]} \qquad (1.9)$$

concentration of the apoferritin 24mer or as the concentration of the ferroxidase sites in the protein. The number of the ferroxidase sites was obtained based on the H

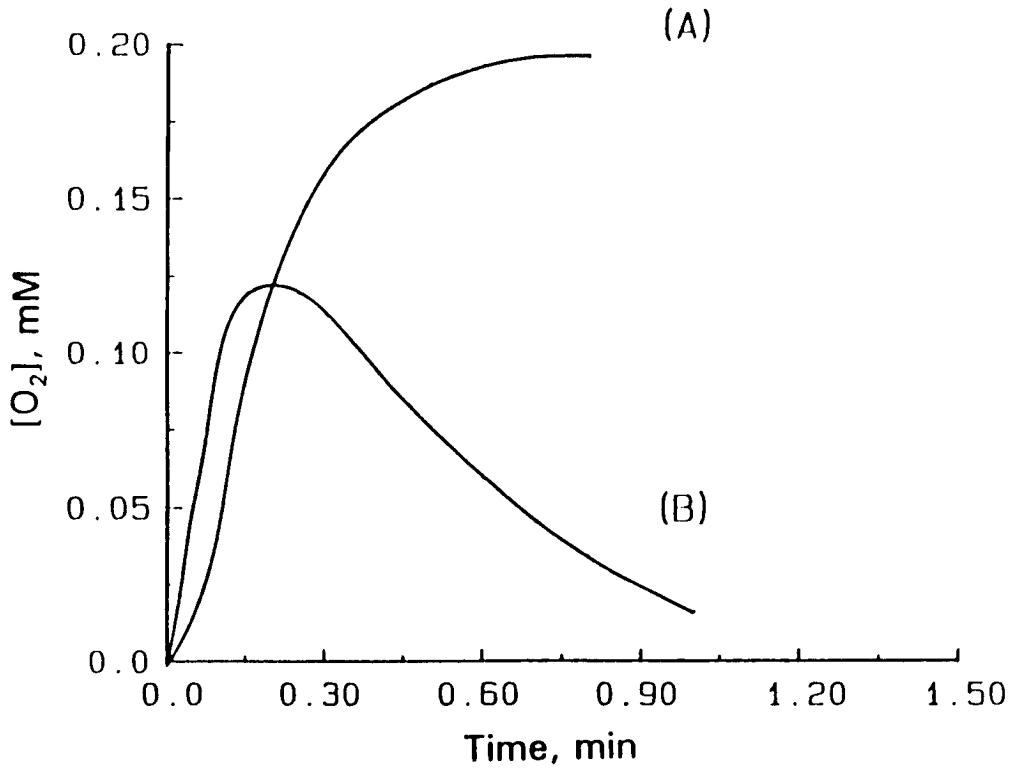

Figure 1.8. Oxygen production during dismutation of superoxide in buffer containing either (A) apoferritin or (B) Fe^{2+}-apoferritin. KO_2 as a 0.1M solution of dicyclohexyl-18-crown-6 in DMSO was added anaerobically to either solution A or B and the O_2 concentration monitored as a function of time. Conditions: [apoferritin] = 4.2 μM, $[Fe^{2+}]_o$ = 0 (A) or 1.232 mM (B), $[KO_2]_o$ = 0.406 mM, in 0.1 M NaCl, 50 mM Mops, pH 7.05, 20 °C. File name: "Feb254 (A) and Feb255 (B)"

subunit composition of horse spleen ferritin. An implicit assumption in this analysis is that the sites function independently. The average values of the kinetic parameters obtained from least-squares curve fitting of various data sets are summarized in Table I.I.

Recently ultraviolet difference spectra have provided evidence for the formation of a μ-oxo-bridged Fe^{3+} dimer at the ferroxidase site during Fe^{2+} oxidation in ferritin H-chains (Bauminger et al., 1991; Treffry et al., 1992). In the proposed mechanism, two Fe^{2+} ions simultaneously bind in the H-subunit ferroxidase site in close proximity to one another, followed by dioxygen binding (Treffry et al., 1992). A concerted 2-electron transfer to dioxygen then occurs with hydrogen peroxide as the product (Treffry et al., 1992). Since the first step in the proposed mechanism involves binding of two Fe^{2+} to the ferroxidase site, a second-order dependence of the rate on initial Fe^{2+} concentration is expected; no such dependence is observed in the present work, ruling out that aspect of the proposed mechanism. (Below kinetic saturation, the reaction is in fact first-order in iron.) All mechanisms we have considered which involve a 2-electron transfer from oxygen to a diiron center predict that second-order kinetics in iron should be observed.

The presence of a putative μ-oxo-bridged Fe^{3+} dimer can be reconciled with the present kinetic data in one of two ways. In the first, the dimer could simply be a core

TABLE 1.1

Kinetic Parameters for Apoferritin Ferroxidase Activity[a]

k_1	178 ± 30 mM-min^{-1} (2970 M^{-1}s^{-1})
k_{cat}	80 ± 3 min^{-1} (1.3 s^{-1})[b1]
k_{cat}	21.2 ± 0.8 min^{-1} (0.34 s^{-1})[b2]
$K_{m,O2}$	0.14 ± 0.03 mM[c]
$K_{m,Fe}$	0.35 ± 0.01 mM[d]
$K_{I,Zn}$	0.067 ± 0.011 mM[c]
$(k_3+k_{-2})/k_1k_2$	0.00179 ± 0.0003 mM-min (1.07 x 10^{-4} M-s)
E_a	36.6 ± 1.3 kJ/mol[f]
$\Delta H^{\ddagger}$	34.2 ± 1.3 kJ/mol[f]
$\Delta S^{\ddagger}$	-108 ± 5 J/mol-K[f]

[a]Conditions: 0.10 M NaCl, 50 mM Mops, pH 7.05, 20°C. Except where noted, averages and standard errors were calculated from 4 independent data sets. The protein used for all the studies consisted of 16% H and 84% L subunits.

[b1]$k_{cat} = k_3$, based on the 24mer protein concentration.

[b2]k_{cat} per ferroxidase site.

[c]Apparent Michaelis constant for O_2 at saturating Fe^{2+} concentration, $K_{m,O2} = (k_3+k_{-2})/k_2$.

[d]Apparent Michaelis constant for Fe(II) at saturating O_2 concentration, $K_{m,Fe} = k_3/k_1$. Normally $K_{m,Fe}$ would be given by $K_{m,Fe} = (k_3+k_{-1})/k_1$ but in deriving equation 8, k_{-1} was assumed small relative to $k_2[O_2]$.

[e]Competitive inhibition constant for Zn^{2+} binding. Average from 4 independent data sets, two in which $[Zn^{2+}]_o$ was held fixed and $[Fe^{2+}]_o$ varied and vice versa.

[f]From the temperature dependence in k_1. Single data set (Fig. 1.9).

nucleation species, formed as an intermediate in reaction 1.6 of Mechanism I. In this case, it would not be expected to influence the observed oxidation kinetics since it would be formed after the rate determining step (reaction 1.5).

In the second case, formation of a μ-oxo bridged dimer, $Fe^{3+}(O_2^{=})Fe^{3+}$-P, at the ferroxidase site can be accounted for by modifying the latter steps of Mechanism I to give Mechanism II, *viz.*

MECHANISM II

$$\text{1st } Fe^{2+} \text{ binding: } \quad P + Fe^{2+} \underset{k_{-1}}{\overset{k_1}{\rightleftarrows}} Fe^{2+}\text{-P} \qquad (1.10)$$

$$\text{Dioxygen binding: } \quad Fe^{2+}\text{-P} + O_2 \underset{k_{-2}}{\overset{k_2}{\rightleftarrows}} Fe^{2+}(O_2)\text{-P} \qquad (1.11)$$

$$\text{1st } Fe^{2+} \text{ oxidation: } \quad Fe^{2+}(O_2)\text{-P} \xrightarrow{k_3} Fe^{3+}(O_2^{-})\text{-P} \qquad (1.12)$$

$$\text{2nd } Fe^{2+} \text{ binding/oxidation: } \quad Fe^{3+}(O_2^{-})\text{-P} + Fe^{2+} \xrightarrow{k_4} Fe^{3+}(O_2^{=})Fe^{3+}\text{-P}$$

$$\xrightarrow{k_5\ H_2O} Fe^{3+}(O^{2-})Fe^{3+}\text{-P} + H_2O_2 \qquad (1.13)$$

The principal difference between Mechanism I and Mechanism II is that in the latter mechanism, the superoxide is not released from the active site bound to Fe^{3+}. The second Fe^{2+} then binds (reaction 1.13) and is oxidized to form either a peroxo bridge or a terminally bound peroxo group, ultimately leading to formation of the spectroscopically

observed μ-oxo bridged Fe^{3+} dimer, $Fe^{3+}(O^{2-})Fe^{3+}$-P, and H_2O_2 (reaction 1.13). The derived rate law for Mechanism II is given by equation 1.14 (Appendix I).

$$1/V = (2/[P]_o)\{(k_1+k_4)/k_1k_4[Fe^{2+}] + (k_3+k_{-2})/k_2k_3[O_2] + (k_3+k_5)/k_3k_5\} \quad (1.14)$$

Saturation kinetics with respect to both $[Fe^{2+}]$ and $[O_2]$ is also predicted in this case but the expressions for k_{cat}, $K_{m,Fe}$, and $K_{m,O2}$ in terms of the fundamental rate constants are more complicated, namely $k_{cat} = k_3k_5/(k_3+k_5)$, $K_{m,Fe} = (k_1+k_4)(k_3+k_5)/k_1k_3k_4k_5$ and $k_{m,O2} = (k_{-2}+k_3)(k_3+k_5)/k_2k_3^2k_5$. The corresponding quantities for Mechanism I are given in the footnotes of Table 1.1.

Temperature Dependence

The temperature dependence of k_1 of iron(II) binding to apoferritin is illustrated in Figure 1.9. k_1 was obtained under conditions where the initial rate was first-order in $[Fe^{2+}]_o$ and zero-order in $[O_2]$, *i.e.* saturating O_2 conditions. An apparent activation energy E_a = 36.6 ± 1.4 kJ/mol (8.8 ± 0.4 kcal/mol), enthalpy of activation $\Delta H^{\ddagger}$ = 34.2 ± 1.4 kJ/mol (8.3 ± 0.3 kcal/mol) and entropy of activation $\Delta S^{\ddagger}$ = -108 ± 5 J/mol-K (-26.1 ± 1.1 cal/mol-K) were obtained from the Arrhenius plot.

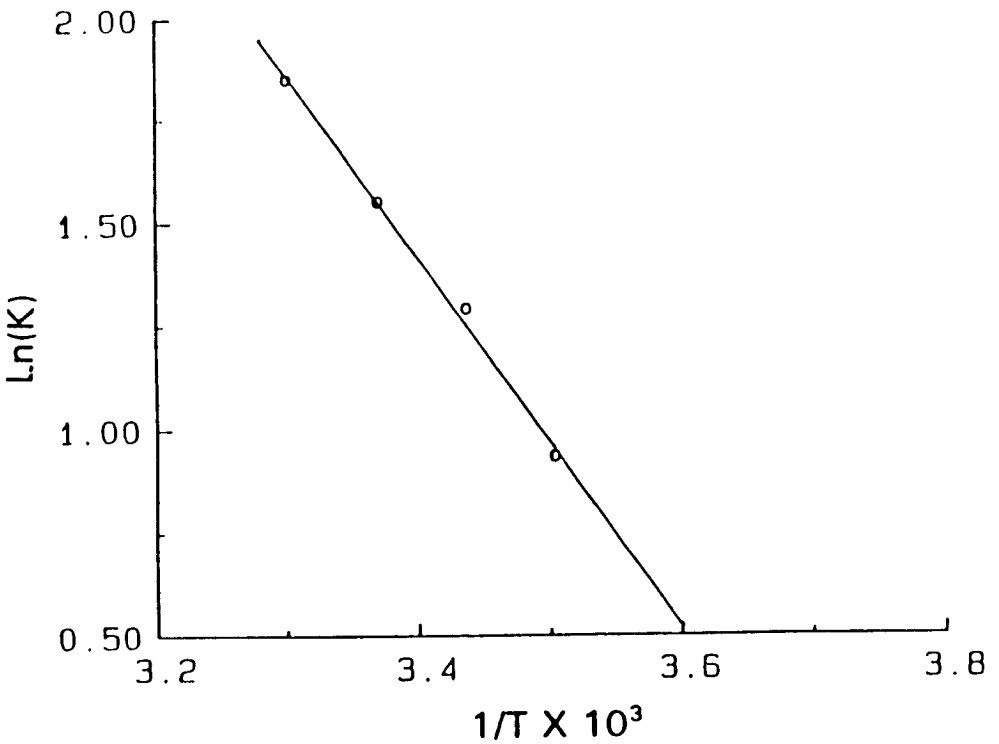

Figure 1.9. Arrhenius plot for k_1 with the least-squares line shown. Inset: pH dependence of initial rate. Conditions: [apoferritin] = 8.3 μM, $[Fe^{2+}]_o$ = 0.11 mM, $[O_2]_o$ = 0.27 mM, in 50 mM Mops, pH 7.04, 20 °C. File name: "Aug124"

pH Dependence

The initial rates of oxygen consumption were plotted against pH under two different Fe^{2+}/protein ratios (Fig. 1.10). The pH dependence shows a broad maximum centered around pH 7 at low Fe^{2+}/protein ratio (Fig. 1.10A), while the initial rate of iron oxidation increases with increasing pH at higher Fe^{2+}/protein ratios (Fig. 1.10B). Fig. 1.11 illustrates the pH dependence of the initial rate in the presence of a iron core inside the protein (340 Fe^{3+}/protein). The Fe^{2+}/protein ratio in this experiment is around 24.

Inhibition by Zinc(II)

Zinc(II) is known to be an inhibitor of iron deposition in ferritin, especially in the early stages of core formation (Treffry et al, 1977). Experiments therefore were undertaken to determine whether the effect of Zn^{2+} was due to inhibition of iron(II) oxidation or possibly due to Zn^{2+} binding at core nucleation sites and blocking core formation. The reciprocal of the initial rate of oxygen consumption, 1/V, as a function of $1/[Fe^{2+}]_o$ at various fixed $[Zn^{2+}]_o$ concentration is plotted in Figures 1.12 and 1.13. The data shows Zn^{2+} to be a non-competitive inhibitor of iron(II) oxidation when present in small amounts (Zn^{2+}/apoprotein $\leq$ 2, Fig. 1.12). Within standard error, the lines intersect the abscissa at a common point. At higher amounts of zinc (Zn^{2+}/apoprotein $\geq$ 6), the inhibition

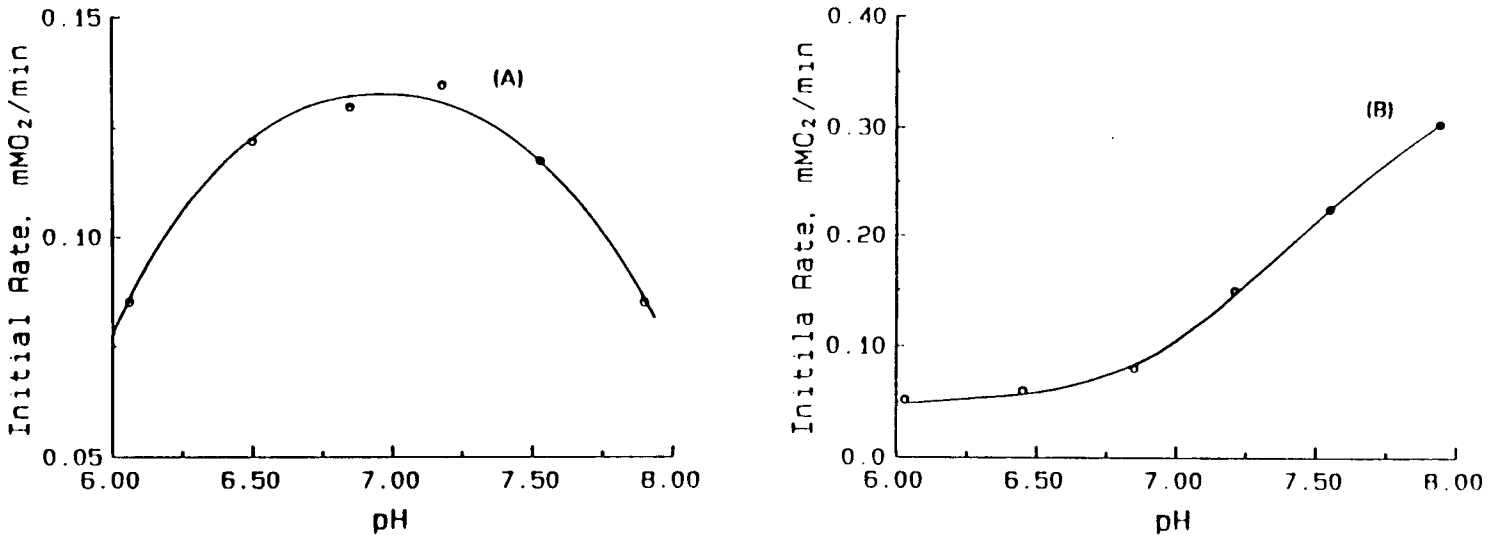

Figure 1.10. pH effects on the iron oxidation in apoferritin at low (A) or high (B) initial Fe^{2+} loading. Conditions: (A) [apoferritin] = 8.3 μM, $[Fe^{2+}]_o$ = 0.11 mM, $[O_2]_o$ = 0.27 mM, in 0.1 M NaCl, 25 mM Mops, 25 mM Mes; (B) [apoferritin] = 2.08 μM, $[Fe^{2+}]_0$ = 0.67 mM, $[O_2]_o$ = 0.27 mM, in 0.1 M NaCl, 25 mM Mops, 25 mM Mes, 20 ^{0}C. File name: "Jul032 (A) Jul151 (B)"

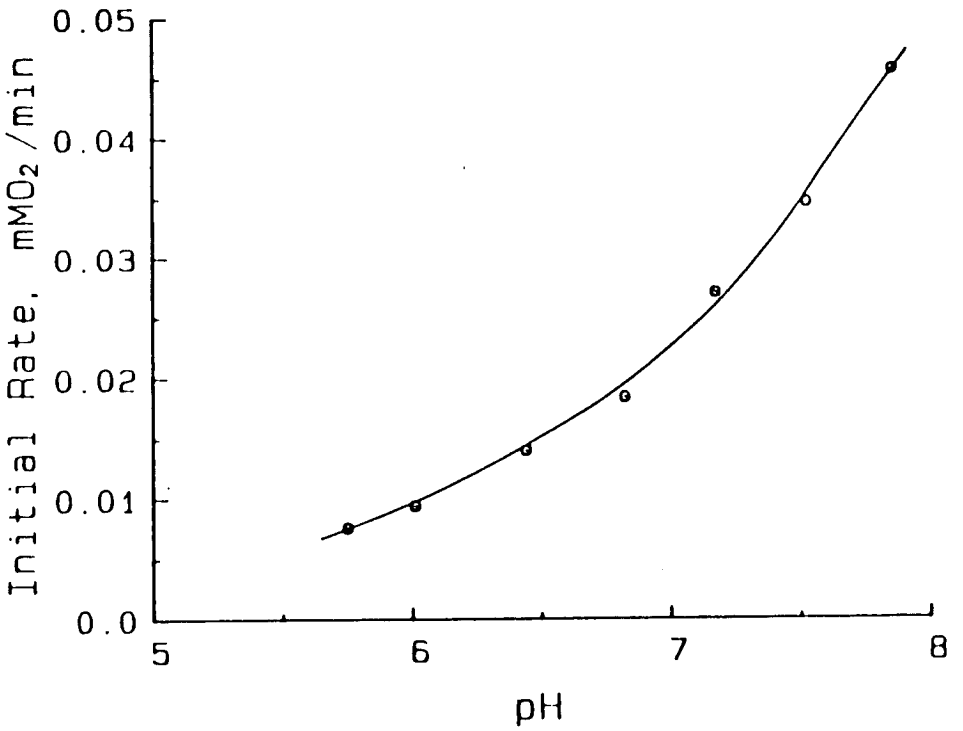

Figure 1.11. pH effect on the iron oxidation in ferritin containing an iron(III) core. Conditions: [apoferritin] = 2.08 μM, Fe^{3+}/protein = 340, $[Fe^{2+}]_0$ = 0.09 mM, $[O_2]_0$ = 0.28 mM, in 50 mM Mops, 50 mM Mes, 20 ^{0}C. File name: "Oct081"

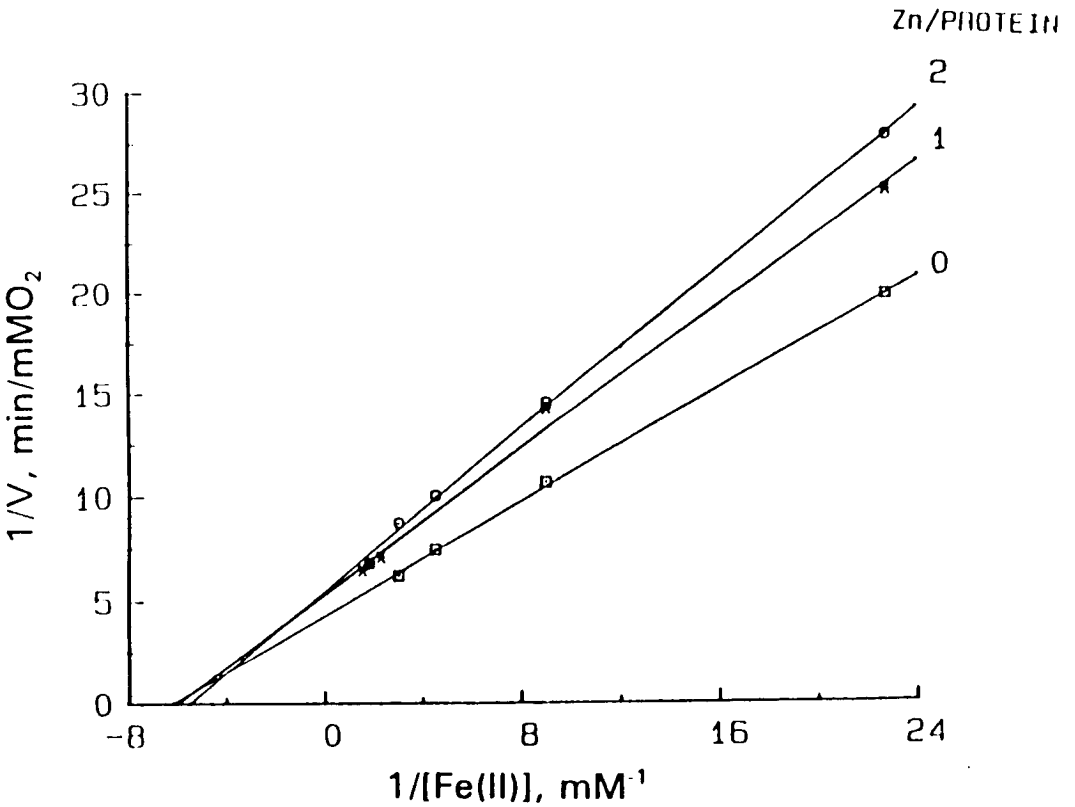

Figure 1.12. Lineweaver-Burk plots for noncompetitive inhibition of iron(II) oxidation by zinc(II) with fixed Zn^{2+}/protein ratios of 0, 1, and 2. Least-squares lines are shown. Conditions: [apoferritin] = 8.3 μM, $[O_2]_o$ = 0.28 mM, in 0.1 M NaCl, 50 mM Mops, pH 7.05, 20°C. File name: "Sep224, Sep225 and Oct012"

becomes competitive (Fig. 1.13).

To model the competitive inhibition, we assume that Zn^{2+} competes with Fe^{2+} for binding at the ferroxidase site, *viz.*

$$Zn^{2+}\text{-}P \overset{K_I}{\rightleftarrows} Zn^{2+} + P \qquad (1.15)$$

Here the Zn^{2+}-P complex thus formed is assumed to be kinetically incompetent. By combining the appropriate rate expressions for reactions 1.3, 1.4, 1.5 and 1.15 in the usual manner, one obtains the following Lineweaver-Burk equation for competitive inhibition. The detailed zinc inhibition mechanism and derivation of equation (1.16) are described in Appendix I.

$$\frac{1}{V} = \frac{2}{[P]_o}\left[\frac{1}{k_1}\left(1 + \frac{[Zn^{2+}]}{K_I}\right)\frac{1}{[Fe^{2+}]} + \frac{k_3+k_{-2}}{k_2k_3[O_2]} + \frac{1}{k_3}\right] \qquad (1.16)$$

In this expression, $[Zn^{2+}]$ and $[Fe^{2+}]$ are the free Zn^{2+} and Fe^{2+} concentrations; for purposes of graphing equation 1.16, they are assumed to be the same as the *total* concentrations $[Zn^{2+}]_o$ and $[Fe^{2+}]_o$. Plots of 1/V versus $1/[Fe^{2+}]_o$ should be linear with slopes scaled by $1 + [Zn^{2+}]_o/K_I$ as is observed experimentally in Figure 1.13. The average value of K_I = 67 ± 11 μM was obtained from experiments where $[Zn^{2+}]_o$ was held constant and $[Fe^{2+}]_o$ varied, and vice versa (*vide infra*).

Figure 1.14, shows the reduction in the initial rate of Fe^{2+} oxidation as a function of added $[Zn^{2+}]_o$ while holding the total ferrous ion concentration $[Fe^{2+}]_o$ constant.

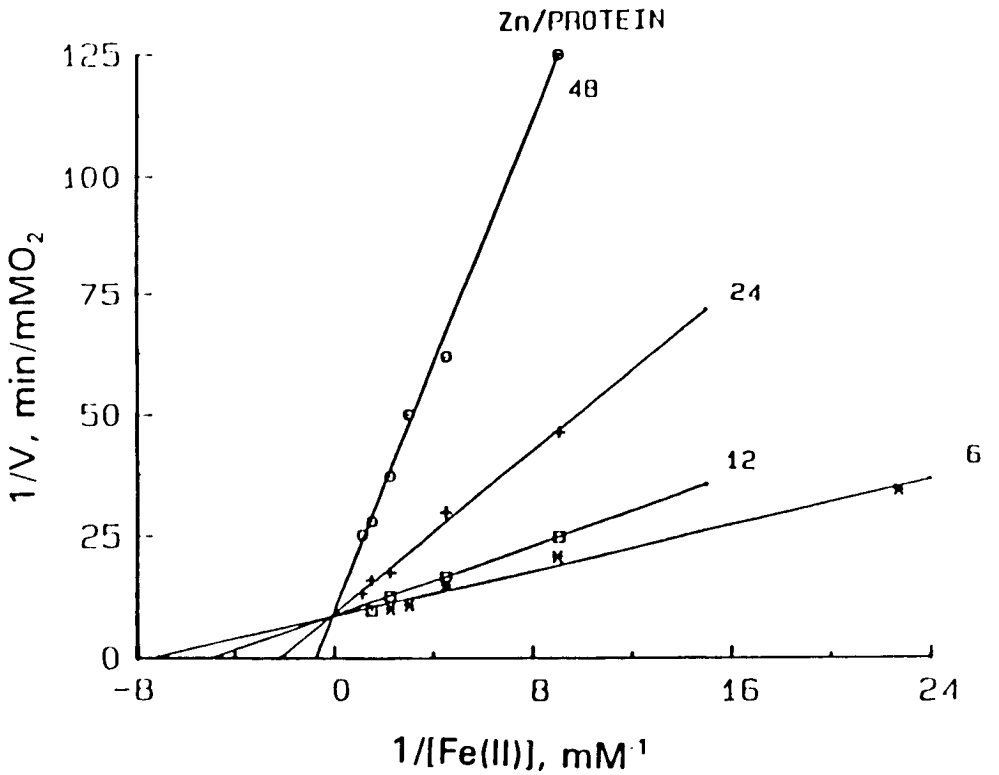

Figure 1.13. Lineweaver-Burk plots for competitive inhibition of iron(II) oxidation by zinc(II) with fixed Zn^{2+}/protein ratios of 6, 12, 24, and 48. Least-squares lines are shown. Conditions are the same as in Figure 6. File name: "Sep012, Sep017, Sep032 and Sep202"

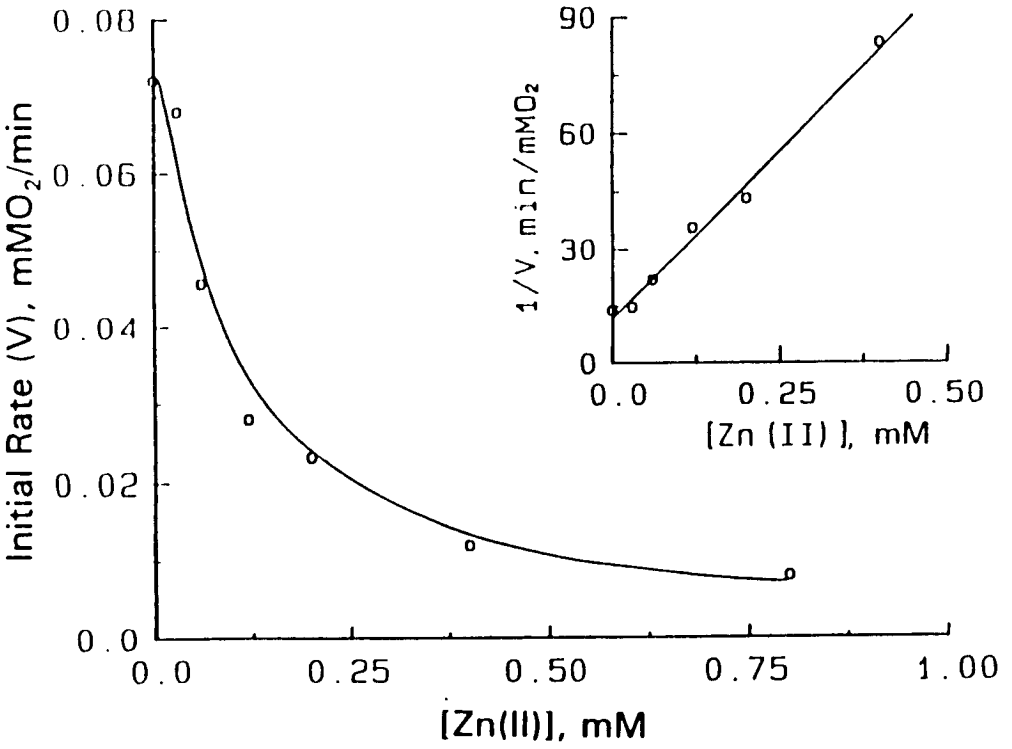

Figure 1.14. Competitive inhibition of iron(II) oxidation by added zinc(II) at a fixed iron(II) concentration. The line for the least-squares fit to equation 12a is shown. Conditions: [apoferritin] = 8.3 μM, $[Fe^{2+}]_o$ = 0.222 mM, $[O_2]_o$ = 0.28 mM in 0.1 M NaCl, 50 mM Mops, pH 7.05, 20°C. File name: "Sep010 and Sep011 (inset)"

Equations 1.17(a-e) describe the dependence of initial rate on added Zn^{2+}, assuming competitive binding between Zn^{2+} and Fe^{2+}.

$$V = k_1[Fe^{2+}]_o \left\{\frac{-b + \sqrt{b^2 - 4ac}}{2a}\right\} \quad (1.17a)$$

$$a = (1 + \alpha[Fe^{2+}]_o)/K_I \quad (1.17b)$$

$$b = 1 + \alpha[Fe^{2+}]_o + ([Zn^{2+}]_o - [P]_o)/K_I \quad (1.17c)$$

$$c = -[P]_o \quad (1.17d)$$

$$\alpha = k_1/k_3 + (k_1/k_2 + k_{-2}k_1/k_3k_2)/[O_2]_o \quad (1.17e)$$

The data in Figure 1.14 were least-squares fitted to equation 1.17a with a, b, c and α given by equations 1.17b through 1.17e. k_1 was set equal to 178 $mM^{-1}min^{-1}$ (Table 1.1) and the parameters K_I, and α were optimized. A value of K_I = 41 ± 7 μM was obtained in reasonably good agreement with the average value of 67 ± 11 μM from all of the zinc inhibition experiments.

Inhibition Effect of Other Metal Ions

In addition to zinc, some other metal ions were also found to be inhibitors of the iron(II) oxidation in apoferritin (Treffry et al., 1977; Crichton et al., 1980). To resolve the number of the ferroxidase sites on horse spleen ferritin, the effect of a number of metal ions, including Rh^{3+}, Cd^{2+}, Cu^{2+}, Co^{2+} and Tb^{3+}, on the rate of iron oxidation was examined. But the inhibition effects of these metal ions are smaller compared to that of Zn^{2+}. The

initial rate of O_2 consumption in the presence of those metal ions are summarized in Table 1.2. The presence of about 24 to 60 Cr^{3+} per apoprotein molecule also partially inhibits the iron oxidation reaction (Table 1.3). However, the EPR spectrum of 0.22 mM Fe^{3+} in the solution containing 24 Cr^{3+}/protein exhibited almost no g'= 4.3 signal (data not shown). Therefore, similar to Tb^{3+} (see Chapter 3), Cr^{3+} must bind tightly at the EPR active monomeric Fe^{3+}-protein binding sites.

The Effect of the Iron Core on Rate of Iron Oxidation

A series of experiments was undertaken to examine the influence of the core on the iron(II) oxidation kinetics. Samples of ferritin containing iron up to 1,200 Fe^{3+}/protein were prepared by adding ferrous sulfate heptahydrate to the apoprotein and allowing the sample to incubate in air for 24 hr (Materials and Methods). Iron(II) was then added to these samples in increments of 10, 26, 52, 105, and 160 Fe^{2+}/protein and the initial rate of Fe^{2+} oxidation measured. The results shown in Figure 1.15 indicate that the presence of core has little effect on the observed rate provided that the increment of iron(II) added is 52 Fe^{2+}/protein or less. Thus all of the iron appears to be oxidized via the protein catalyzed pathway under these conditions. However, when the higher Fe^{2+}/protein increments of 105 and 160 Fe^{2+}/protein are employed, sigmoidal curves are observed, indicating the onset of

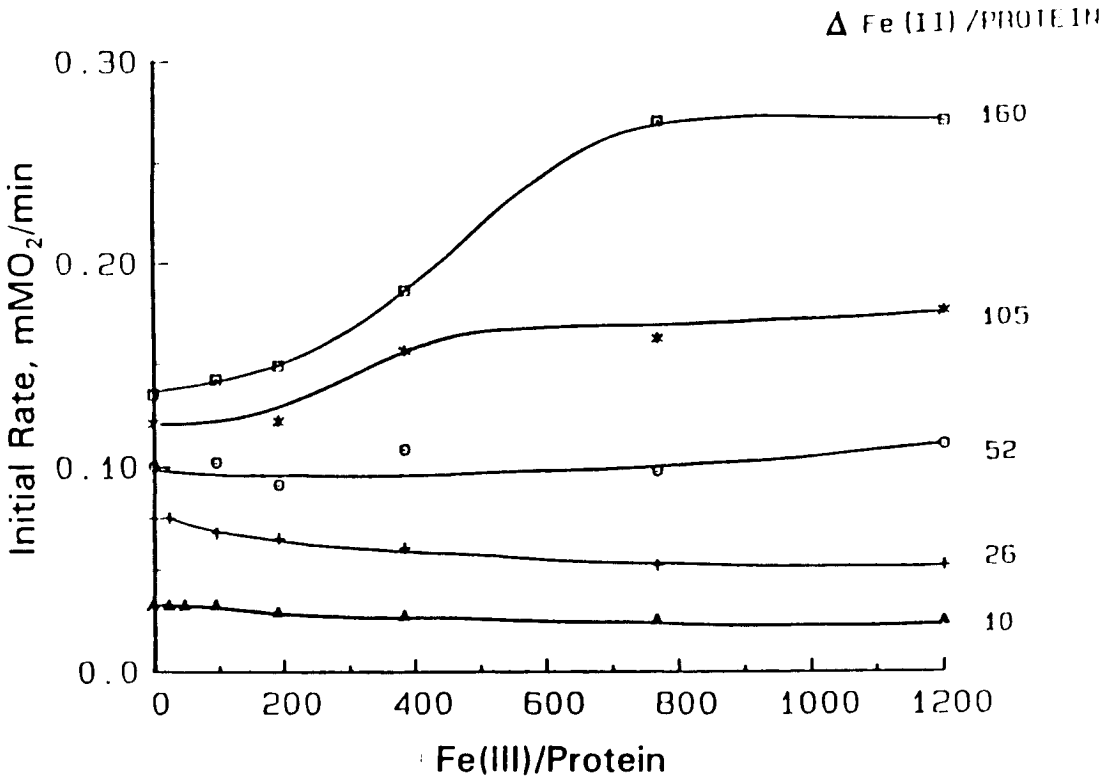

Figure 1.15. Dependence of the initial rate of oxygen consumption on the increment of iron(II) added and on the amount of iron already present in ferritin. Increments of iron(II), (ΔFe^{2+}), were added to samples of ferritin containing from 0 to 1200 Fe^{3+}/protein and the initial rates of oxygen uptake measured. Conditions: [ferritin] = 4.2 μM, $[O_2]_o$ = 0.28 mM, in 0.1 M NaCl, 75 mM Mops, pH 7.05, 20°C. File name: "Oct181, Oct241-Oct244"

TABLE 1.2

Inhibition of Iron Oxidation in Horse Spleen Apoferritin by Various Metal Ions[1]

Metal ion	Initial rate (μM O_2/min)	Relative Rate
No metal	62	100
Ru^{2+}	49	79
Cd^{2+}	49	79
Co^{2+}	44	71
Tb^{3+}	43	69
Cu^{2+}	40	64
Zn^{2+}	24	39

[1]Conditions: [apoferritin] = 4.2 μM, [Fe^{2+}] = 0.11 mM, [M^{n+}] = 0.055 mM, [O_2]0 = 0.28 mM, [NaCl] = 0.1 M, [Mops] = 50 mM, pH 7, 20 ^{0}C.

TABLE 1.3

Cr^{3+} Inhibition of Iron Oxidation in Horse Spleen Ferritin[1]

[Cr^{3+}], mM	0.0	0.2	0.3	0.4
V_0, mMO_2/min	0.19	0.054	0.048	0.054

[1]Conditions: [apoferritin] = 8.3 μM, [Fe^{2+}] = 0.22 mM, [NaCl] = 0.1 M, [Mops] = 0.2 M, pH 7.2, 20 ^{0}C.

another mechanism for iron oxidation, presumably involving the mineral surface. The Fe^{2+}/O_2 stoichiometry increased from 2 to 4 from the low to the high end of the sigmoidal curve as predicted by equations 1.1 and 1.2.

Fe/O_2 Stoichiometry

The stoichiometry of iron oxidation during the reconstitution of ferritin was determined from the amount of O_2 consumption following complete oxidation. Figure 1.16 shows the stoichiometry of iron oxidation in horse spleen apoferritin as a function of the amount of added Fe^{2+} per protein molecule by electrode oximetry. The observation that Fe/O_2 stoichiometry changes from 2 to 4 with increasing Fe^{2+}/protein ratios is in good accord with the previous reported results using ^{16}O mass spectroscopy (Xu & Chasteen, 1991). It was also found that the Fe/O_2 stoichiometry increased with increasing pH at low Fe/protein ratios of 13. The stoichiometry of iron oxidation as a function of pH is plotted in Figure 1.17.

Phosphate Effect

Experiments were also carried out to examine the effects of phosphate on the rate of oxidation of iron. Figure 1.18 demonstrates that phosphate has little effect on the initial rate of iron oxidation. Under the conditions used previously in Mössbauer studies of Fe^{2+} oxidation in apoferritin (1 mM Fe^{2+}, 83 μM apoprotein with or without 1

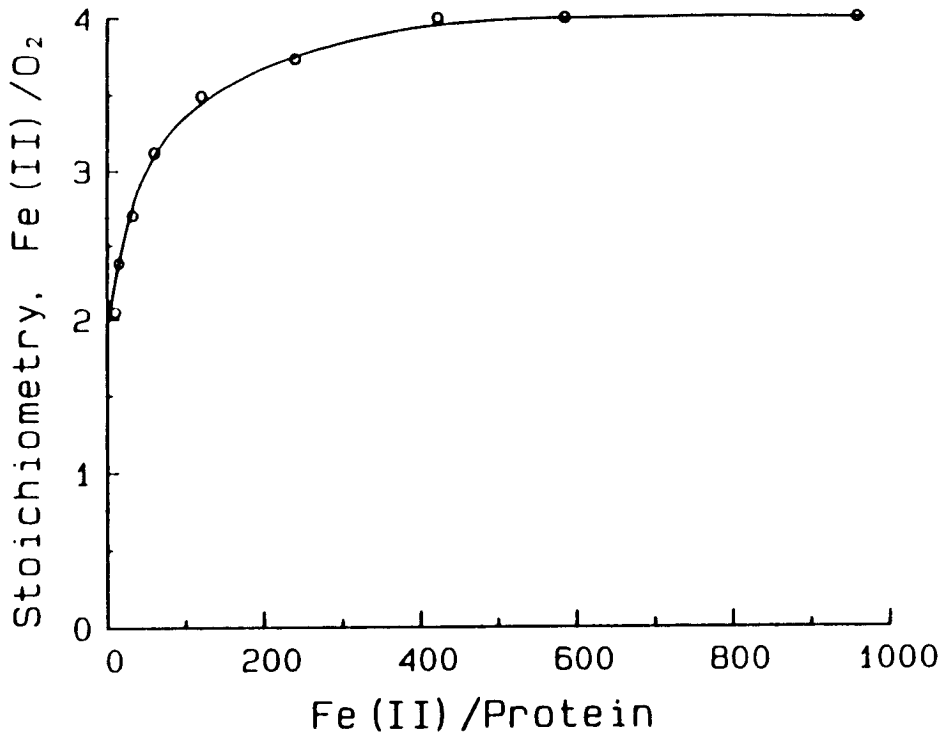

Figure 1.16. Stoichiometry of iron oxidation as a function of the Fe^{2+}/protein ratio in horse spleen apoferritin. Conditions: $[Fe^{2+}]_0$ = 0.44 mM, $[O_2]$ = 0.28 mM, in 0.1 M NaCl, 50 mM Mops, pH = 7.0, 20 ^{0}C. The Fe^{2+}/protein ratio was increased by decreasing the protein concentration. File name: "91jun15"

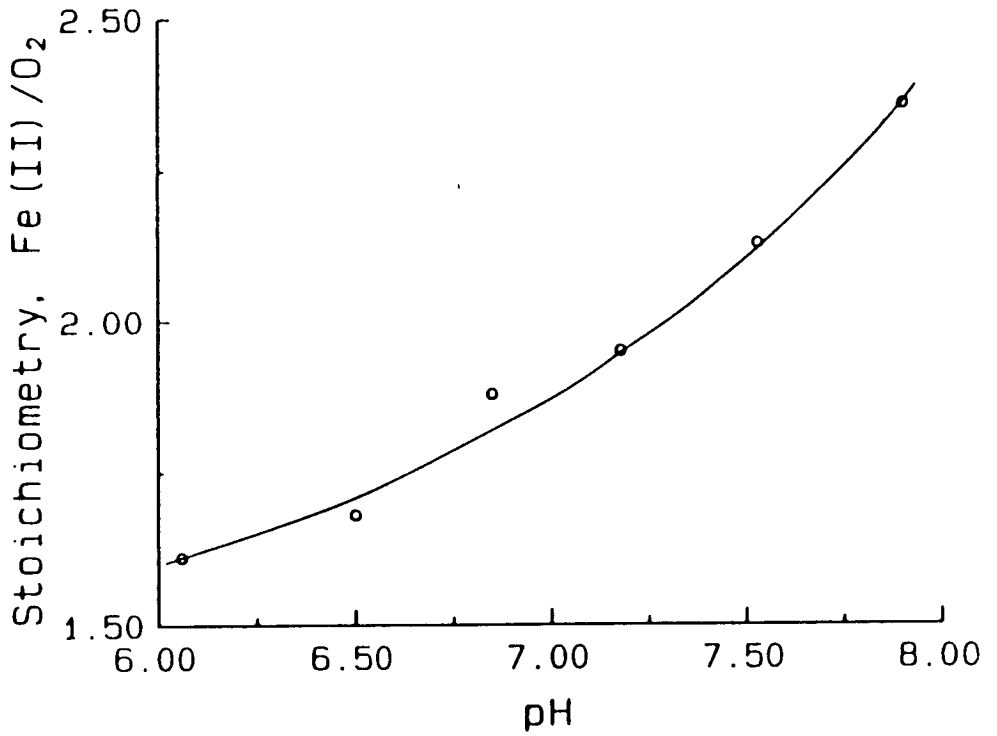

Figure 1.17. Stoichiometry of iron oxidation as a function of pH at low iron/protein ratio. Conditions: [apoferritin] = 8.3 μM, $[Fe^{2+}]_o$ = 0.11 mM, $[O_2]_o$ = 0.27 mM, in 0.1 M NaCl, 25 mM Mops, 25 mM Mes, in 0.1 M NaCl, 25 mM Mops, 25 mM Mes, 20 ^{0}C. File name: "Jul031"

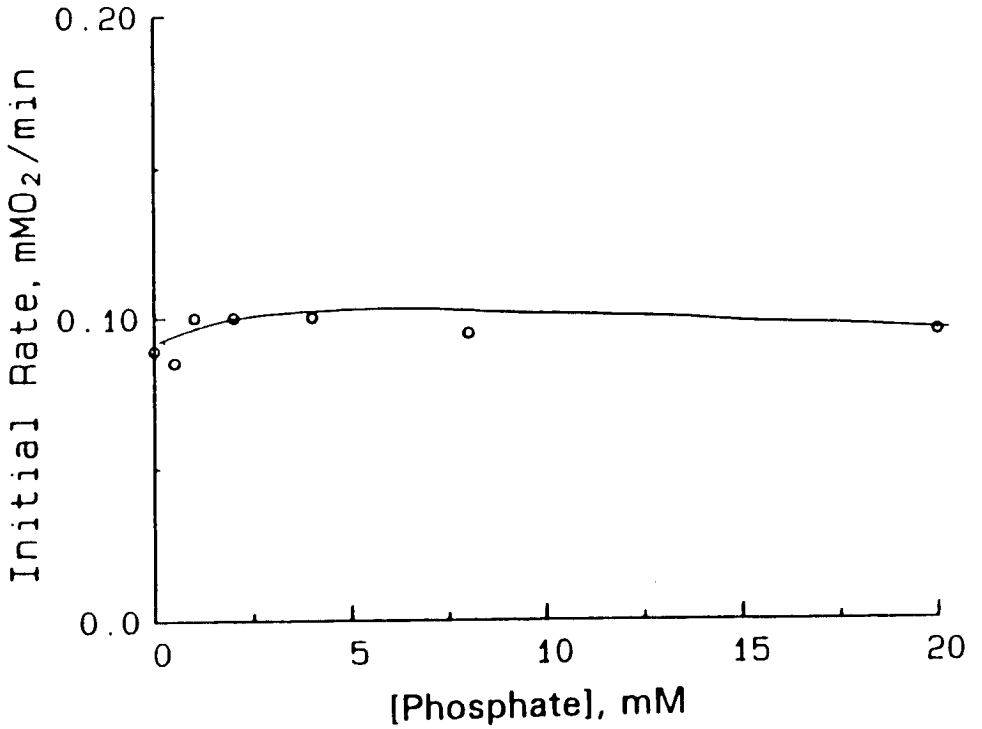

Figure 1.18. Phosphate effect on the rate of oxygen consumption. Conditions: [apoferritin] = 4.2 μM, $[Fe^{2+}]_0$ = 0.11 mM, $[O_2]_0$ = 0.27 mM, in 0.1 M NaCl, 50 mM Mops, pH 6.9, 21 ^{0}C. File name: "93my171"

mM P_i (phosphate) in 0.1 M Hepes, pH 7.55, 0°C) pseudo first order rate constants of 0.44 ± 0.02 min^{-1} and 0.42 ± 0.02 min^{-1} in the presence and absence of P_i, respectively were obtained compared with 0.45 ± 0.07 min^{-1} and 0.25 ± 0.02 min^{-1} from Mössbauer experiments (Cheng & Chasteen, 1990). Thus the present work is at variance with the previous observation from this laboratory that P_i accelerates iron oxidation in apoferritin at low Fe^{2+} loading (12 Fe/apoferritin) of the protein.

Catalase Activity

Part of the H_2O_2 produced in the iron oxidation reaction ultimately disproportionates to O_2 and H_2O via the catalase reaction 1.18 as evidenced by a

$$H_2O_2 \rightarrow \tfrac{1}{2}O_2 + H_2O. \qquad (1.18)$$

slow evolution of O_2 over a period of 5 - 30 min after iron(II) oxidation was complete. About one third of the O_2 which had been originally consumed in the oxidation reaction was observed to be regenerated. This value is smaller than what is predicted from equations 1.1 and 1.18 (Fig. 1.19). Apoferritin has no catalase activity since the rate of O_2 production when H_2O_2 was added to buffer was the same whether or not protein was present, while the presence of holoferritin inhibited the disproportionation of H_2O_2. The reason for this inhibition is not clear.

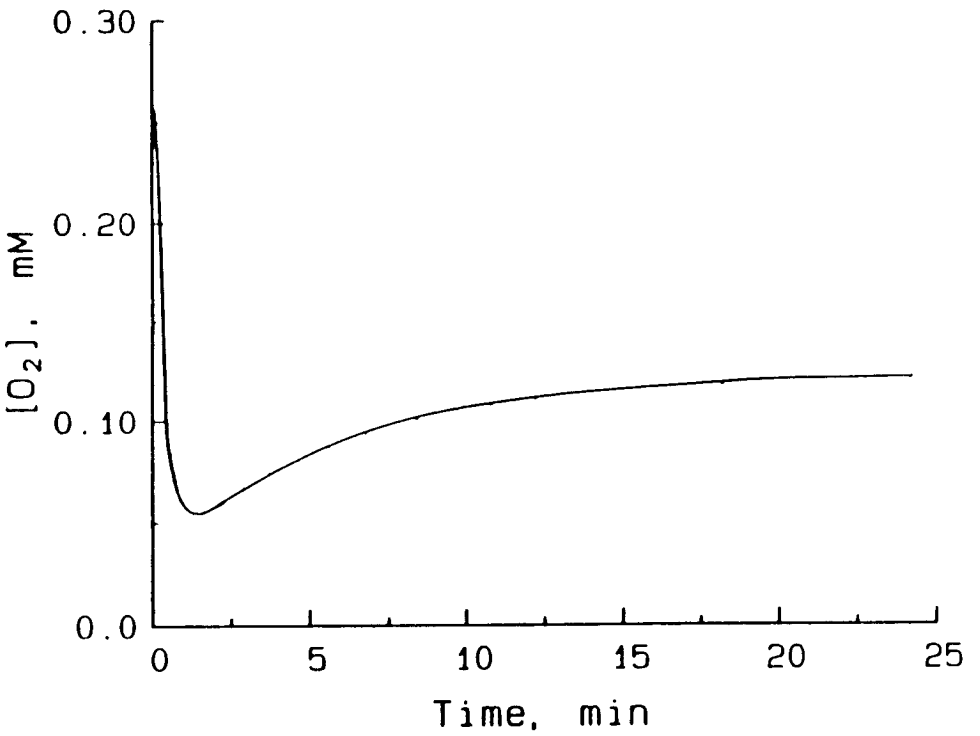

Figure 1.19. Evidence of H_2O_2 disproportionation. Conditions: [apoferritin] = 16.7 μM, $[Fe^{2+}]_0$ = 0.5 mM, $[O_2]_0$ = 0.28 mM in 0.1 M NaCl, 50 mM Mops, pH 7.05, 20 ^{0}C. File name: "93ap121"

DISCUSSION

The present work has revealed several new aspects of the oxidation chemistry of iron(II) in apoferritin and ferritin. The results demonstrate that ferritin behaves as a ferroxidase having kinetic properties characteristic of a true enzyme. However, ferritin is unique in that the product of the reaction, Fe^{3+}, is stored within the protein itself. The present findings are in accord with the previous reported work (Bakker & Boyer, 1986) showing ferroxidase activity in apoferritin from studies of the apoferritin catalyzed formation of the Fe^{3+}-transferrin from Fe^{2+} and dioxygen.

The location of the ferroxidase sites within the protein is of special interest. The horse spleen protein used in the present study is a heteropolymer consisting of 16% H and 84% L subunits. Since the residues constituting the ferroxidase site in the H-subunit of the human protein, namely Glu-27, Glu-62 and His-65 (Lawson et al., 1989, 1991), are conserved in the H-subunits of all species, it seems likely that the ferroxidase activity observed with the horse spleen protein resides in the H-subunit but is perhaps influenced by the presence of L-subunit (Chapter II). The existence of L-subunit ferroxidase sites is not precluded by the present data. Attempts to quantify the number of ferroxidase sites by metal ion inhibition, and thereby confirm their presence on the H-subunit only, were

unsuccessful. None of the metal ion employed in the inhibition study is able to completely eliminate the catalytic activity of apoferritin (Table 1.2). Experiments in which the kinetically inert Cr^{3+} ion was bound to the apoprotein by the anaerobic addition of Cr^{2+} to apoferritin followed by O_2 gave only partial inhibition of the enzyme; 29% of the ferroxidase activity still remained at a Cr^{3+}/apoferritin ratio of 60 (Table 1.3).

The kinetic parameters summarized in Table 1.1 fall in the range typical of many enzymes (Walsh, 1979; Zerner *et* al., 1964). The overall effectiveness of an enzyme is given by the "apparent bimolecular rate constant" $k_2' = k_{cat}/K_m$, which takes into account the degree of saturation of the active site by substrate. For ferritin, this value is $k_2' = k_{cat}/K_{m,O2} = 9.5 \times 10^3\ M^{-1}s^{-1}$ which is comparable to the value for chymotrypsin (Zerner et al., 1964). Here k_2' is the second-order rate constant for the oxidation of the Fe^{2+}-P complex, *viz.* $-d[O_2]/dt = k_2'[Fe^{2+}\text{-}P][O_2]$. The k_2' value for apoferritin is well below the limiting value of $10^9\ M^{-1}s^{-1}$ for a diffusion-controlled reaction (Walsh, 1979); however, it is one to three orders of magnitude higher than typically found for Fe^{2+} chelates (Kurimura et al., 1968; Kurimura & Kuriyama., 1969), *e.g.* $k_2' = 77\ M^{-1}s^{-1}$ for Fe^{2+}-NTA (Materials and Methods). It is well known that complexation of Fe^{2+} by oxygen donor or mixed oxygen-nitrogen donor chelates accelerates its oxidation (Kurimura & Kuriyama, 1969) but apoferritin complexation appears to be particularly

effective in this regard.

The enthalpy of activation $\Delta H^{\ddagger}$ = 34.2 kJ/mol for k_1 of reaction 1.3 (Fig. 1.9, Table 1.1) falls in the range of most enzymes (Segel, 1975) and is comparable to $\Delta H^{\ddagger}$ for ligand exchange and oxidation reactions of simple Fe^{2+} complexes (Eigen & Wilkins, 1965; Hewkin & Prince, 1970; Wilkins, 1991; Borggard, 1972; Sasa et al., 1987; Ng & Henry, 1980). The value obtained for k_1, however, is two orders of magnitude lower than found for ligand exchange in simple Fe^{2+} chelates (Eigen & Wilkins, 1965; Hewkin & Prince, 1970). The low value of k_1 for apoferritin and the relatively large negative entropy of activation $\Delta S^{\ddagger}$ = -108 J/mol-K for the reaction perhaps reflects significant changes in protein ligand conformation when Fe^{2+} binds. Smaller entropy changes are commonly observed upon complexation of Fe^{2+} by small chelates (*e.g.* Hewkin & Prince, 1970).

When a small amount of Fe^{2+} is introduced to apoprotein solution (Fe/protein ratio = 13), the pH profile for the ferroxidase reaction has a maximum near pH 7 (Fig. 1.10, curve A) and is similar in shape to activity-pH curves commonly found for enzymes. At higher Fe/protein ratio, however, the initial rate of iron oxidation in apoferritin increased continuously with increasing pH (Fig. 1.10, curve B). The dramatically different behaviors in pH profile between the low and high initial iron loadings can be explained according to the iron oxidation and deposition

chemistry in apoferritin. Basically, there are two driving forces for Fe^{2+} oxidation in apoferritin, one is from the ferroxidase activity of the ferritin shell, the other is the tendency of Fe^{3+} hydrolysis. At higher iron/protein ratio, Fe^{3+} hydrolysis overshadows the ferroxidase activity, especially at higher pH values. The enzyme-catalyzed reaction, however, dominates at lower iron/protein ratio, and therefore a bell-shaped pH profile is observed. Such curves are usually attributed to the existence of more than one protonation state of the enzyme and/or substrate (Segel, 1975; Roberts, 1977). Similar pH profiles for the rate of oxidation of simple iron(II) chelates have been observed and ascribed to a combination of deprotonation of coordinating functional groups and hydrolysis of the Fe^{2+} (Kurimura et al., 1968; Kurimura & Kuriyama, 1969). In the case of ferritin, the $pK_a \approx 6\text{-}7$ of histidine, one of the ligands in the H-subunit ferroxidase site (Lawson et al., 1989, 1991), falls in the appropriate range for affecting the observed rate changes with pH.

Nevertheless, at Fe^{2+}/protein = 13 the stoichiometry of iron oxidation increased from 1.6 to 2.5 at a pH range of 6 - 8 (Fig. 1.17). This indicates that even though the enzyme-catalyzed mechanism is more effective at lower Fe^{2+}/protein ratios, a small amount of Fe^{2+} is still oxidized following the Fe^{3+} hydrolysis pathway. Thus, the bell-shape of the rate-pH curve observed in Figure 1.10A is quite shallow compared to commonly found activity-pH curves for

enzymes (Segel, 1975; Roberts, 1977). In addition, when a small iron core (320 Fe/protein) is present in ferritin, the initial rate of iron oxidation increases rapidly with increasing pH upon the second addition of a small amount of Fe^{2+} (Fig. 1.11), suggesting the domination of the Fe^{3+} hydrolysis mechanism in this instance.

Either Mechanism is consistent with the observed kinetic data; However, Mechanism II would account for the failure of previous studies to spin-trap any "free" superoxide radical during the oxidative deposition of iron in apoferritin (Xu & Chasteen, 1991; Grady et al., 1989) as well as the lack of any effect of added superoxide dismutase on the rate.[1,2] The kinetic data suggest that Fe^{2+} oxidation occurs in two one-electron steps to produce H_2O_2 rather than in a concerted 2-electron step, regardless of the mechanism of iron(II) oxidation in ferritin.

It is reasonable to assume that the inhibitory effect of Zn^{2+} on Fe^{2+} oxidation is due to binding of both metals at the ferroxidase site(s). The observed inhibition is complicated, however, suggesting noncompetitive inhibition at low Zn^{2+}/protein ratios (Fig. 1.12) which becomes competitive upon addition of further Zn^{2+} (Fig. 1.13). These observations indicate the presence of at least two types of zinc binding sites (the non-competitive inhibition effect observed at lower Zn^{2+} concentration may be from the heterogeneity of the apoferritin sample). The zinc inhibition results are also in keeping with x-ray

crystallographic data on the horse spleen protein showing at least four binding sites for zinc as well as other metals (Harrison et al., 1986; Treffry et al., 1984). Some of these zinc sites may be important functionally.

Figure 1.15 shows that there are clearly two pathways for iron oxidation in ferritin. In the protein catalysis model proposed by Crichton and Roman (1978), the protein is postulated to be involved in oxidation of the iron(II) at all stages of core formation. Our data indicate that this model is operable as long as the iron is delivered to the protein in sufficiently small increments (<50 Fe^{2+}/protein), which results in an initial rate of oxidation essentially independent of the amount of iron(III) already present in the protein (Fig. 1.15). In contrast, the crystal-growth model appears to be operable when iron(II) is delivered to the protein in increments exceeding 50 Fe^{2+}/protein. In this model, iron is initially oxidized on the protein but once sufficient core has developed, iron oxidation and deposition occurs directly on the growing mineral surface (Macara et al., 1972, 1973). Kinetic curves with sigmoidal shapes are predicted by this model (Macara et al., 1972, 1973) as observed in Figure 1.15. Evidently when large increments of Fe^{2+} are employed, the protein catalysis pathway becomes saturated, resulting in the excess Fe^{2+} being shunted to the mineral surface upon which it is oxidized. Whether the protein ferroxidase pathway or both pathways operate in a particular situation of course depends

on the immediate flux of iron into the protein.

The fate of the H_2O_2 produced in the overall reaction 1 is of particular interest. H_2O_2 and Fe^{2+}-apoferritin have been shown to participate in the Fenton reaction 1.19 to produce hydroxyl radical but the yield of spin-trapped

$$Fe^{2+} + H_2O_2 \rightarrow Fe^{3+} + OH\cdot + OH^- \qquad (1.19)$$

secondary radicals was quite low (Chapter III; Grady et al., 1989). However, only part of the H_2O_2 produced during iron oxidation (equation 1.1) ultimately disproportionates essentially to O_2 and H_2O by reaction 1.18 (Fig. 1.19). The presence of catalase in protein solution only enhanced the stoichiometry from 2 to about 3.2. Thus, some of the H_2O_2 produced were not accessible to catalase. Two hypotheses concerning the fate of the rest of the H_2O_2 have been proposed. (1) As an oxidant, H_2O_2 may oxidize some amino acid on the protein shell; (2) Fe^{3+}-O-O-Fe^{3+} may be formed and deposited in the iron core during iron oxidation. Experiments were designed in an attempt to test each hypothesis. (1) A ferritin sample containing 168 Fe^{3+}/protein was prepared by successive addition of 24 Fe^{2+} per protein, so that the oxidative amino acids on the protein shell would be completely oxidized by the H_2O_2 produced in each addition of Fe^{2+}. Then, an additional amount of Fe^{2+} was introduced to the ferritin sample, all the H_2O_2 formed this time should go through the

disproportionation reaction supposing the first assumption is correct. (2) 0.2 mM Fe^{2+} was injected to 8.3 μM ferritin solution in the sample cell, followed by addition of microliter amounts of concentrated HCl to the ferritin solution immediately after the completion of iron oxidation in order to bring down the pH of the sample to < 2.0. Under these conditions, the ferritin shell would be denatured and the iron core dissolved. Thus more O_2 should be released if the Fe^{3+}-O-O-Fe^{3+} was formed as proposed above. However, these experiments did not provide us with the anticipated results. Nevertheless, oxidative damage to the protein does occur to some extent when iron is oxidatively deposited in ferritin with O_2 as the oxidant; a loss in histidine and lysine residues (de Silva et al., 1992) and the formation of protein derived radicals have been shown to occur during this process (Grady et al., 1989; Grady & Chasteen, 1991).

CHAPTER FOOTNOTES

[1.1]All of the iron(II) is oxidized under the conditions of the experiment as demonstrated by Mössbauer spectroscopy (Xu & Chasteen).

[1.2]Comparison of curves A and B of Figure 4 show that O_2 from the dismutase reaction is initially produced at a faster rate in the presence of Fe^{2+}-apoferritin than with apoferritin (2-4 times faster depending on the experiment), indicating enhanced superoxide dismutase activity from the Fe^{2+}. Iron(II) at the same concentration in buffer with protein present also enhances SOD activity (a phenomenon known to occur with redox active metals (McClune et al., 1977) but only about half as much as Fe^{2+}-apoferritin itself (data not shown). Therefore, it is evident that the Fe^{2+}-apoferritin complex itself facilitates the dismutation of superoxide, albeit weakly so. Neither apoferritin or holoferritin display significant superoxide dismutase activity relative to buffer alone. Addition of bovine superoxide dismutase to solutions containing iron(II), O_2, and apoferritin has no effect on the rate of iron(II) oxidation, suggesting that the O_2^- produced within the protein during Fe^{2+} oxidation either preferentially undergoes the ferritin catalyzed dismutation reaction or remains bound to the iron and is unavailable to the bovine SOD enzyme. As expected, addition of bovine catalase halves the rate of O_2 consumption (not the rate of iron(II) oxidation) since O_2 is produced in the catalase reaction $2H_2O_2 \rightarrow 2H_2O + O_2$, H_2O_2 being a product of Fe^{2+} oxidation.

CHAPTER II

FERROXIDASE KINETICS OF HUMAN LIVER APOFERRITIN, RECOMBINANT H-CHAIN APOFERRITIN AND SITE-DIRECTED MUTANTS

INTRODUCTION

The kinetic studies described in Chapter I revealed that horse spleen ferritin is a true enzyme, exhibiting ferroxidase activity which is characterized by saturation kinetics with respect to the substrates Fe^{2+} and O_2 and first-order kinetics with respect to the protein. The protein catalyzes reaction 1 in which hydrogen peroxide is the principal product of dioxygen reduction (Xu & Chasteen, 1991).

$$2Fe^{2+} + O_2 + 4H_2O \longrightarrow 2FeOOH_{core} + H_2O_2 + 4H^+ \qquad (2.1)$$

The role of the two different subunits in iron oxidation and core formation has been the subject of considerable study. Ferritin molecules containing a large percentage of H subunits show faster rates of iron uptake (Worwood, 1990; Wagstaff & Jacobs, 1978), while those with a large percentages of L subunit tend to sequester more iron in their inner cavity (Artymiuk et al., 1991; Lawson et al., 1991). Site-directed mutagenesis and x-ray crystallographic

studies of the Tb^{3+} derivative of recombinant H-chain apoferritin of human liver (rHF) have located a putative ferroxidase center on the H-chain involving two metal binding sites, A and B, only 3 Å apart (Lawson et al., 1989; 1991). Site A involves residues Glu-27, Glu-62, His-65 and Glu-107 as ligands to Tb^{3+}, and site B residues Glu-61, Glu-62 and Glu-107. Residues Glu-61 and Glu-107 bridge between the two sites. Glu-27, Glu-62 and His-65 are not conserved in the L-subunit so it lacks the putative ferroxidase center. A third Tb^{3+} site (site C) composed of residues Glu-61, Glu-64 and Glu-67 is present near the ferroxidase center. This site, which is conserved in both H and L subunits, has been postulated to be a nucleation site for formation of the ferrihydrite mineral core (Lawson et al., 1991; Levi et al., 1992). L-chain ferritins, while lacking the putative ferroxidase center, are capable of forming cores, albeit much slower than H-chain ferritins (Levi et al., 1989; 1992).

The previous kinetic study of the ferroxidase activity of horse spleen ferritin was unable to address the question of the role of H and L subunits in enzymatic activity since the protein used was a heteropolymer containing 16% H and 84% L subunits (Chapter I). In the following work, we examined iron(II) oxidation in recombinant H-chain apoferritin and in recombinant L-chain apoferritin (rLF), both homopolymer proteins, and in human liver ferritin (HLF) which is a heteropolymer of 4% H and 96% L subunits. Three

H-chain site-directed mutants were also studied: mutant 222 in which the two ligands Glu-62 and His-65 of the putative ferroxidase center are changed (E62K, H65G and also K86Q); mutant A2 in which the putative nucleation site ligands Glu-61, Glu-64 and Glu-67 are changed (E61A, E64A, E67A), and mutant S1 having both the putative ferroxidase center and nucleation site ligands changed (E61A, E62K, E64A, H65G, E67A, and also D42A, K86Q) (Levi et al., 1991; 1992; Wade et al., 1991). In addition, the kinetic measurement of sheep spleen ferritin containing 66% H and 34% L was also performed. Furthermore, the catalytic activities of a series of recombinant human apoferritins which accommodate a varying amount of H and L subunits are compared based on the percentage of the H chain.

The rate of iron(II) oxidation was measured directly using a rapid response oxygen electrode (Chapter I) as opposed to earlier studies in which iron oxidation was measured indirectly or the color development associated with core formation was monitored (*e. g.* Levi et al., 1988; Wade et al., 1991). Electrode oximetry measurements enable us to carry out a detailed kinetic study and analysis of the iron oxidation reaction in apoferritin and site-directed mutants which has not been previously possible.

The results further delineate the role of the H and L subunits in the oxidation of Fe^{2+}. The experiments show that the ferroxidase activity of human liver ferritin originates from the catalytic active site on the H-subunit

and that the mutation of the putative nucleation site has little effect on the rate of Fe^{2+} oxidation. Recombinant L-chain ferritin is shown to have virtually no ferroxidase activity itself; however, the L-subunit significantly modulates the ferroxidase activity of the protein in mixed L-chain H-chain ferritins as evidenced by changes in the nature of the inhibition of the enzyme by Zn^{2+} and by alterations in the values of the Michaelis kinetic parameters, particularly K_{mO2} and k_{cat}. Mixed L-chain H-chain ferritins are more active than predicted based on their H-subunit composition alone.

MATERIALS AND METHODS

All chemicals were reagent grade and used without further purification unless otherwise indicated. Ferrous sulfate heptahydrate was obtained from J. T. Baker Chemical Co.; Mes and Mops were purchased from Research Organics Inc.; 2,2′-dipyridyl, thioglycolic acid (TGA) and sodium acetate were from Aldrich Chemical Company Inc.; and zinc sulfate heptahydrate was from Mallinckrodt Chemical Works. Recombinant L-chain and H-chain ferritins and H-chain variants were prepared by our collaborators in Italy as previously described (Levi et al., 1987; 1988; Lawson et al., 1989; Wade et al., 1991;) and rendered iron free by dialysis against 1 % thioglycolic acid in 0. 1 M sodium acetate, pH 5.5 for 24 h followed by dialysis against 0.1 M Mops, 0.1 M NaCl, pH 7 (Levi et al., 1988). Protein concentrations were determined by Bio-rad™ Coomassie brilliant blue G250 protein assay using bovine serum albumin as a standard. Sheep spleen ferritin was directly isolated from frozen sheep spleens following procedures as previously described (Arosio et al., 1978). The H and L subunits in sheep spleen ferritin was separated on 12% SDS-PAGE gel, and the H and L subunit composition were determined to be 64 % H and 34 % L by scanning of the Coomassie blue stained gel with a densitometer (Arosio et al., 1978).

Due to the very small percentage of H subunit in human liver ferritin, it was difficult to quantitate the H and L

subunit composition directly from the SDS-PAGE of human liver ferritin. An alternate method, therefore, was used to solve this problem. Samples containing (1) 5 % rHF + 95% HLF and (2) 10 % rHF + 90% HLF, rather than 100 % HLF, were introduced on a 17.5 % SDS-PAGE gel. Scanning of the Coomassie blue stained gel with a densitometer resolved 8.9 % H for sample (1) and 14.8 % H for sample (2) respectively. Thus, composition of about 4 % H and 96 % L in human liver ferritin was determined.

Kinetic measurements of iron(II) oxidation were performed with Fe/protein ratios < 50 where hydrogen peroxide is the main product of dioxygen reduction as given by equation 2.1 (Xu & Chasteen, 1991). A specially-designed sample cell containing an oxygen micro-electrode was used to measure the kinetics of O_2 consumption during Fe^{2+} oxidation (Chapter I). Iron(II) was added to the protein solution as freshly prepared 0.100 M $FeSO_4 \cdot 7H_2O$ in 0.05 M HCl. Reconstituted ferritin samples containing 1000 Fe per protein were prepared by gradually adding 20.8 μl of 0.100 M $FeSO_4.7H_2O$ to 1 ml of 20.8 μM apoferritin in 0.1 M NaCl, 100 mM Mops, pH 7.10 in air over a period of 2 minutes. Samples were then stirred for 1 hr followed by standing overnight at 4°C before introducing an additional amount of Fe^{2+} solution. Zn^{2+} inhibition studies were performed by adding microliter quantities of 0.100 M $ZnSO_4 \cdot 7H_2O$ to 1 ml of 20.8 μM apoprotein followed by incubation of the sample for 1 hr at ~20°C prior to the addition of Fe^{2+}.

RESULTS

The Stoichiometry of Iron Oxidation

Figure 2.1 shows the consumption of dissolved oxygen following addition of ferrous sulfate to buffer alone (curve a) and to six different apoferritins in buffer (curves b-g) using an Fe^{2+}/protein ratio of 32. From the total amount of oxygen consumed at completion of the reaction, the stoichiometry of iron(II) oxidation can be determined. The apparent stoichiometries obtained were $Fe^{2+}/O_2 = 2.1 \pm 0.1$ for rHF (curve g) and 2.7 ± 0.1 for HLF (curve e). The value of 2.1 for rHF implies that iron oxidation occurs according to the reaction 1 in agreement with previous results for horse spleen apoferritin (Xu & Chasteen, 1991). The higher value of 2.7 observed for HLF is a consequence of the relatively slow rate of Fe^{2+} oxidation observed with this protein (*c.f.* curves e & g) during which time some of the H_2O_2 originally produced in the iron(II) oxidation reaction disproportionates to O_2 and H_2O via reaction 2 (Chapter I). The disproportionation reaction results

$$2H_2O_2 \longrightarrow O_2 + 2H_2O \qquad (2.2)$$

in an artificially high value for the stoichiometry. Therefore the stoichiometry of 2.7 Fe^{2+} oxidized per O_2 consumed in HLF is an upper limit to the true value which is probably 2.0 as for HoSF and rHF (Table 2.1).

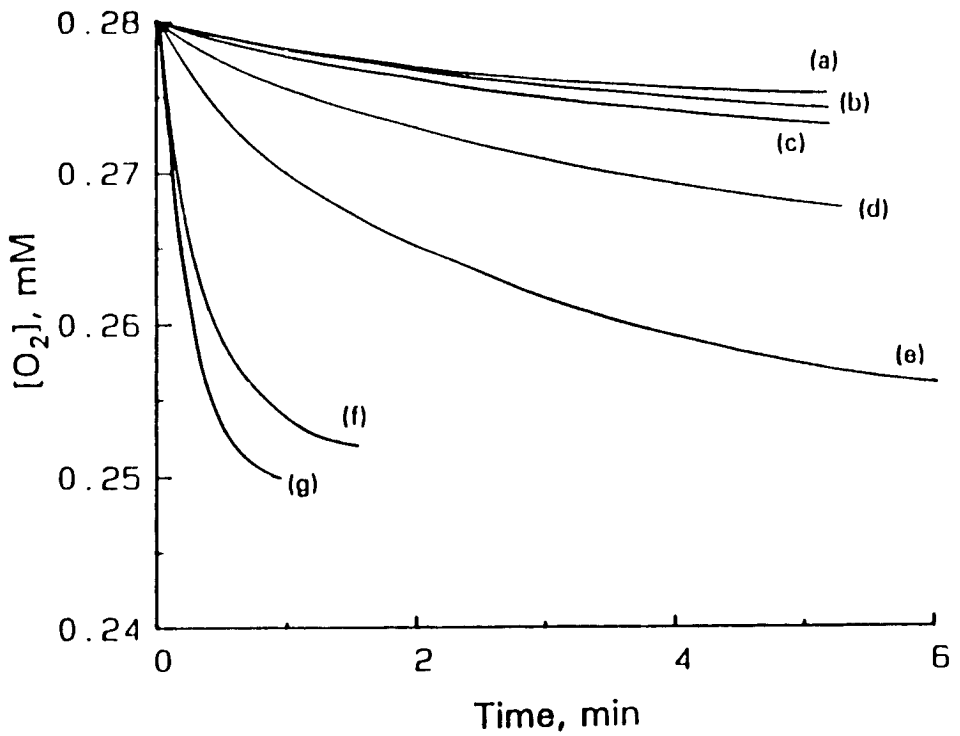

Figure 2.1. Oxygen consumption versus time for the oxidation of Fe^{2+} in (a) Buffer, (b) mutant S1 (D42A, E61A, E62K, E64A, H65G, E67A, K86Q), (c) rLF, (d) mutant 222 (E62K, H65G, K86Q), (e) HLF, (f) mutant A2 (E61A, E64A, E67A), and (g) rHF. Conditions: [apoferritin] = 2.08 μM, $[Fe^{2+}]_0$ = 67 μM, in 0.1 M NaCl, 50 mM Mops, pH 7.05, 20°C. File name: "92jy110 (a), 92jy114 (b), 92jy111 (c), 92jy112 (d), 92jy113 (e), 92de031 (f), 92jy115 (g)"

Ferroxidase Activity

Comparison of the curves in Figure 2.1 for buffer (curve a), and rHF (curve g) shows that the H-chain homopolymer greatly facilitates iron(II) oxidation whereas the L-chain homopolymer (rLF) (curve c) is virtually devoid of ferroxidase activity. Mutant 222 (E62K, H65G, K86Q) (curve d) in which the putative ferroxidase site ligands Glu-62 and His-65 have been mutated has lost much of its ability to facilitate Fe^{2+} oxidation, a result confirming the importance of one or both of these residues in ferroxidase activity. On the other hand, mutant A2 (E61A, E64A, E67A) which is depleted of the putative nucleation site ligands Glu-61, Glu-64, and Glu-67 is nearly as active as the recombinant H-chain protein (*c.f.* curves f and g), indicating that these ligands are not critical to iron(II) oxidation. Mutant S_1 in which both the putative ferroxidase and nucleation sites have been mutated is completely inactive (curve b). rLF (curve c) and mutant 222 (curve d), both lacking the ferroxidase site ligands Glu-62 and His-65, slightly accelerate the iron(II) oxidation compared to buffer and S_1, suggesting that the "nucleation site" may have weak ferroxidase activity. These findings for Fe^{2+} oxidation are consistent with previous observations of the relative rates of core formation and Fe^{2+} oxidation in these proteins (Levi, et al., 1988; 1989; Lawson et al., 1989; Wade et al., 1991). The initial rates of oxygen consumption for the human recombinant apoferritins and the

H-chain site-directed mutants are summarized in Table 2.1

To test the importance of a preexisting iron core in the iron(II) oxidation, samples of rHF and rLF were prepared containing 1000 Fe^{3+}/protein to which additional increments of Fe^{2+} were added, either 21 or 210 Fe^{2+}/protein. Figure 2.2 and its inset show the oxygen consumption profiles for both rHF (curve a) and rLF (curve b). When a large increment of additional Fe^{2+} is added (ΔFe^{2+}/protein = 210), iron(II) oxidation proceeded at similar rates for both rHF and rLF as shown in Figure 2.2. In contrast, when a small increment of Fe^{2+} is introduced (ΔFe^{2+}/protein = 21), the initial rate of oxygen consumption was about twice as large for rHF compared to rLF (0.028 *vs.* 0.015 mM/min) (Fig.2.2, inset). These data suggest that when a large increment of iron is introduced to either H-chain or L-chain homopolymers already containing a sizable iron core (1000 Fe/protein) the surface of the mineral core itself becomes important for Fe^{2+} oxidation.

The Cooperative Functions of H and L Subunits

To compare the catalytic activities of a number of ferritins containing different H and L compositions, the initial rates of oxygen consumption in rHF, rLF, SSF, HoSF, and buffer were measured as a function of the Fe^{2+} concentration (Fig. 2.3). The rate curve for rLF is similar to that of buffer alone, confirming that the L-subunit lacks a ferroxidase site (Lawson et al., 1989; 1991; Levi et al.,

TABLE 2.1

Initial Rate of Oxygen Consumption by Recombinant Human Apoferritins and Mutants.[1]

Protein	Initial Rate[2] (μM O_2/min)	Relative Rate
Buffer	1.36	2.0
S1	1.36	2.0
rLF	1.70	2.5
222	4.30	6.3
HLF	10.0	14.7
A2	54.0	79.4
rHF	68.0	100

[1]Conditions: as in Figure 2.1.

[2]Errors in rates are normally ± 5 %.

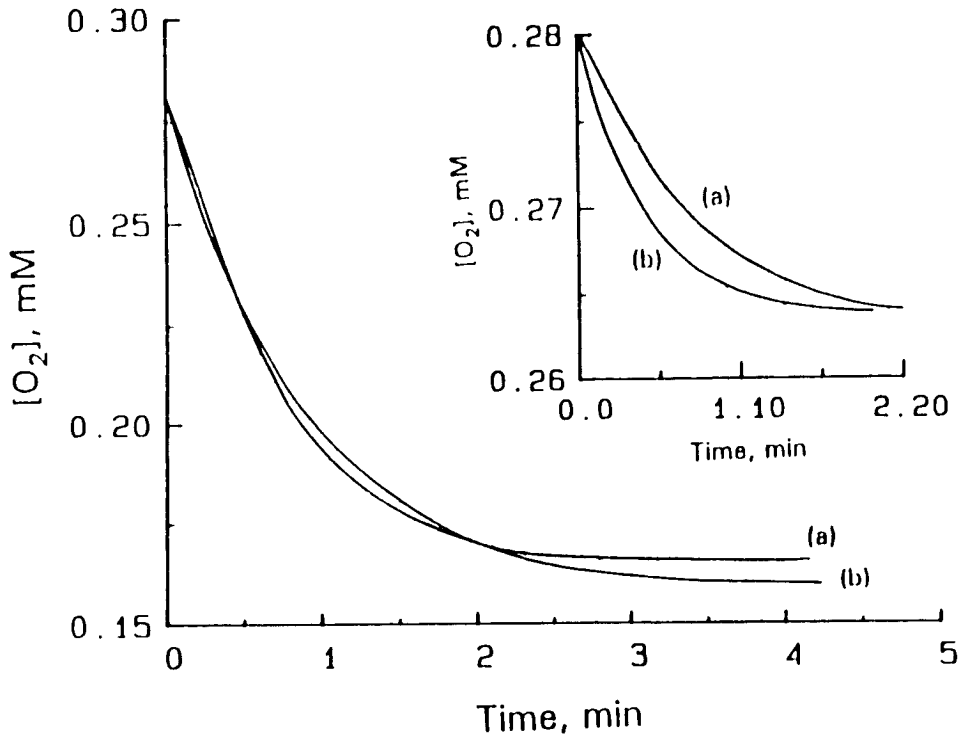

Figure 2.2. Oxygen consumption versus time for iron(II) oxidation in ferritins containing cores of 1000 Fe^{3+}. Increment of iron(II): ΔFe^{2+}/protein = 210 for Figure 2 and ΔFe^{2+}/protein = 21 for the inset. (a) rHF, (b) rLF. Conditions: [ferritin] = 2.08 μM, in 0.1 M NaCl, 100 mM Mops, pH 7.10, 20°C. File name: "92sep153 (a), 92sep154 (b), 92sep150 (inset, a), and 92sep151 (inset, b)"

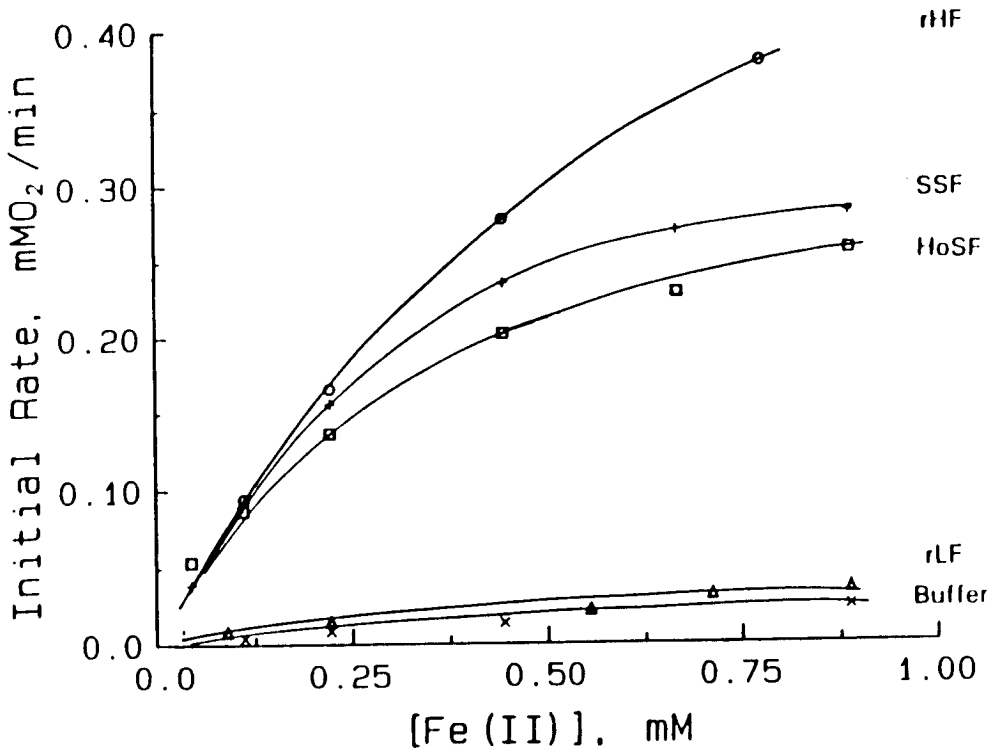

Figure 2.3. Iron saturation kinetics of various mammalian apoferritins. Conditions: [apoferritin] = 8.3 μM; $[O_2]_0$ = 0.28 mM, in 0.1 M NaCl, 50 mM Mops, pH 7 at 20 ^{0}C. File name: "Jan012 (rHF), Jan011 (SSF), Sep012 (HoSF), Dec091 (rLF), and Dec111 (buffer) "

1989) . In contrast, saturation kinetics with respect to iron(II) concentration is observed for rHF, SSF and HoSF as expected for an enzyme-catalyzed reaction where Fe^{2+} is a substrate. The rates of oxygen consumption for the various proteins increase with increasing H subunit composition, *i.e.*, rHF (100%) > SSF (66%) > HoSF (16%), as predicted since only the H-subunit possesses the ferroxidase site. However, when the rates at kinetic saturation are expressed on a H-chain basis, the order is reversed, namely, HoSF (1.6) > SSF (0.42) = rHF (0.42) where the number in parentheses is the rate of O_2 consumption in mM O_2/min. Therefore, in addition to the ferroxidase site on the H subunit, other factors are also contributing to the catalytic activity of apoferritins.

More direct evidence of the cooperativity of the H and L subunits comes from kinetic experiments performed on several specially assembled human apoferritins containing different amounts of H and L homopolymers (0 % - 100% of H-chain). Figure 2.4 illustrates the initial rate of oxygen consumption as a function of the percentage of H-subunit at Fe(II)/protein ratios of 35 and 350 respectively.
The rate dependence on H-chain percent is not linear in both instances. The observed activities are larger than what are expected based on the ferroxidase activity of the H subunit alone (Fig. 2.4, the dotted lines). The maximum enhancement in initial rate occurred at around 35 % of H-chain (Fig. 2.5). The initial rates on a per H subunit basis are listed against the percentage of L-subunit in the heteropolymer

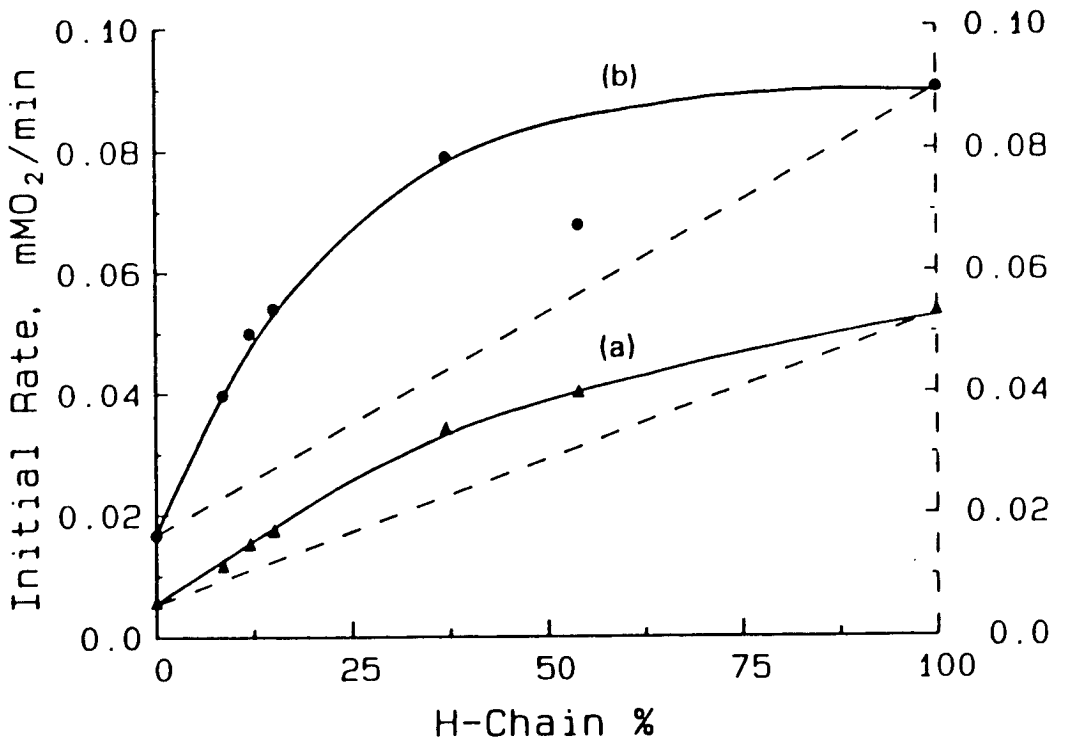

Figure 2.4. Initial rate of oxygen consumption versus H-chain % of the recombinant human liver apoferritin. Conditions: [apoferritin] = 1.9 μM; $[O_2]_0$ = 0.28 mM in 0.1 M NaCl, 50 mM Mops, pH 7.05 at 20 ^{0}C. Curve a: $[Fe^{2+}]_0$ = 0.066 mM; Curve b: $[Fe^{2+}]_0$ = 0.67 mM. File name: "93ma081 (a), and 93ma089 (b)"

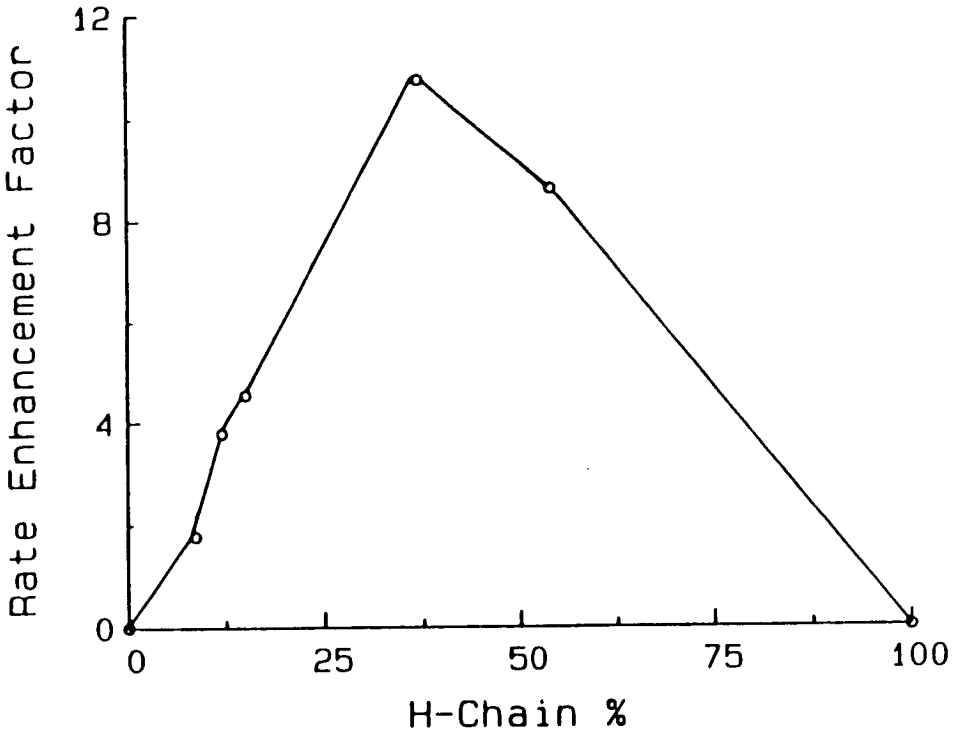

Figure 2.5. Rate enhancement factor versus H-chain % for recombinant HLF. Conditions: the same as curve a in Figure 2.4. File name: "93ma08a

mixtures in Table 2.2. It is clear that even though the L subunit lacks the ferroxidase site, its presence in ferritin somehow enhances the ferroxidase activity of the H subunit.

Enzyme Kinetics

In order to establish that rHF and HLF are true ferroxidases, measurements of the kinetics of oxygen consumption were carried out as a function of the concentrations of Fe^{2+}, O_2 and protein. Figure 2.6 and 2.7 show the dependence of the initial rate of iron oxidation on the concentration of Fe^{2+}. Saturation kinetics with respect to Fe^{2+} is observed with both rHF & HLF, consistent with an enzyme catalysis mechanism in which Fe^{2+} is a substrate. The insets of Figure 2.6 and Figure 2.7 illustrate the corresponding Lineweaver-Burk plots which are linear.

Figure 2.8 shows that saturation kinetics is also observed with respect to O_2 for rHF (upper panel), and HLF (lower panel). The rate was found to be first-order with respect to protein concentration for both HLF and rHF (Fig. 2.9). The kinetic parameters from least-squares fits of the Lineweaver-Burk plots in Figures 2.6, 2.7 and 2.8 are listed in Table 2.3 along with those previously determined for horse spleen apoferritin.

Zn^{2+} Inhibition

Zinc has long been known to be an inhibitor of core formation in horse spleen ferritin (Treffry et al., 1977)

TABLE 2.2

Initial Rate of Oxygen Consumption by the Recombinant Human Liver Ferritins Containing Different Amounts of H- and L-Subunit[1]

L-Chain %	V_0 X 10^3 per H-Chain[2] (mMO_2/min)
0	0.53
46	0.74
63	0.91
85	1.13
82	1.23
91.5	1.33

[1]Conditions: the same as Figure 2.4.

[2]Errors in rates are within ± 5 %.

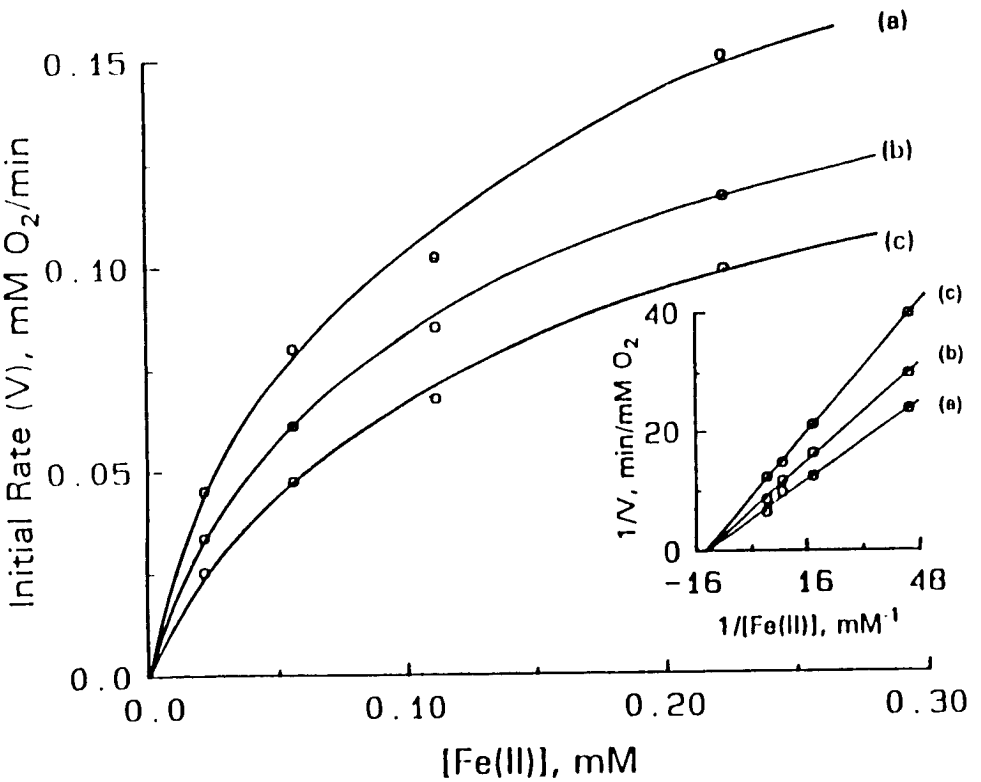

Figure 2.6. Initial rate of O_2 consumption as a function of iron(II) concentration in rHF at Zn^{2+}/Protein = 0 (a), 12 (b), and 24 (c). Inset: Lineweaver-Burk plots with the least-square straight lines. Conditions: [apoferritin] = 2.08 μM, $[O_2]_0$ = 0.28 mM, in 0.1 M NaCl, 50 mM Mops, pH 7.05, 20°C. File name: "Feb223 (a), Feb226 (b), Feb228 (c), feb224 (inset ,a), Feb227 (inset, b), and Feb229 (inset, c)"

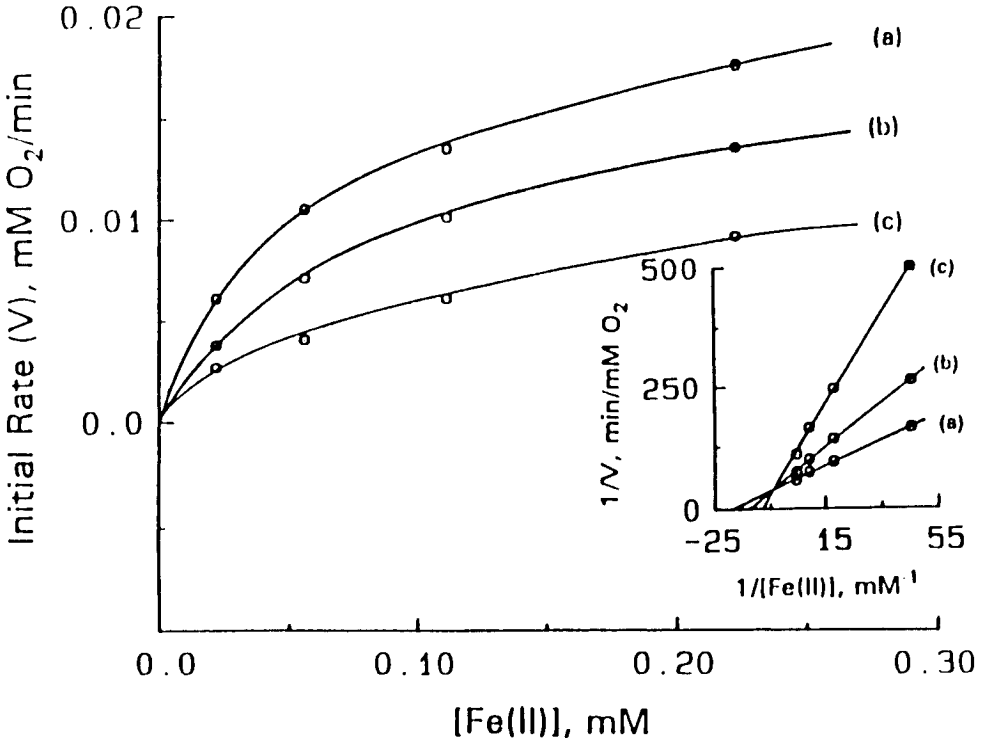

Figure 2.7. Initial rate of O_2 consumption as a function of Fe^{2+} concentration in HLF at Zn^{2+}+/protein = 0 (a), 6 (b), and 12 (c). Insets: The corresponding Lineweaver-Burk plots. Conditions are indicated in Figure 2.6. File name: "Feb221 (a), Feb235 (b), Feb233 (c), Feb122 (inset, a), Feb236 (inset, b), and Feb234 (inset, c)"

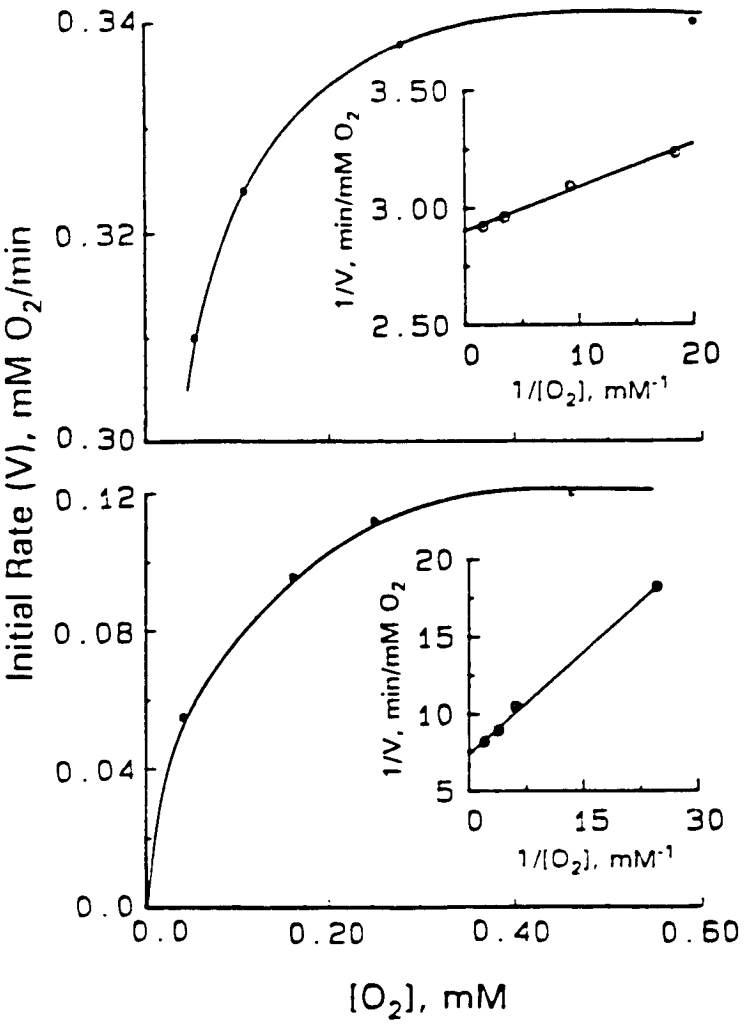

Figure 2.8. Rate of O_2 consumption as a function of O_2 concentration in rHF (upper panel) and in HLF (lower panel). Insets: The double reciprocal plots. Conditions: [apoferritin] = 10.4 μM, $[Fe^{2+}]_0$ = 44 μM, in 0.1 M NaCl, 50 mM Mops, pH 7.05, 20°C. File name: "92m181-182 (rHF) & 92j11-92j12 (HLF)"

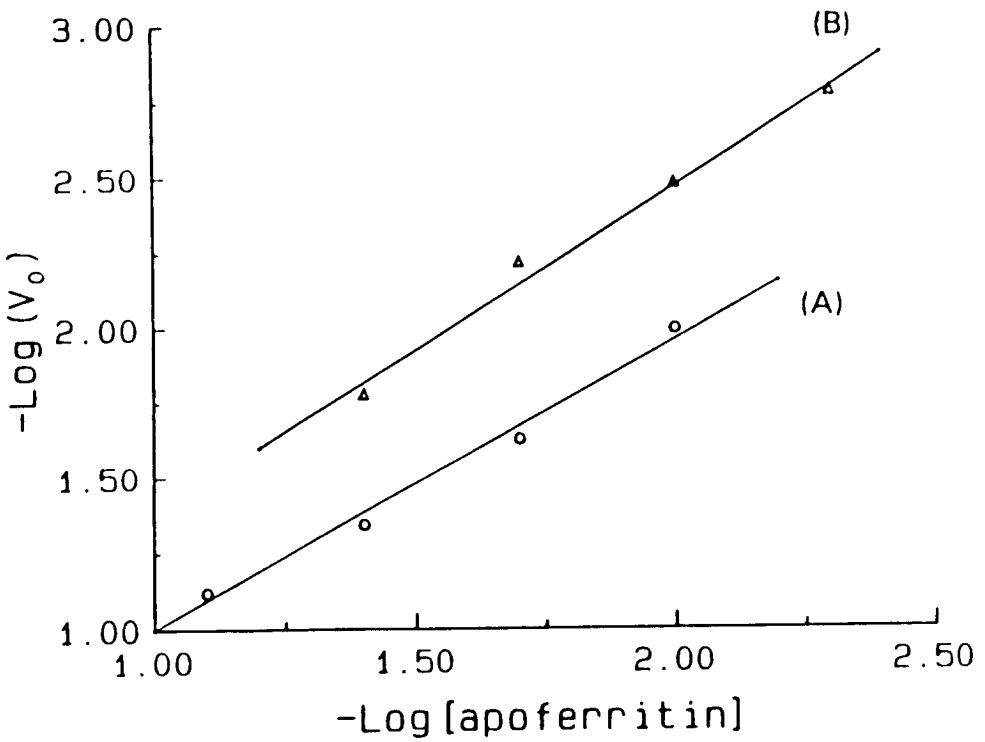

Figure 2.9. First-order plots with respect to apoferritin concentration. Conditions: $[Fe^{2+}]_0$ = 0.11 mM; $[O_2]_0$ = 0.28 mM in 0.1 M NaCl, 50 mM Mops, pH =7.05 at 20 ^{0}C. Curve a: rHF; curve b: HLF. File name: "92se161 (a) and 92se162 (b)"

and has been shown to be a noncompetitive inhibitor of iron(II) oxidation in horse spleen apoferritin at Zn^{2+}/protein ratios of ≤ 2 and a competitive inhibitor at ratios ≥ 6 (Chapter I). Zinc also inhibits iron uptake by the liver in animal studies (Matrone et al., 1975). To reveal how Zn^{2+} inhibits iron oxidation in rHF and HLF, oxygen uptake experiments were performed at various Zn^{2+}/protein ratios. The resultant Fe^{2+} saturation kinetics curves for rHF are shown in Figure 2.6 with the corresponding double reciprocal plots presented in the inset. Noncompetitive inhibition by Zn^{2+} is clearly observed in rHF as shown by the common intercept of the abscissa (Fig. 2.6, inset).

Two mechanisms have been previously proposed for the enzyme catalyzed oxidation of Fe^{2+} in apoferritin; one involves oxidation of a mononuclear Fe^{2+}-protein complex (Mechanism I) and the other the stepwise one-electron oxidation of a binuclear iron complex (Mechanism II) (Chapter I). The two mechanisms modified to take into account of zinc inhibition are given in Appendix I. As outlined there, either mechanism leads to equation 2.3 for noncompetitive inhibition of Fe^{2+} oxidation by Zn^{2+}, *viz.*

$$1/V = (2/P_0K_1K_2)\left\{\frac{(1+[Zn^{2+}]/K_1)}{\alpha[Fe^{2+}]} + \frac{(1+[Zn^{2+}]/K_1)(1+K_2[O_2])K_1}{\alpha}\right\} \quad (2.3)$$

where $\alpha = (k_3 + k_3'[Zn^{2+}]/K_1)[O_2]$, $K_1 = k_1/k_{-1}$, $K_2 = k_2/k_{-2}$.

Here K_I is the inhibitor dissociation constant and the other k's correspond to rate constants for the individual steps in the mechanism (Appendix I). P_0 is the protein concentration. Thus from equation 2.3, plots of 1/V versus $1/[Fe^{2+}]$ at various fixed Zn^{2+} concentrations are expected to intercept the abscissa at the same point, $-1/K_{m,Fe}$, as is observed (Fig. 2.6, inset). Since the rate of Fe^{2+} oxidation is much faster in the absence of inhibitor, *i.e.* $k_3 >> k_3'$, K_I can be obtained by plotting 1/V versus $[Zn^{2+}]$ at various fixed Fe^{2+} concentrations (Fig. 2.10). The intercept of the abscissa is equal to $-K_I$. A value of K_I = 74 ± 10 μM is obtained (Table 2.3). Figure 2.11 shows the effect of added Zn^{2+} on the initial rate of oxygen consumption in rHF. The presence of 2 Zn^{2+} per rHF subunit reduces the initial rate by 50 %, while in horse spleen ferritin only 0.5 Zn^{2+}/subunit are needed to do the same (Fig. 1.14 in Chapter I).

In contrast to rHF, HLF shows mixed inhibition by Zn^{2+} (Fig. 2.7, inset). Both the slope and intercept vary with Zn^{2+} concentration, but the lines intercept at a common point, namely $1/[Fe^{2+}] \approx -4$ mM^{-1} and $1/V \approx 40$ min mM^{-1}. Unlike the noncompetitive inhibition mechanism in which the presence of inhibitor does not affect the binding of substrate, in the mixed-inhibition mechanism the enzyme and the enzyme-inhibitor complex bind substrates with different affinity (Roberts, 1977). The following Lineweaver-Burk equation is obtained for the mixed-inhibition mechanism

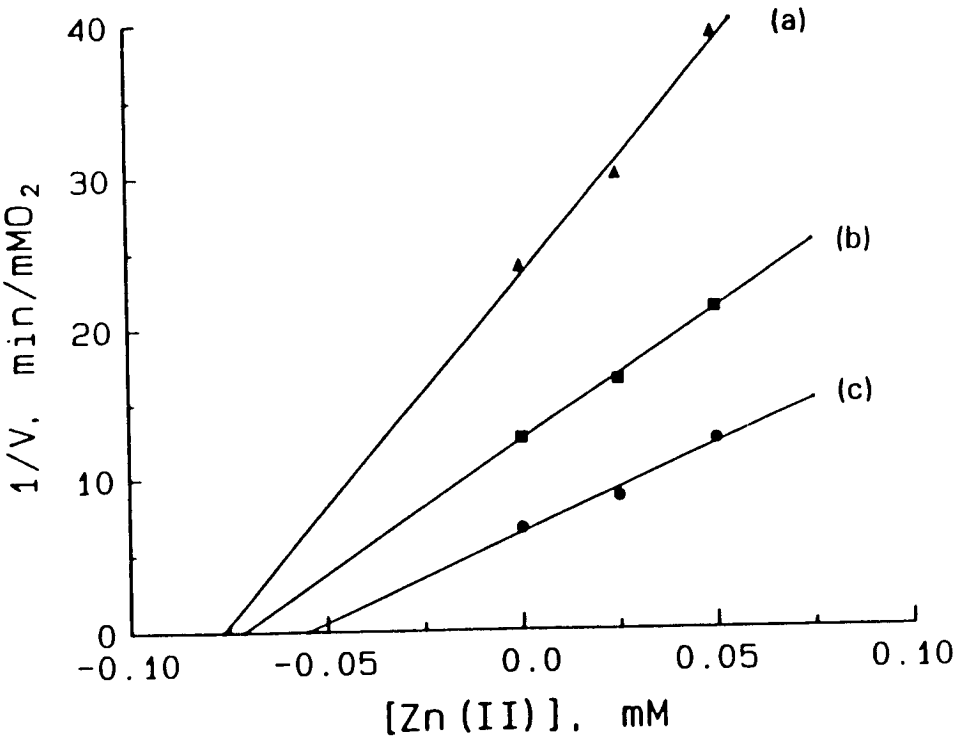

Figure 2.10. Plots of $1/V_0$ versus $[Zn^{2+}]_0$ at various Fe^{2+} concentrations in rHF. Conditions: as described in Figure 2.6, where $[Fe^{2+}]_0$ = 0.022 mM (a), 0.056 mM (b), and 0.222 mM (c). File name: "92oct304 (a), 92oct303 (b), and 92oct301 (c)"

TABLE 2.3

Kinetic Parameters for rHF[a], HLF[a] and HoSF[b]

	rHF	HLF	HoSF
$K_{m,O2}$ (μM)	6 ± 2	60 ± 12	140 ± 30
$K_{m,Fe}$ (μM)	80 ± 10	50 ± 10	350 ± 10
k_{cat} (min^{-1})	201 ± 14	31.2 ± 0.6	80.0 ± 3.3
$K_{I,Zn}$ (μM)	74 ± 10	-----	67 ± 11[c],
Fe^{2+}/O_2	2.1 ± 0.1	< 2.7 ± 0.1	2.0 ± 0.2[d]
E_a (kJ/mol)	26.4 ± 0.1	67.3 ± 0.5	36.6 ± 1.3
$\Delta H^{\ddagger}$ (kJ/mol)	23.9 ± 0.1	64.8 ± 0.5	34.2 ± 1.3
$\Delta S^{\ddagger}$ (J/mol-K)	-136.0 ± 0.4	-11.0 ± 1.6	-108 ± 5

[a]Conditions: 0.1 M NaCl, 50 mM Mops,pH 7.05, 20°C. The kinetic parameters listed for rHF and HLF were obtained from the data plotted in Figures 2.6 - 2.8 and 2.12.

[b]HoSF, horse spleen apoferritin composed of 16% H and 84% L subunits. The data listed for HoSF are from Chapter I.

[c]K_I for competitive inhibition at Zn^{2+}/protein ratios ≥ 6.

[d]From Xu and Chasteen, 1991.

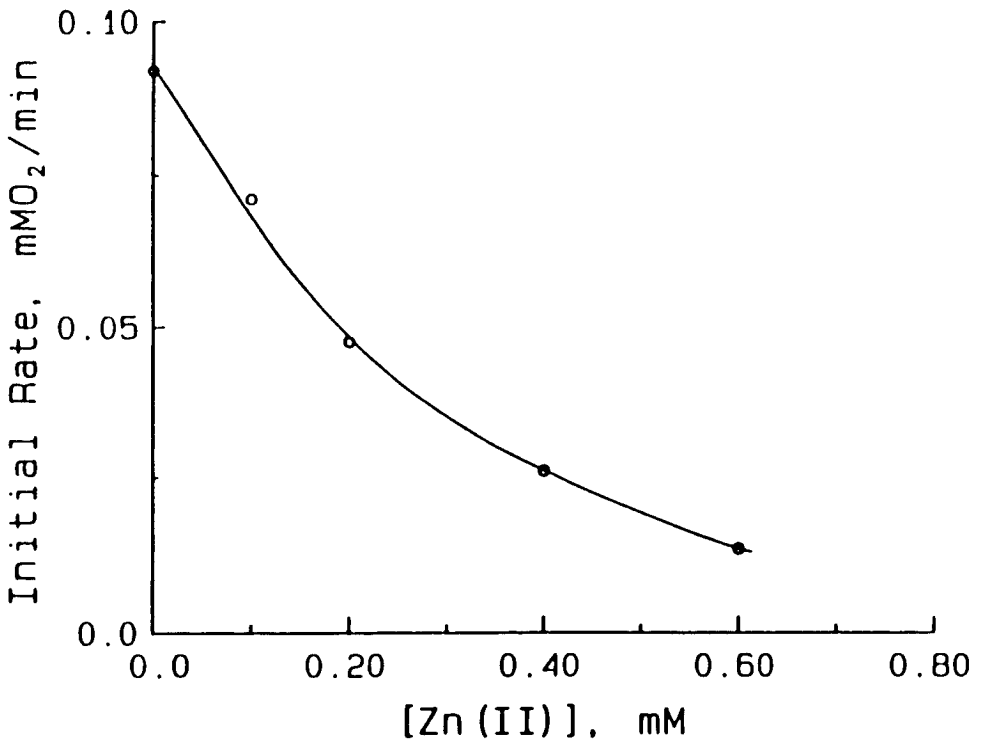

Figure 2.11. Inhibition of iron(II) oxidation by Zn(II) at a fixed iron(II) concentration in rHF. Conditions: [rHF] = 4.2 μM; $[Fe^{2+}]_0$ = 0.11 mM, $[O_2]_0$ = 0.28 mM in 0.1 M NaCl, 50 mM Mops, pH 7.05 at 20 ^{0}C. File name: "92ja02"

(Appendix I).

$$1/V = 2/P_0[O_2].\{\frac{1+[Zn^{2+}]/K_I}{(A+B[Zn^{2+}]/K_I)[Fe^{2+}]} + \frac{C+D[Zn^{2+}]/K_I}{A+B[Zn^{2+}]/K_I}\} \quad (2.4)$$

where $A = k_3K_1K_2$, $B = k_3'K_1'K_2'$, $C = K_1(1 + K_2[O_2])$, $D = (1 + K_2'[O_2])K_1'$. The intersection of Lineweaver-Burk plots at different Zn^{2+} concentrations occurs at a common point as shown in Figure 2.7 (inset) and is given by $1/[Fe^{2+}] = (BC-DA)/(A/K_I-B)$ and $1/V = \{(1+1/K_I)/(A+B)\}\{(B-DA)/(A/K_I - B)\}+(C+D)/(A+B)$. Because the slope and intercept depend on several rate and equilibrium constants, it is not possible to independently determine a value for the inhibitor constant K_I for mixed-inhibition.

Temperature and pH Dependence

The Arrhenius plot of the temperature dependence of the rate constant k_1 for Fe^{2+} binding to the ferroxidase site is shown in Figure 2.12. The value of k_1 was obtained from the equation $V = k_1[Fe^{2+}][P_0]$ under conditions of pseudo second-order kinetics where the observed initial rate V is saturated with respect to O_2 concentration and undersaturated with respect to Fe^{2+} concentration. The activation energies E_a and the entropies $\Delta S^{\ddagger}$ and enthalpies $\Delta H^{\ddagger}$ of activation for rHF and HLF are summarized in Table 2.3.

The pH dependence of the initial rate of iron oxidation

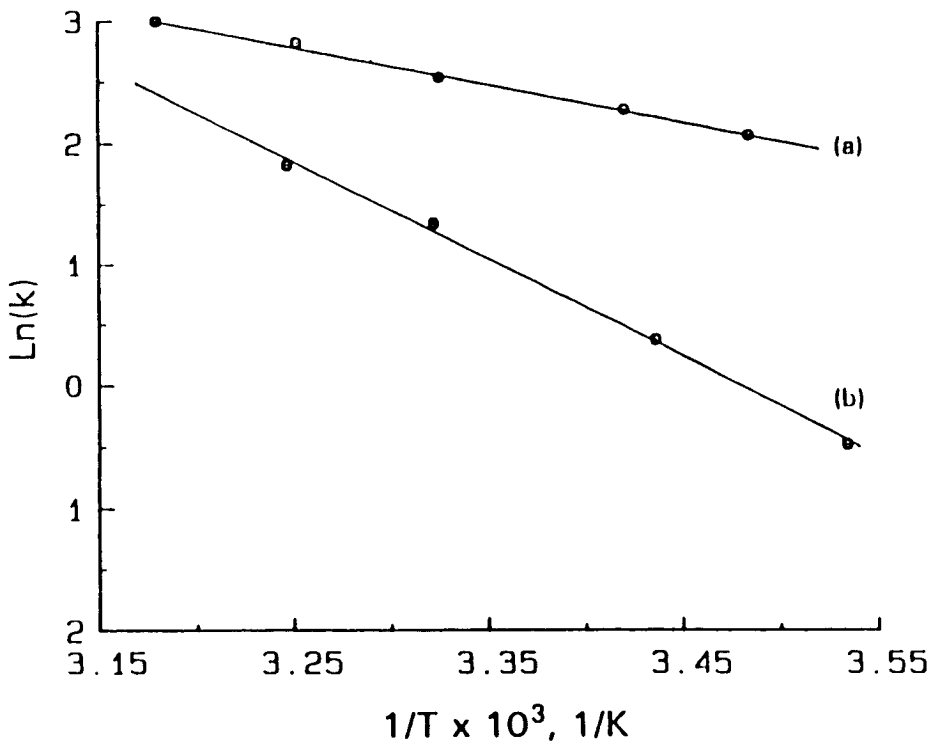

Figure 2.12. Arrhenius plot for k_1 in rHF (a) and HLF (b). Conditions: [apoferritin] = 4.2 μM, $[Fe^{2+}]_0$ = 110 μM, in 0.1 M NaCl, 50 mM Mops, pH 7.05. File name: "92my21 (a) and 92jy220 (b)"

is illustrated in Figure 2.13. A bell-shaped pH profile is observed for the oxidation reaction in rHF with a maximum rate at pH ≈ 7.0 (Fig. 2.13, curve a). Deprotonation of the ferroxidase site ligand His-65 is probably responsible for the observed curve as previously discussed for HoSF (Chapter I). Similar curves are commonly encountered in the O_2 oxidation of small Fe^{2+} chelates (*e. g.*, Kuramura et al., 1968). In contrast, with HLF the initial rate of O_2 consumption increases with increasing pH (Fig. 2.13, curve b), probably due to the low activity of the protein which is obscured by the high rate of iron(II) autoxidation at pH > 7.0. The apparent stoichiometry of Fe^{2+} oxidation increases from 2.7 Fe^{2+}/O_2 at pH 7 to 3.6 at pH 8.9, close to the limiting value of 4.0 for Fe^{2+} autoxidation (equation 2.5).

$$4Fe^{2+} + O_2 + 6H_2O \rightleftarrows 4FeOOH + 8H^+ \qquad (2.5)$$

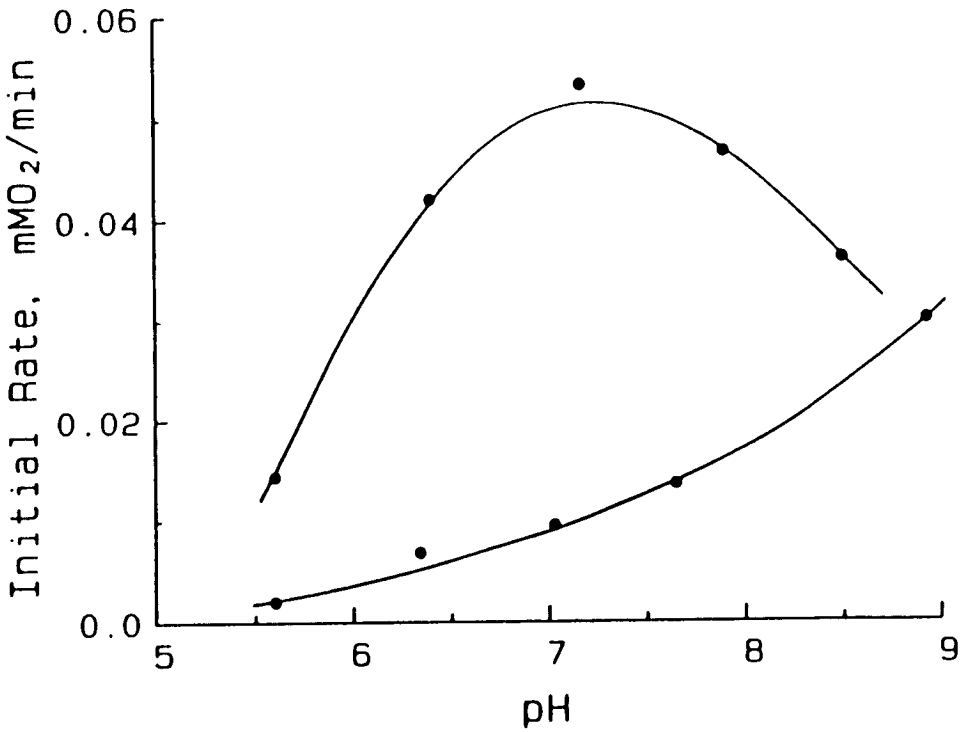

Figure 2.13. pH dependence of the initial rate of O_2 incorporation in rHF (a) and in HLF (b). Conditions: [apoferritin] = 2.08 μM, $[Fe^{2+}]_0$ = 67 μM , in 0.1 M NaCl, 25 mM Mes, 25 mM Mops, 20°C. File name: "92my22 (a) and 92jy240 (b)"

DISCUSSION

Comparison of ferroxidase activity of the six different apoferritins (Fig. 2.1) confirms that the ferroxidase site in human apoferritins is located solely on the H-subunit. A major binding site for Fe^{2+} on the L-subunit of the horse spleen protein has been identified by VO^{2+} EPR and ENDOR spectroscopy (Hanna et al., 1991) which in light of the present data is unlikely to be a ferroxidase site although it may be the initial site of Fe^{2+} binding to the protein prior to migration to the ferroxidase site.

Alteration in the postulated ferroxidase center ligands Glu-62 and His-65 (Lawson et al., 1989) does not completely eliminate the Fe^{2+} oxidation (Fig. 2.1, curve d). Only when both the putative ferroxidase site (Glu-62 and His-65) and nucleation site (Glu-61, Glu-64 and Glu-67) ligands are mutated does the protein fail to catalyze the oxidation of iron (Fig. 2.1, curve b). These results are consistent with the previous observation that rLF, although lacking the putative ferroxidase center, is still capable of slowly accumulating iron (Levi et al., 1989; Wade et al., 1991). Mutation of the three inner surface glutamate residues, Glu-61,64,67, of the putative nucleation site in variant A2 causes only a slight decrease in the rate of Fe^{2+} oxidation (32 Fe^{2+}/apoprotein) (Fig. 2.1, curve f), implying that these residues have only a minor role in iron(II) oxidation under conditions of low increments of iron(II) in agreement

with recent Mössbauer data (Bauminger et al., 1991). This result contrasts with that obtained when 1000 Fe's are added to the apoprotein where the rate of core formation in mutant A2 was significantly lowered (Lawson et al., 1991), an observation consistent with the postulated role for residues Glu-61,64,67 in core nucleation or iron(II) oxidation at high iron loading of the protein.

The kinetic results obtained here with human liver ferritin are in accord with previous findings on horse spleen ferritin, confirming that apoferritins generally function as ferroxidases during iron uptake. The first-order kinetics with respect to Fe^{2+} concentration below levels of kinetic saturation in both rHF and HLF provide strong evidence for a mechanism involving a one-electron transfer step during iron(II) oxidation. The μ-oxo-bridged Fe^{3+} dimers found immediately following Fe^{2+} oxidation in horse spleen ferritin (Bauminger et al., 1989) and in rHF (Bauminger et al., 1991; Treffry et al., 1992) probably are the result of iron(II) oxidation taking place in two one-electron steps by a mechanism similar to Mechanism II given in the Appendix I. The ligands of the iron dimer complex may be the same as those of the A and B sites of the Tb^{3+} dimer located at the ferroxidase center of rHF by x-ray crystallography (see Introduction). Moreover, the failure of spin trapping experiments to detect the formation of free superoxide, $O_2\cdot^-$ (Grady et al., 1989; 1991), can be accounted for by Mechanism II since the $O_2\cdot^-$ produced upon oxidation of

the first Fe^{2+} remains bound, forming a Fe^{3+}-O_2^- protein complex. Thus, Mechanism II is in better accord with all available kinetic and spectroscopic data than Mechanism I.

The k_{cat} values for the various ferritins follow the order rHF (201) > HoSF (80) > HLF (31 min^{-1}) as expected based on their H-subunit content (Table 2.3). On average the 24 mers of rHF, HoSF and HLF contain 24, 3.8 and 1.0 H-subunits, respectively. However when k_{cat} is expressed on a per H-subunit basis, the order of activity is reversed, *i.e.* rHF (8.4) < HoSF (21) < HLF (31 $min^{-1}subunit^{-1}$). A similar phenomenon has been observed when comparing the catalytic activities of rHF, SSF, and HoSF (see Results).

It is evident that the ferroxidase activity per H-subunit is substantially greater in the heteropolymer proteins relative to the H-chain homopolymer and appears to increase with increasing L-subunit composition. While these kinetic behaviors may be related in part to differences of those apoferritin species, the experimental results with the H and L homopolymer mixtures of human liver apoferritin, which are summarized in Table 2.2, demonstrate that the most efficient ferroxidase sites at oxidizing iron are those where appreciable amounts of L-chains exist. Either some of the ferroxidase sites of H-homopolymer rHF do not catalytically process the Fe^{2+} substrate and therefore do not contribute to the observed reaction rate, or the presence of L-subunits in HLF and HoSF significantly enhances the catalytic activity of the ferroxidase sites

that are on the H-subunits. Recent studies have shown that the L-ferritin is more efficient than H-ferritin in inducing iron mineralization possibly because it contains a higher density of negative charges in the cavity (Levi et al., 1992). Thus it is conceivable that the large ratio of nucleation to ferroxidase sites and the high nucleation efficiency of L-chains in heterpolymer proteins could enhance the turnover of Fe^{3+} produced at the ferroxidase sites, leading to the greater value of k_{cat} on a per H-subunit basis than we observed here for L-subunit rich ferritins. This finding suggests that the two chains cooperate in the mechanism of ferritin iron uptake, probably acting on different steps of the reaction pathway.

When a relatively large increment of iron(II) (≈210) is added to ferritin already containing 1000 Fe/protein, the rate of iron(II) oxidation is essentially the same for both rHF or rLF (Fig. 2.2) even though the latter lacks a ferroxidase site (Levi et al., 1988). Under these conditions, iron(II) oxidation evidently occurs primarily on the surface of the mineral core in accord with the crystal-growth model for core formation (Macara et al., 1972, 1973). However, when a small increment of iron(II) is introduced to the protein (21 Fe^{2+}/protein) containing 1000 Fe^{3+}/protein, the initial rate of iron(II) oxidation is faster in rHF than in rLF (Fig. 2.2, inset), presumably in this instance because of involvement of the protein ferroxidase site in Fe^{2+} oxidation in rHF. In light of the present observations

and those obtained previously with HoSF (Chapter I), there are clearly at least two pathways for iron(II) oxidation in ferritin, the crystal-growth pathway (Macara et al., 1972, 1972) involving the mineral surface and the enzyme-catalysis pathway originally proposed by Crichton and Roman (1978). Oxidation of iron(II) occurs simultaneously by both pathways but each predominates under different circumstances depending on the size of the ferritin mineral core, protein subunit composition, pH and the amount of iron(II) introduced to the protein. Thus small increments of iron(II) loading favor the protein catalysis pathway but when this pathway becomes kinetically saturated at higher increments of iron(II), the observed rate of the reaction then largely reflects the crystal growth pathway.

Zinc inhibition of ferroxidase activity of the ferritins is complex. It is noncompetitive for rHF (Fig. 2.6) and for HoSF at low Zn^{2+}/protein ratios ≤ 2 but becomes competitive at ratios ≥ 6 (Chapter I). Mixed inhibition is observed in HLF at ratios ≤ 12 (Fig. 2.7) and competitive inhibition at ratios > 24 (data not shown). Four kinds of Zn^{2+} binding sites have been located inside the cavity and in the 3-fold channels of the L-chain of horse spleen ferritin by x-ray crystallography (Harrison et al., 1986), but the number and location of Zn^{2+} binding sites on H-chain ferritin are unknown. The less efficient Zn^{2+} inhibition in rHF compared to horse spleen ferritin (see Results) implies that there are other higher affinity Zn^{2+} binding sites on rHF in

addition to the ferroxidase sites.

The recent proposal that Zn^{2+} inhibition at a high Zn^{2+}/protein ratio of 240:1 in horse and sheep spleen apoferritin occurs from Zn^{2+} binding in the 3-fold channels (Yablonski & Theil, 1992) is at variance with recent site-directed mutagenesis studies of rHF showing that Zn^{2+} inhibition is retained when the 3-fold channels are mutated (Treffry et al., 1993). UV-difference spectroscopic studies of the Zn^{2+} inhibition of Fe^{3+} binding to horse spleen ferritin suggest the presence of a high affinity Zn^{2+} binding site which is not involved in Fe^{2+} oxidation (Treffry & Harrison, 1984). It is possible that some of the observed noncompetitive inhibition may involve Zn^{2+} binding to nucleation sites for Fe^{3+} core formation, thus lowering the rate of turnover of Fe^{2+} to Fe^{3+}, or to sites involved in iron migration. However, since the rate of Fe^{2+} oxidation in mutant A2, which lacks the putative "C" nucleation site ligands Glu-61,64,67, is nearly the same as that of the wild type, our data indicate this site is unlikely a key binding site for Zinc inhibition. Recent Mössbauer kinetic data indicating that this site is not important for cluster formation at levels of iron loading similar to those employed here is consistent with this view (Bauminger et al., 1992). Thus the observed noncompetitive inhibition in rHF and HoSF and the mixed inhibition in HLF appear to involve zinc binding sites yet to be identified. Zinc binding to the L-chain nucleation site could be

involved in inhibition of the heterpolymers as well. Since Zn^{2+} inhibition gradually becomes competitive at higher ratios in both HLF and HoSF, it is evident that Zn^{2+} at sufficiently high concentration ultimately can compete directly with Fe^{2+} for binding at the H-chain ferroxidase sites in these proteins.

The K_I (= 74 μM) for noncompetitive inhibition in rHF is very similar to the value of 67 μM (Zn^{2+}/protein $\geq$ 6) for competitive inhibition in HoSF (Table 2.3). The similarity in inhibition constants suggest similar ligands for Zn^{2+} in both instances. The formation constant ($1/K_I \sim 10^4\ M^{-1}$) for the Zn^{2+}-protein complex is typical of the values commonly observed for small chelates having two to three coordinating carboxylate groups (Martell & Smith, 1977), a result consistent with the makeup of crystallographically identified Zn^{2+} sites of HoSF which involve aspartate and glutamate residues (Harrison et al., 1986).

The observed dioxygen saturation kinetics (Fig. 2.8) shows that kinetic saturation is achieved at lower concentrations of O_2 in rHF compared with HLF, indicative of an apparent tighter oxygen binding to Fe^{2+}-rHF than to Fe^{2+}-HLF. The K_{mO2} for rHF is about 10 times smaller than that of HLF (Table 2.3) and suggests that the L-subunit modulates the affinity of the Fe^{2+}-protein complex for O_2 in the heteropolymer.

The small activation energy (E_a = 26 kJ) for k_1, the rate constant for Fe^{2+} binding to the ferroxidase site in

rHF, is consistent with the high ferroxidase activity of the protein compared to HLF. The large negative entropy of activation ($\Delta S^{\ddagger}$ = -136 J/mol-K) in rHF suggests substantial changes in the protein ligand conformation upon Fe^{2+} binding, whereas the small activation entropy, $\Delta S^{\ddagger}$ = -11 J/mol-k, in HLF is comparable to that observed upon complexation of Fe^{2+} by small chelates (Hewkin & Prince, 1970). These findings provide further evidence for the involvement of the L-subunit in modulating iron(II) oxidation in the heteropolymer. Moreover, the small negative activation entropy of HLF may account for the higher than expected reactivity of this protein based on its H-subunit composition alone.

In summary, the present data have provided further insight into the kinetic properties of the ferritins. The data demonstrate that catalytic activity is centered on the H-subunit but is clearly modulated by the presence of the L-subunit. The iron(II) oxidation kinetics of the mutants are in general accord with the rates of core formation determined in previous studies with these proteins (Levi et al., 1989; Wade et al., 1991). The kinetics observed here for both rHF and HLF is most consistent with a mechanism based on formation of a dimeric iron species at the ferroxidase center, where iron(II) oxidation occurs via two one-electron transfer steps involving a single dioxygen molecule as in Mechanism II.

CHAPTER III

INVESTIGATION OF THE EPR-ACTIVE SPECIES GENERATED DURING IRON OXIDATION IN HORSE SPLEEN APOFERRITIN

Introduction

The basic process of iron uptake and deposition in ferritin can be described as follows: (1) Fe^{2+} first binds to the outer surface of the protein shell; (2) the Fe^{2+} then migrates to the ferroxidase sites which are located on the inner surface of the H-chain where it is oxidized at these sites; (3) the resulting Fe^{3+} moves to the nucleation sites inside the cavity; (4) Fe^{3+} cluster formation then occurs. Recently, the Fe^{2+} binding site or sites have been located in the 3-fold channel near the exterior surface of the protein shell with Cys-130, His-118 and or His-128 as possible ligands (Lee et al., 1993). Ligands of the ferroxidase site as well as the putative nucleation site have been identified with site-directed mutagenesis in the interior of the H-subunit of Human liver ferritin (Lawson et al., 1989). However, details of how Fe^{2+} transfers from the outer protein surface to the ferroxidase sites, as well as how Fe^{3+} migrates from the ferroxidase sites to the nucleation sites situated in the inner surface of the protein shell are unclear.

To better understand the molecular mechanism of iron uptake by horse spleen ferritin a variety of techniques, including UV-Vis, EPR and Mössbauer spectroscopies, have been employed. Several intermediate species have been observed by Mössbauer spectroscopy, including an Fe^{3+}-protein complex, an Fe^{3+}-Fe^{3+} dimer, and various-sized Fe^{3+} clusters during the initial stages of ferritin formation (Bauminger et al., 1989; Jacobs., 1989). EPR spectroscopy reveals three signals of different g values upon iron(II) oxidation in ferritin under aerobic conditions. The signal at g′ = 4.3 has been ascribed to be a monomeric Fe^{3+}-protein complex (Chasteen & Theil, 1982; Rosenberg & Chasteen, 1982), while the other two signals at g′ = 1.87 and g = 2.00 have been assigned to a dimeric Fe^{2+}-Fe^{3+} mixed-valence species and an organic free radical signal respectively (Chasteen et al., 1985; Hanna et al., 1991; Grady et al., 1989). The mixed-valence signal is seen only in the presence of excess amounts of Fe^{2+}.

Inhibition studies using Zn^{2+} and Tb^{3+} on the formation of the intermediate species have been used to probe the location and binding sites of individual species observed during iron oxidative deposition in ferritin (Hanna et al., 1991; Rosenberg & Chasteen, 1985). X-ray crystallographic studies of metal ion binding to ferritin have resolved the Zn^{2+} and Tb^{3+} binding sites on horse spleen ferritin (Harrison et al., 1985; 1986). The Zn^{2+} binding sites are in the hydrophilic channels along the 3-fold axes as well as

on the exterior and interior surfaces of the protein, while the Tb^{3+} binding sites are located inside the 3-fold channel and the 2-fold groove as well as inside on the B-helix.

In previous EPR measurements, experiments were performed at reaction times of a few minutes to several hours. The reaction time is the time between the introduction of Fe^{2+} into the oxygenated apoferritin sample and the time the sample is frozen for EPR measurement. Short-lived intermediate species formed at the very early stages of ferritin formation might have already decayed away in these relatively long time intervals. Therefore, in the present work, kinetic studies of the EPR-active species were achieved by combining the rapid-mixing, freeze-quench technique with EPR spectroscopy, employing a reaction time scale of milliseconds to minutes. In this way, EPR-active species can be detected at the very onset of iron oxidation. The three paramagnetic species generated during the very early stages of iron deposition in the apoferritin shell have been partially characterized. Moreover, an additional radical signal with axial symmetry has been observed and the nature of this radical has been speculated upon.

Materials and Methods

Materials

Horse spleen ferritin, bovine liver catalase (EC 1.11.1.6), bovine erythrocyte superoxide dismutase (EC 1.15.1.1), and *Aspergillus niger* glucose oxidase (EC 1.1.3.4) were purchased from Boehringer Mannheim; Mops was from Research Organics Inc.; α-D(+) glucose and N-(2-hydroxyethyl)piperazine-N′-3-propane sulfonic acid (EPPS) were purchased from Sigma Chemical Co.; ferrous sulfate heptahydrate and sodium bicarbonate were obtained from J. T. Baker Co.; zinc sulfate heptahydrate was from Mallinckrodt Chemical Works. Terbium(III) chloride hexahydrate and sodium periodate were from Aldrich. A 0.1 M stock solution of KO_2 was prepared in dimethyl sulfoxide (DMSO) containing 0.1 M d-18-crown-6 ether. Apoferritin was prepared by dialysis against 1% TGA and 0.15 M NaCl as described previously. The concentration of the apoferritin was measured on a Cary 219 spectrophotometer from the absorbance at 280 nm and was expressed in subunit throughout the text. The stock solution of apoferritin was stored in 0.05 M Mops at 4^0C.

Freeze-Quench Experiments

Rapid-mixing Apparatus: All fast-mixing experiments were performed at room temperature (22-23 ^{0}C) on a System 1000 chemical/freeze-quench apparatus manufactured by Update Instrument Inc. The temperature of the isopentane,

monitored with a Copper-constant thermocouple, was maintained at -130 ± 5 ^{0}C. The schematic experimental setup, including a syringe ram (a), a ram controller (b), and a freezing tank (c) is shown in Figure 3.1.

Freeze-quenching Procedures: In a typical experiment, two syringes of 2.0 ml and 0.5 ml volumes were used. Samples with a total volume of around 300 μl from the two syringes were pushed through a reactor hose and the spray nozzle at a velocity of 2 cm/s into the liquid isopentane contained in a quartz or plastic funnel to which a 5 inch long quartz EPR tube was attached with 0.125" X 0.0625" (outer and inner diameters) rubber tubing. The small crystals formed in the isopentane reservoir were promptly packed into the EPR tube within a minute. The EPR tube containing the acquired sample was then disconnected from the funnel and stored in a dry-ice acetone slush at -77 ^{0}C, and the isopentane inside the EPR tube was pumped away using a mechanical vacuum pump and a liquid N_2 trap. Subsequently, a 5" piece of open ended quartz tubing was attached to the EPR tube using a piece of heat-shrink tubing. Samples were then stored at -126 ^{0}C for later EPR measurements. The detailed experimental procedures are described in Appendix II.

Determination of the Instrument Dead Time: The dead time of the instrument was determined using the standard reaction of metmyoglobin with sodium azide as previously described (Brenner et al., 1989; Ballou & Palmer, 1974). A

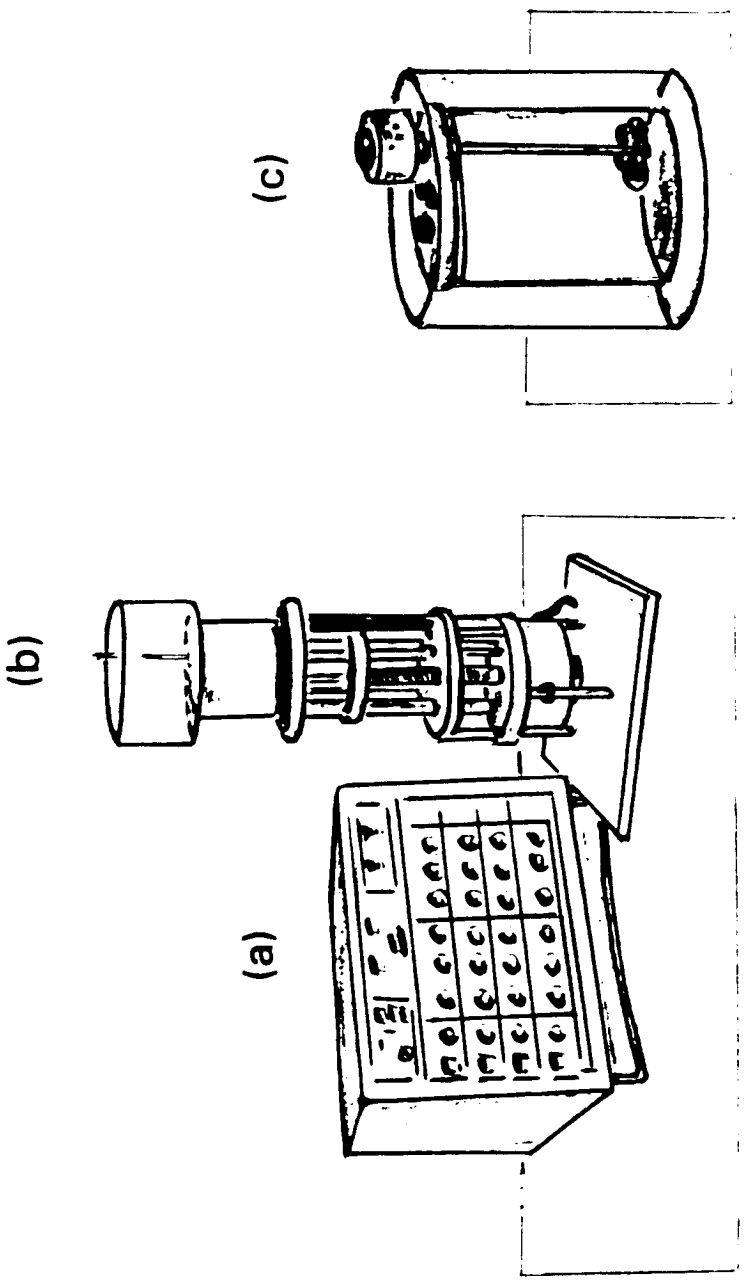

Figure 3.1. Rapid-mixing freeze-quench instrumentation. (a) ram controller; (b) ram; (c) liquid N_2 and isopentane tanks.

solution of 1.0 mM metmyoglobin in 0.02 M Trizma-HCl and 0.1 M KNO_3 buffer, pH = 7.8 was shot against buffer or against 25 mM sodium azide in buffer. The binding of azide ion to metmyoglobin caused the conversion of the g′≈ 5 high spin Fe^{3+} to low spin, and therefore, to the disappearance of the g′ ≈ 5 signal (Fig. 3.2 and Equation 3.1). The reaction exhibits pseudo-first order kinetics with respect to

$$\text{metmyoglobin-Fe}^{3+}\text{(high spin)} + N_3^- \rightleftarrows \text{metmyoglobin-Fe}^{3+}\text{-}N_3 \text{ (low spin)} \qquad (3.1)$$

metmyoglobin over a wide range of concentrations with azide at 10-fold excess. The dead time can then be determined by the following procedure. First, the first-order plot of the disappearance of the high spin EPR signal is made (Fig. 3.3) (the g ≈ 5 EPR signal is proportional to the metmyoglobin (high spin) concentration), and then the first-order equation is obtained using the linear-regression method:

$$\log[PA] = -(k_{app}/2.303)t + A \qquad (3.2)$$

where PA is the peak amplitude of the high spin g′≈ 5 EPR signal; A is the extrapolated value of log[PA] to time zero; and k_{app} is the apparent first-order rate constant. The values of A = 2.29 ± 0.09 and k_{app} = 30.6 ± 1.7 sec^{-1} were obtained from linear-regression, where k_{app} was reasonably close to the previously reported result of 34.0 sec^{-1} (Ballou

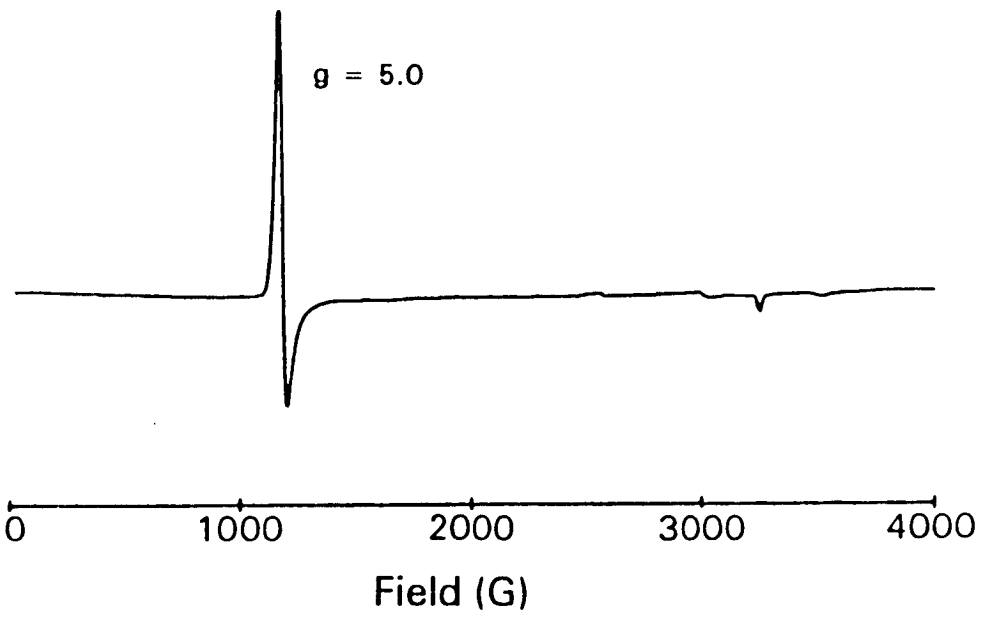

Figure 3.2. EPR spectrum of metmyoglobin. Conditions: [metmyoglobin] = 0.50 mM, [sodium azide] = 12.5 mM in 0.02 M trizma-HCl, 0.1 M KNO_3, pH 6.8. Instrument settings: field center = 2000 G; modulation amplitude = 5 G; time constant = 0.1 s; microwave power = 1 mW; scan rate = 4000 G/8 min; T = 13 K. File name: "93jan501"

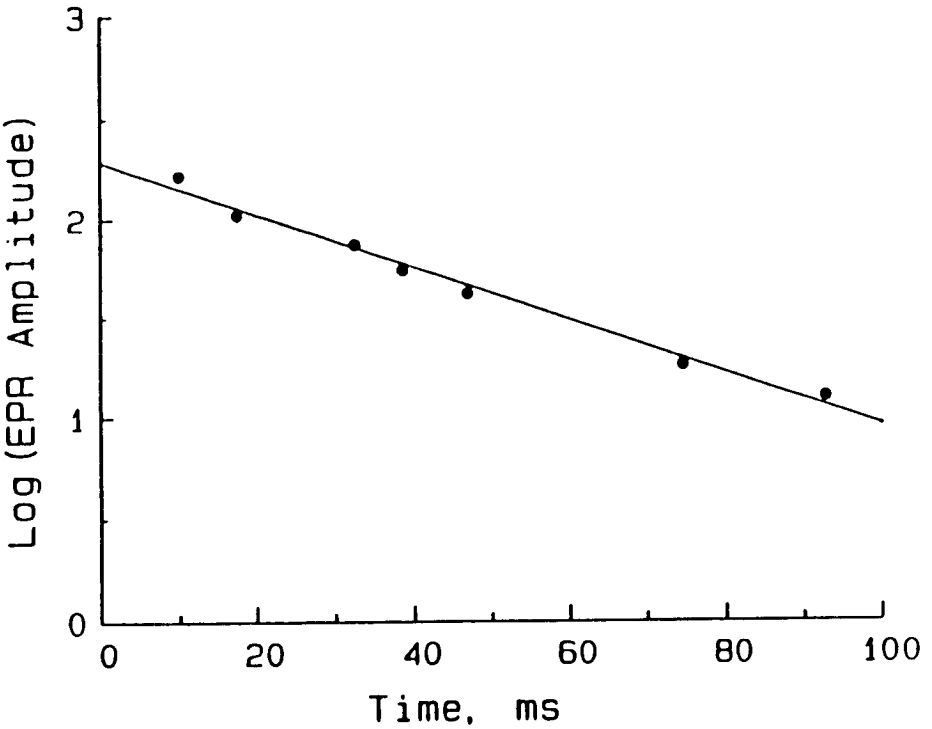

Figure 3.3. First-order plot of the metmyoglobin and sodium azide reaction. Conditions are the same as for Figure 3.2. File name: "93jan601"

& Palmer, 1974). Finally, the actual value of log[PA] at time zero, as measured in triplicate by shooting metmyoglobin against buffer alone, was substituted into equation 3.2. A dead time of 15 ± 2 ms was so determined.

Kinetic Measurements of the EPR Active Species: In the kinetic studies, samples collected in the rapid-mixing experiments were prepared by shooting 1.25 mM apoferritin in 0.1 M Mops buffer (2 ml syringe) against varying amounts of Fe^{2+} solution in 0.01 M HCl (0.5 ml syringe). The initial concentrations of the samples upon mixing were 1.0 mM apoferritin, 0.08 M Mops, and 0.40, 0.80 as well as 2.0 mM Fe^{2+}, at pH 7.10, 23 ^{0}C. Zinc inhibition experiments were carried out by mixing 1.25 mM apoferritin, 0.1 M Mops and 1.25 mM zinc(II) solution for about 2 hours, then the Zn^{2+}-protein solution was shot against a 10.0 mM Fe^{2+} solution in 0.01 M HCl.

Interaction of the Monomeric and Dimeric Complexes: Experiments designed to study interactions between the mononuclear Fe^{3+}-apoferritin complex (EPR signal at g′ = 4.3) and the dimeric Fe^{2+}-Fe^{3+} species at g′= 1.87 were performed under strictly anaerobic conditions. A solution of 1.25 mM ferritin containing 6 Fe^{3+}/protein, 61.5 mM glucose and 0.75 mg/ml catalase in 0.1 M Mops buffer was first deaerated by passing prepurified argon gas over the stirred protein solution for one hour. 0.72 mg/ml glucose oxidase was then introduced to the deaerated protein sample by a syringe to remove trace amounts of O_2. The

deoxygenated ferritin solution was then shot on the rapid-mixing instrument against a predeaerated 10.0 mM Fe^{2+} solution, pH = 2.0, at various times, or against 0.01 M HCl to give a control sample. The rapid-mixed samples were obtained following procedures described above.

Control Experiments for the Superoxide Radical as well as the Protein Radical Formed by the Fenton Reaction: A 0.7 M H_2O_2 solution was fast-mixed with 87.5 mM $NaIO_4$ in 0.05 M sodium carbonate buffer, pH = 9.5 at 23 ^{0}C. The sample was freeze-quenched at a reaction time of 4.33 seconds; a distinctive superoxide radical EPR signal was observed. A similar experiment was also performed with Mops buffer, pH = 7.00 to obtain the superoxide radical EPR signal, but it was unsuccessful. In an attempt to examine the protein radical produced due to the reaction of the hydroxyl radical with the protein, 38.0 mM H_2O_2 was shot anaerobically against 1.0 mM apoferritin containing 2 Fe^{2+} per subunit in 0.1 M Mops buffer, pH 7.10. Both H_2O_2 and the protein solutions were predeaerated. The reaction was stopped by freeze-quench at times of 30.3 and 240.3 seconds.

Stir-Mixing and Dry-Ice Acetone Freeze-Quench Experiments

Free Radical Formation: To test whether the radical signal formed during iron oxidation in the fast-mixing experiment is identical to the free radical observed previously (Grady et al., 1989), iron oxidation experiments were performed by stir-mixing 6 μl of 0.100 M Fe^{2+} in 0.01 M

HCl with 300 μl of 1.0 mM apoferritin solution in 0.1 M Mops at pH 7.1. The protein solution was prepurged with 100 % O_2 in an attempt to maximize the radical formation. Then the sample was frozen in dry-ice acetone slush around 65 seconds after initiation of iron oxidation. The experiment was also performed by reversing the order of Fe^{2+} and dioxygen addition to apoferritin solution. First, 1.0 mM apoferritin in 0.1 M Mops was deoxygenated under Ar-gas for about one hour, a microliter amount of Fe^{2+} solution was then injected into the magnetically stirred protein sample. The sample was incubated for 5 minutes, and subsequently exposed to 100 % O_2 and stirred for about 70 seconds before being frozen in dry-ice acetone bath at -77 ^{0}C.

Terbium Inhibition Experiments: Terbium(III) inhibition experiments were performed manually by mixing 0.3 ml of 1.0 mM apoferritin in subunit containing 1.0 mM Tb^{3+} in 0.1 M Mops with 1.2 μl of 0.1 M ferrous sulfate solution. The mixed samples were allowed to age from 10 to 90 seconds before being frozen in a dry-ice acetone slush. Reaction times were recorded by a stop-watch.

Redox Activity of Apoferritin: Experiments concerning the redox activity of apoferritin were performed according to the following procedure: (1) 1 ml deoxygenated solution of 1 mM apoferritin, 0.1 M Mops, 61.5 mM glucose, 0.75 mg/ml catalase and 0.72 mg/ml glucose oxidase was mixed with 5 μl ferrous sulfate (0.1 M Fe^{2+} in 10 mM HCl) which had been extensively deaerated with Ar gas; (2) the sample was then

transferred with a gas-tight syringe to an argon-flushed EPR tube followed by immediate freezing in a dry-ice acetone slush. The time interval from initial mixing to freezing was around 5 minutes. Two control samples without apoferritin or without Fe^{2+} were prepared under the same experimental conditions.

Experiments Involving the Fenton Reaction: *Addition of H_2O_2 to the Fe^{2+}-protein solution:* 6 μl of 0.100 M Fe^{2+} solution was injected into 300 μl of 1.0 mM predeoxygenated apoferritin solution (in 0.1 M Mops, pH 7.1) and was incubated for 5 minutes, followed by delivering 10 μl of 3 % H_2O_2 to the Fe^{2+}-protein solution. The mixture was stirred for about 60 seconds before being frozen in the dry-ice acetone slush. *Addition of Fe^{2+} to the H_2O_2-protein solution*: the experiment was also performed by first mixing 10 μl H_2O_2 with 300 μl of 1.0 mM apoferritin solution followed by subsequent addition of 6 μl of 0.100 M Fe^{2+} solution. In this case, some brown precipitate was observed immediately after the introduction of Fe^{2+} to the H_2O_2-protein sample. Subsequently, the precipitate was centrifuged away and the solution was frozen in the dry-ice acetone bath within 5 minutes.

Iron Oxidation in rHF, rLF and Various Mutants: Experiments involving the recombinant apoferritin and site-directed mutants were designed to investigate the locations of the mononuclear Fe^{3+} and the dimeric Fe^{2+}-Fe^{3+} binding sites on ferritin. The mixed-valence protein samples were

prepared following procedures as described previously (Hanna et al., 1991). A desired amount of Fe^{2+} was first introduced to 0.5 mM oxygenated apoferritin solution (rHF, rLF, 222 or S1) in 0.1 M Hepes and 0.15 M Nacl, at pH 7.1, and the solution was allowed to react in air for about 20 minutes. The resultant sample was then deaerated under argon gas for 30 minutes followed by the addition of a small amount of oxygen-free Fe^{2+} solution. The prepared sample was Subsequently frozen in dry ice acetone slush bath.

EPR Measurements

EPR spectra were recorded on a Varian E-4 spectrometer at 77 K or on a Varian E-9 spectrometer at liquid helium temperatures using an Air Products Helitran low temperature flow cryostat with a Cryo Industries of America transfer line. Temperatures were measured before and after each spectrum run with a low temperature detector. The EPR spectrometers were interfaced to an ISA standard Intel based 80486 computer using data acquisition hardware and EPRWare software written by Scientific Software Services. The same computer was used for data manipulation with EPRWare software.

Strong pitch (g = 2.0028) and the standard sample, Mn^{2+} in CaO (g_0 = 2.0011), were employed to calculate the g-factors of the EPR signals (Chasteen et al., 1993). Spin quantitations were determined by using a 0.36 mM transferrin solution in 0.1 M Hepes, 0,01 M $NaHCO_3$, pH = 7.5, for the g'

= 4.3 signal and 0.5 mM $Cu(NO_3)_2$ in 25% glycerol, pH = 2.0, for the radical and the mixed-valence signals. The normalized areas for both the unknown and standard signals were calculated from Equation 3.3.

$$A = \frac{DI * (SR)^2 * T}{RG * MA * (P)^{1/2} * g_p} \qquad (3.3)$$

where DI and g_p are the double integral and the average g factor of the signal (the g-value corresponding to 1/2 the maximal value of the double integral), and SR, RG, MA, as well as P are the instrument parameters representing the scan range, receiver gain, modulation amplitude, and microwave power respectively. The spin concentrations of the monomeric Fe^{3+}-protein and the radical signals were obtained from Equation 3.4 with Fe^{3+}-transferrin and copper nitrate

$$[unknown] = [standard] * A_{unknown} / A_{standard} \qquad (3.4)$$

as standards respectively. Similarly, the spin concentration of the mixed-valence Fe^{2+}-Fe^{3+} signal at g′ = 1.87 was calculated from Equation 3.5, which is equivalent to Equation 3.4 multiplied by a factor of Z/2 to account for the Bolzmann population of the EPR observable S = 1/2 ground state. Z, given by equation 3.6, is the partition function

$$[\text{unknown}] = [\text{standard}] * A_{\text{unknown}} * Z / 2A_{\text{standard}} \qquad (3.5)$$

$$Z = 2 + 4\exp(3J/kT) + 6\exp(8J/kT) + 8\exp(15J/kT) + 10\exp(24J/kT) \qquad (3.6)$$

for the ladder of spin states of the mixed-valence species, J (= - 5.3 cm^{-1}), is the antiferromagnetic exchange coupling constant (Hanna et al., 1991). The double integral of the mixed-valence species $(DI)_{g' = 1.87}$ was obtained by subtracting the double integral value of the radical signal $(DI)_{g = 2.0}$ from the total integral of the two signals (Fig. 3.4, inset).

Results

The EPR-Active Species

Two iron EPR signals at g′ = 4.3 and g′ = 1.87, and a radical signal with $g_{\perp}$ = 2.0033 and $g_{\parallel}$ = 2.042 were observed in frozen solution at 7.3 K after the fast mixing of Fe^{2+} with an apoferritin solution (Fig. 3.4). While the mononuclear Fe^{3+}-apoferritin EPR signal at g′= 4.3 and the dimeric Fe^{2+}-Fe^{3+} signal (g′ = 1.87) have been well characterized previously in this laboratory (Rosenberg & Chasteen, 1982; Chasteen et al., 1985; Hanna et al., 1991), the signal at $g_{\perp}$ = 2.0033 and $g_{\parallel}$ = 2.0418 differs from the radical signal previously reported which has an apparent g factor of 2.0077 (Grady et al., 1989).

Figure 3.5 shows the different EPR features of the two radical signals produced during iron(II) oxidation in apoferritin under different experimental conditions. For convenience, the radical signal of spectrum A, obtained from a sample prepared by fast-mixing and freeze-quenching at -135 ^{0}C, is designated radical I ($g_{\perp}$ = 2.0033, $g_{\parallel}$ =2.042), while the radical signal of spectrum B, measured from a sample acquired by stir-mixing and freeze-quenching in a dry-ice acetone slush, is designated radical II (g = 2.0084). Both spectra were measured at a temperature of 8.3 K. Interestingly, the line shape of the signal in spectrum A (radical I) changed significantly with increasing temperature (Fig. 3.6), but the features of the radical II

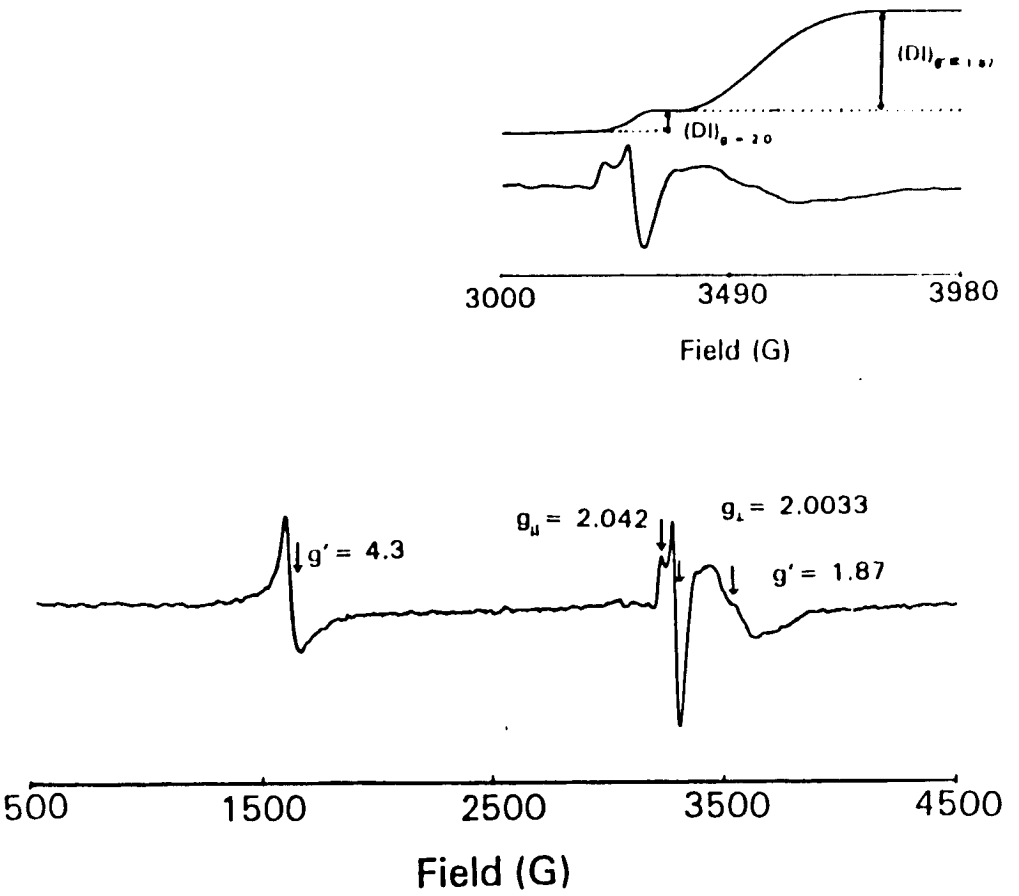

Figure 3.4. The EPR spectrum of ferritin at 7.2 K. Conditions: [Mops] = 80 mM, [apoferritin] = 1.0 mM subunit, $[Fe^{2+}]_0$ = 2.0 mM, pH = 7.1, reaction temperature = 23°C, reaction time = 5.4 s. Instrument settings: modulation amplitude = 10 G; receiver gain = 8000; time constant = 1 s; frequency = 9.36 GHz; scan rate = 4000 G/8 min; microwave power = 0.5 mW; T = 7.2K. Inset: the double integration of the radical and the mixed-valence signals. File name: "93ja19m1"

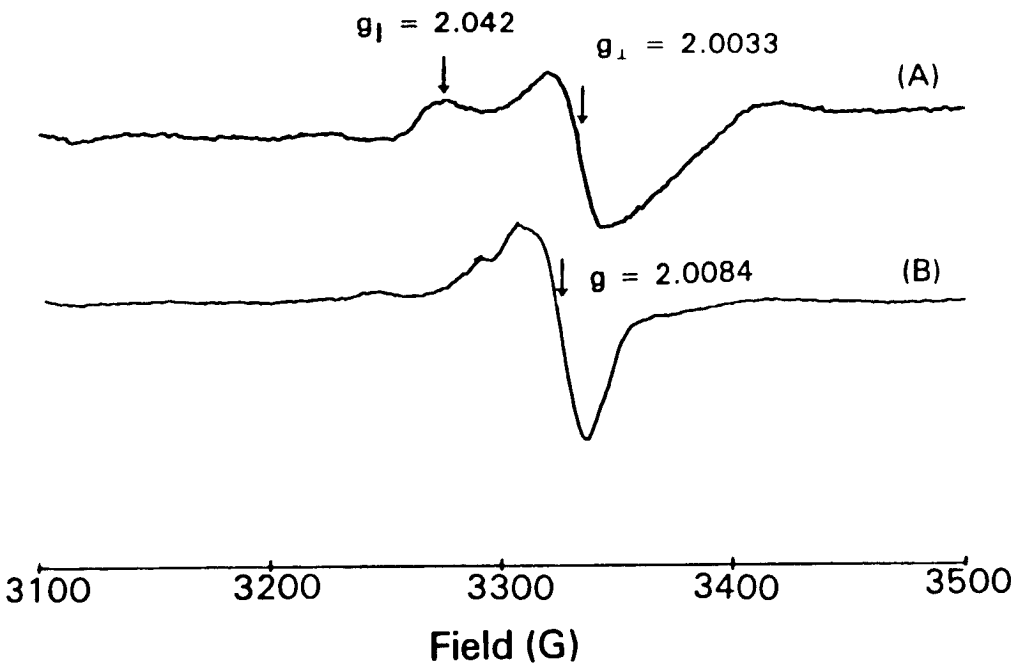

Figure 3.5. Comparison of EPR spectra of radical I (spectrum A) and radical II (spectrum B). Conditions: (A) [Mops] = 80 mM, [apoferritin] = 1.0 mM subunit, $[Fe^{2+}]_0$ = 2.0 mM, $[O_2]_0$ = 0.25 mM, pH = 7.1, reaction temperature = 23°C, reaction time = 5.4 s, prepared by the fast-mixing, freeze-quench method. (B): [Mops] = 0.10 mM, [apoferritin] = 1.0 mM subunit, $[Fe^{2+}]_0$ = 2.0 mM, $[O_2]_0$ = 1.27 mM, pH = 7.1, reaction temperature = 23°C, reaction time = 65 s, prepared by the stir-mixing method. Instrument settings: as Figure 3.4 except for scan rate of 400 G/8 min and T = 8.3 K. File name: "93se30c1 (A) & 93se15a1 (B)"

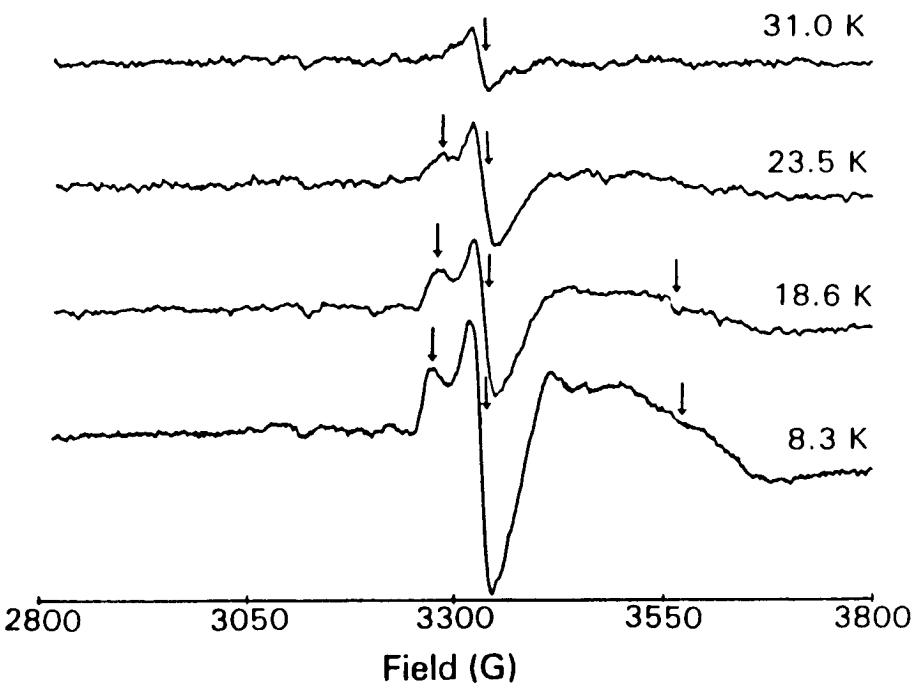

Figure 3.6. Temperature dependence of the radical I signal. Conditions: as listed in Figure 3.5 for spectrum A. File name: "93se30c4 (A), 93se30c6 (B), 93se30c3 (C) and 93se30c2 (D)"

signal in spectrum B were only slightly affected by temperature changes (Fig. 3.7, spectrum D at 8.3 K and spectrum E at 77 K).

Temperature Dependence - Curie's Law

Figure 3.6 illustrates the temperature dependence of EPR signals at $g_{\parallel}$ = 2.0418, $g_{\perp}$ = 2.0033 and g′ = 1.87. The EPR amplitudes of all three signals decrease with increasing temperature in accord with Curie's Law (Equation 3.7). To test whether the $g_{\parallel}$ = 2.0418 signal is related to the

$$\text{EPR Intensity} = \text{Constant}/T \qquad (3.7)$$

mixed-valence Fe^{2+}-Fe^{3+} species or is just the $g_{\parallel}$ factor of the radical I signal as assumed, EPR amplitudes of the three signals were measured at various temperatures. The relationships of EPR amplitude versus 1/T or (EPR amplitude * T) versus temperature for the three EPR signals at g′ = 1.87, g = 2.0033 and g = 2.0418 were plotted in Figures 3.8, 3.9 and 3.10 respectively. The dotted line in each figure is the corresponding Curie's Law. Due to their similar temperature dependence, it is evident that the signals at g = 2.0033 and g = 2.0418 are indeed the $g_{\perp}$ and the $g_{\parallel}$ factors of the same radical and they are not related to the mixed-valence species at g′ = 1.87 (Fig. 3.9 and 3.10). In accord with previously reported results, the temperature dependence of the mixed-valence signal at g′ = 1.87 deviated from the

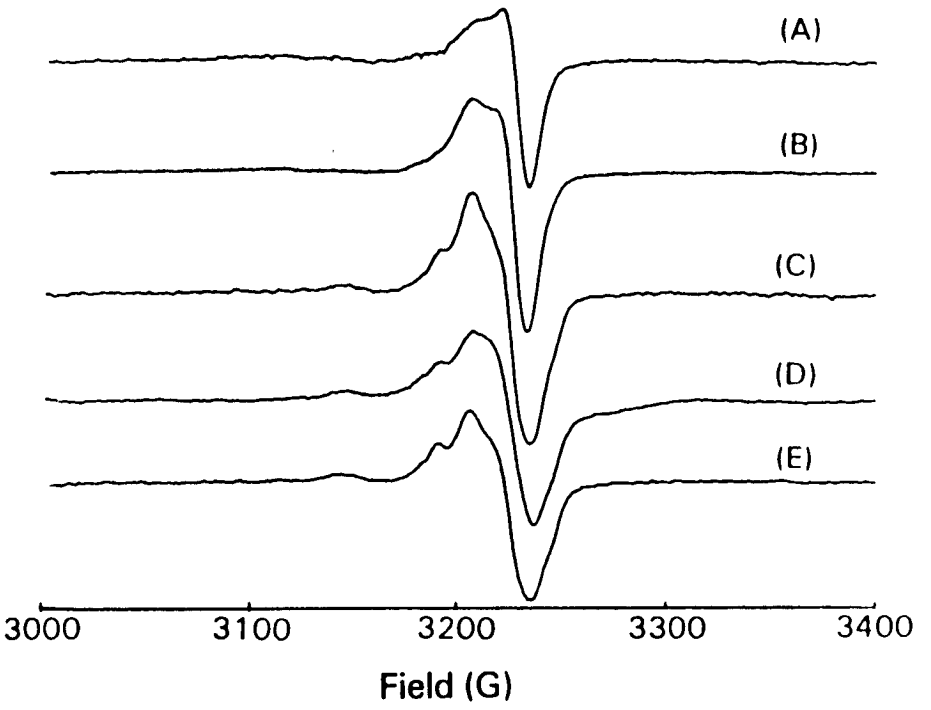

Figure 3.7. Comparison of several radical II signals produced by the stir-mixing method under different reaction conditions. Conditions for (A) & (B): [apoferritin] = 1.0 mM, $[H_2O_2]_0$ = 29.4 mM, $[Fe^{2+}]_0$ = 2.0 mM in 0.1 M Mops. (A) addition of Fe^{2+} to H_2O_2-protein, (B) anaerobic addition of H_2O_2 to Fe^{2+}-protein solution. Conditions for (C), (D) and (E) are as described in Figure 3.5 for spectrum B. (C) stirring in 100 % O_2 to Fe^{2+}-protein solution, (D) introducing Fe^{2+} to apoferritin containing 1.27 mM O_2. (E) is the same sample as (D). Instrument settings: field center = 3200 G; scan rate = 400 G/8 min; time constant = 1 s; modulation amplitude = 10 G; microwave power = 5 mW; temperature = 77 K for (A)-(D) and 8.3 K for (E). File name: "93se14d5 (A), 93se14c5 (B), 93se14b5 (C), 93se15a1 (D), and 93se14a5 (E)"

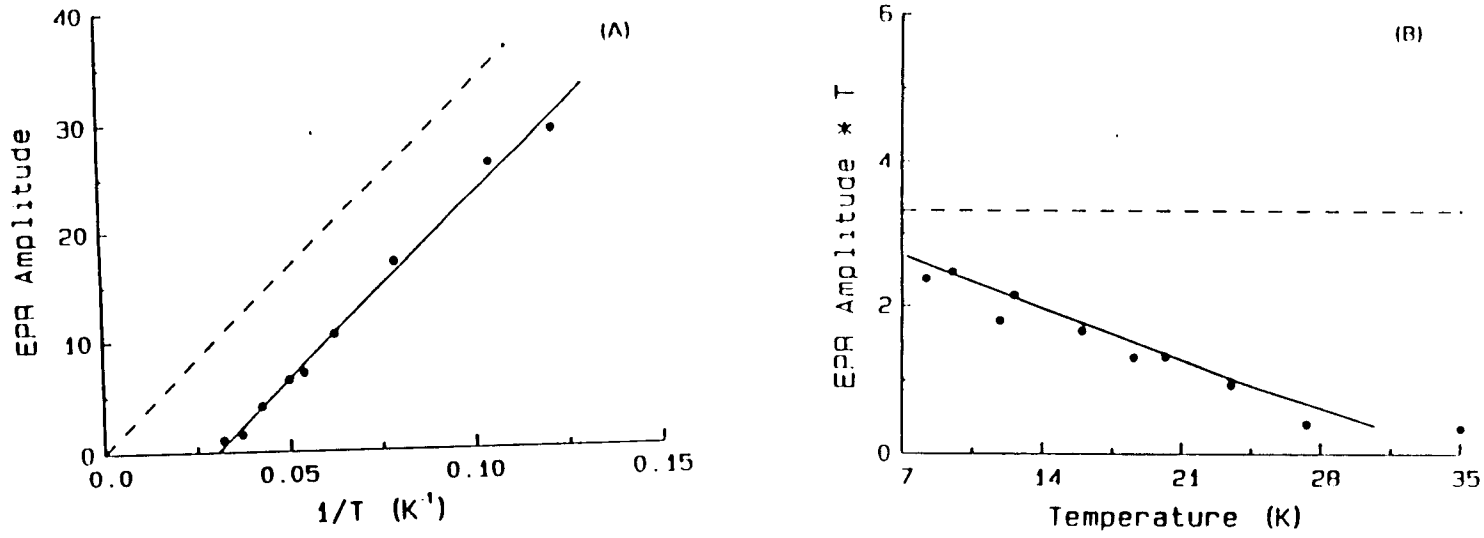

Figure 3.8. Temperature dependence of the g′ = 1.87 mixed-valence EPR signal. Plots A and B are from the same data. Conditions are the same as listed in spectrum A of Figure 3.5. File name: "93oc014 (A) & 93oc017(B)"

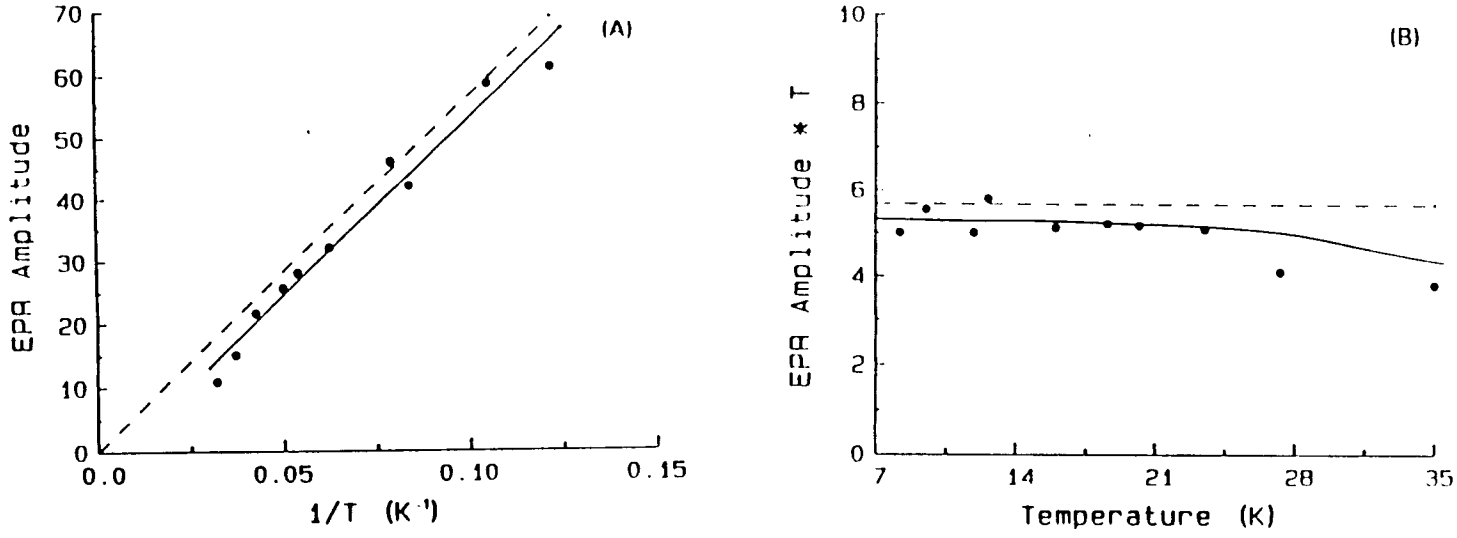

Figure 3.9. Temperature dependence of the g = 2.0033 EPR signal of radical I. Conditions are the same as listed in spectrum A of Figure 3.5. File name: "93oc015 (A) & 93oc018 (B)"

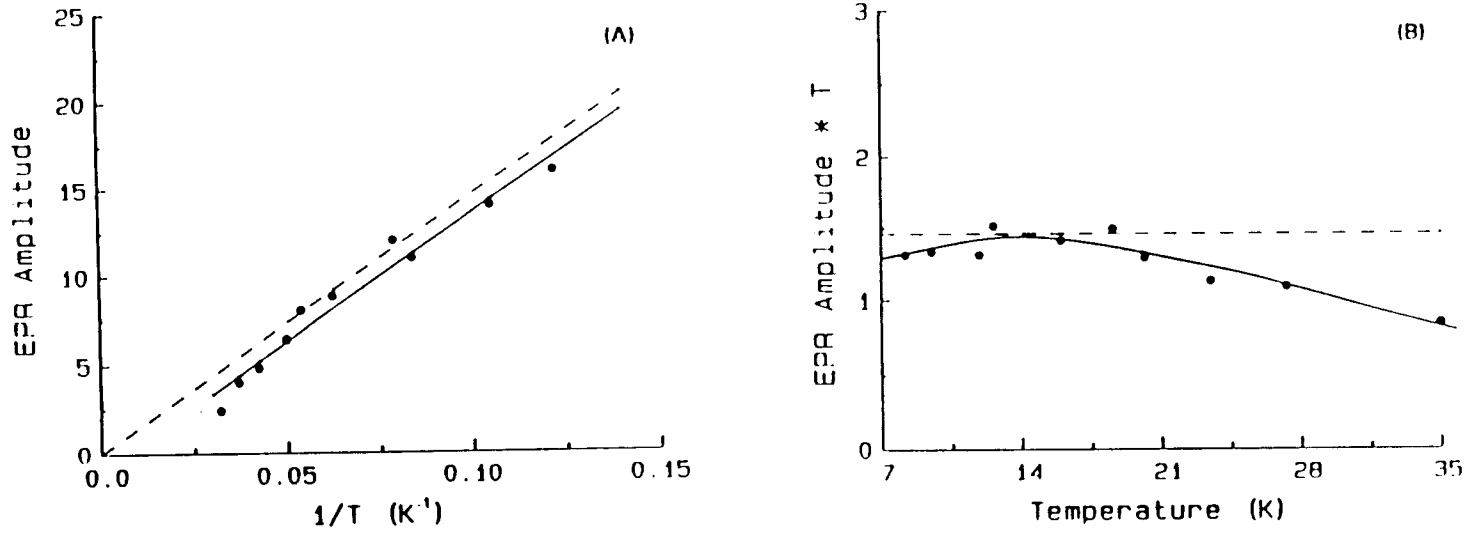

Figure 3.10. Temperature dependence of the g = 2.0418 EPR signal. Conditions are the same as listed in spectrum A of Figure 3.5. File name: "93oc016 (A) & 93oc019 (B)"

Curie's Law (Fig. 3.8). This behavior has been well characterized in Hanna's work (Hanna et al., 1991), and will not be further discussed. Finally, the effect of temperature on the EPR intensity of the radical II signal produced during stir-mixing of Fe^{2+} with apoferritin followed by freezing in dry ice/acetone 65 seconds after mixing (spectrum B in Figure 3.5) was also studied and the results plotted in Figure 3.11.

Effect of Reaction Time, pH, as well as Initial Oxygen and Fe^{2+} Concentrations on the Radical I Signal

The line shape of the radical I signal formed during the fast-mixing freeze-quench experiments was independent of reaction time (Fig. 3.12, A & B), pH and buffer (Fig. 3.12, A & C), or the initial oxygen concentration (Fig. 3.12, A & D). The reaction time was 5.3 seconds for spectra A, C and D. The signal intensity decreased with increasing reaction time from 5.3 to 480 seconds (Fig. 3.12, A & B) and pH from 7.15 to 9.5 (Fig. 3.12, A & D), but greatly increased with increasing initial oxygen concentration (Fig. 3.12, $[O_2]_0$ = 0.25 mM for A and 1.27 mM for D).

The spectra in Figure 3.12 were taken near liquid helium temperature (8.3 K). However, when the spectra were measured at liquid nitrogen temperature (77 K), the effect of initial oxygen concentration on the EPR intensity of the radical signal was insignificant (Fig. 3.13). This result indicates that there are at least two species involved in

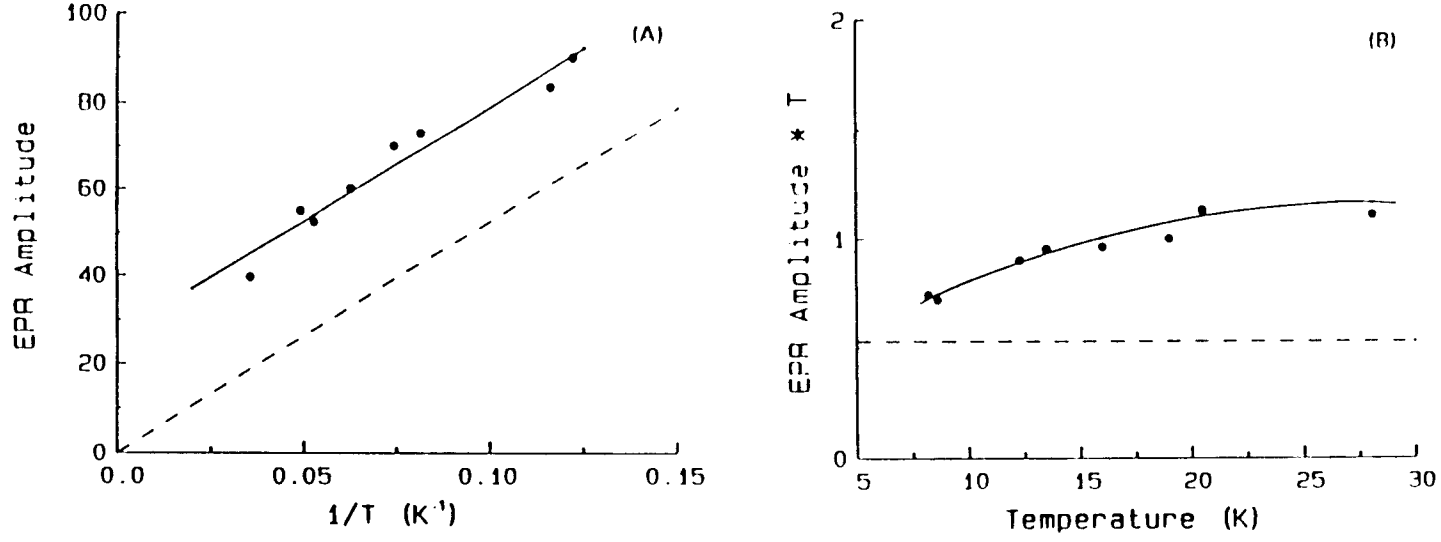

Figure 3.11. Temperature dependence of the radical II EPR signal. Conditions are the same as listed in spectrum B of Figure 3.5. File name: "93oc0111 (A) & 93oc0112 (B)"

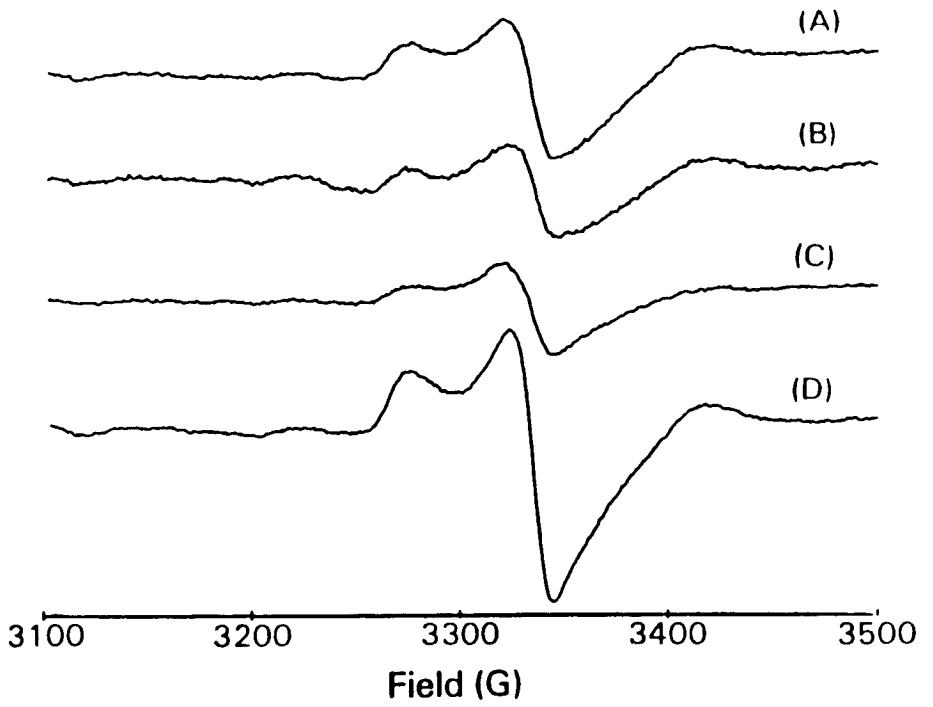

Figure 3.12. EPR spectra of radical I signal formed under different conditions. Conditions: [apoferritin] = 1.0 mM subunit, $[Fe^{2+}]_0$ = 2.0 mM, reaction temperature = 23 ^{0}C, prepared by fast-mixing freeze-quench method. (A) in 80 mM Mops buffer, pH 7.10 and $[O_2]_0$ = 0.25 mM at a reaction time of 5.3 s; (B) as (A) except at reaction time of 8.0 minutes; (C) in 80 mM Epps buffer, pH 9.5 and $[O_2]_0$ = 0.25 mM at reaction time of 5.3 seconds; (D) same as (A) except that $[O_2]_0$ = 1.27 mM. Instrument settings: as listed in Figure 3.5. File name: "93se30c1 (A), 93se30D1 (B), 93se30G1 (C), and 93se30e1 (D)"

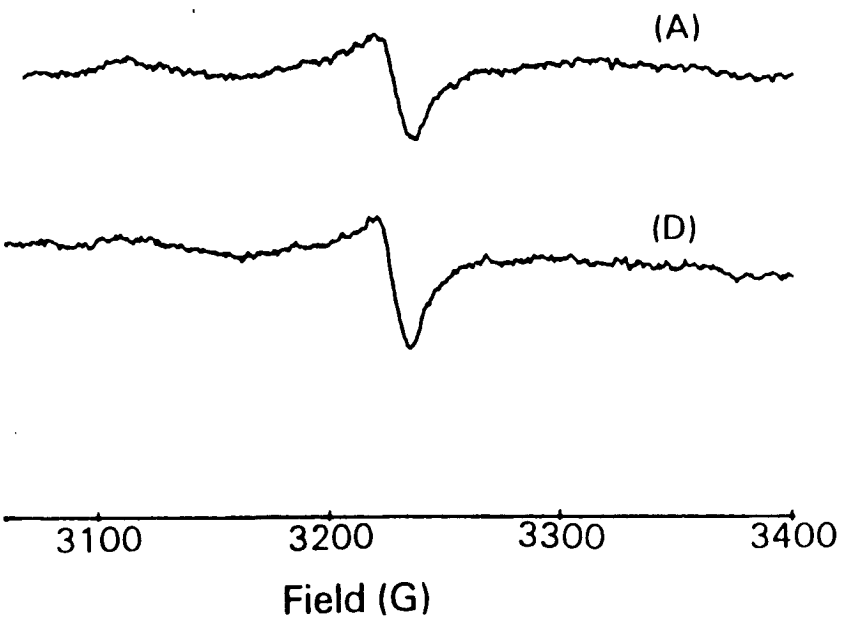

Figure 3.13. EPR spectra of samples (A) and (D) in Figure 3.12 measured at 77 K. File name: "93se22c3 (A) & 93se22e3 (B)"

the g = 2.0033 signal. One of them can be detected only at low temperature, as is the case for the mixed-valence signal.

Figure 3.14 shows the effect of initial iron(II) concentration on the EPR amplitudes of the mixed-valence signal at g'= 1.87, and the radical I signal at $g_\perp$ = 2.0033 and $g_\parallel$ = 2.042. It is evident from the figure that the signal at $g_\parallel$ = 2.042 is not associated with the mixed-valence Fe^{2+}-Fe^{3+} species at g'= 1.87 since the two signals changed differently with the initial Fe^{2+} concentration. By contrast, changes in the EPR amplitude of the $g_\perp$ = 2.0033 signal with $[Fe^{2+}]_0$ approximately correspond to those of the $g_\parallel$ = 2.042 signals, a result further indicating that both come from radical I which has axial magnetic symmetry.

Studies of the Origin of the Radical Species

The line-shape and g-factor of the radical II signal produced during iron oxidation by oxygen in apoferritin (Fig. 3.7, C & E) are similar to those of the radical signal generated by stir-mixing H_2O_2 with a Fe^{2+}-protein solution (Fig. 3.7, B) or by mixing Fe^{2+} with an apoferritin-H_2O_2 solution (Fig. 3.7, A). This result suggests that Fenton reaction (Equation 3.8) is involved in the formation of radical II.

While the sequence of addition of Fe^{2+} and O_2

$$Fe^{2+} + H_2O_2 = Fe^{2+} + OH + OH^{\bullet} \qquad (3.8)$$

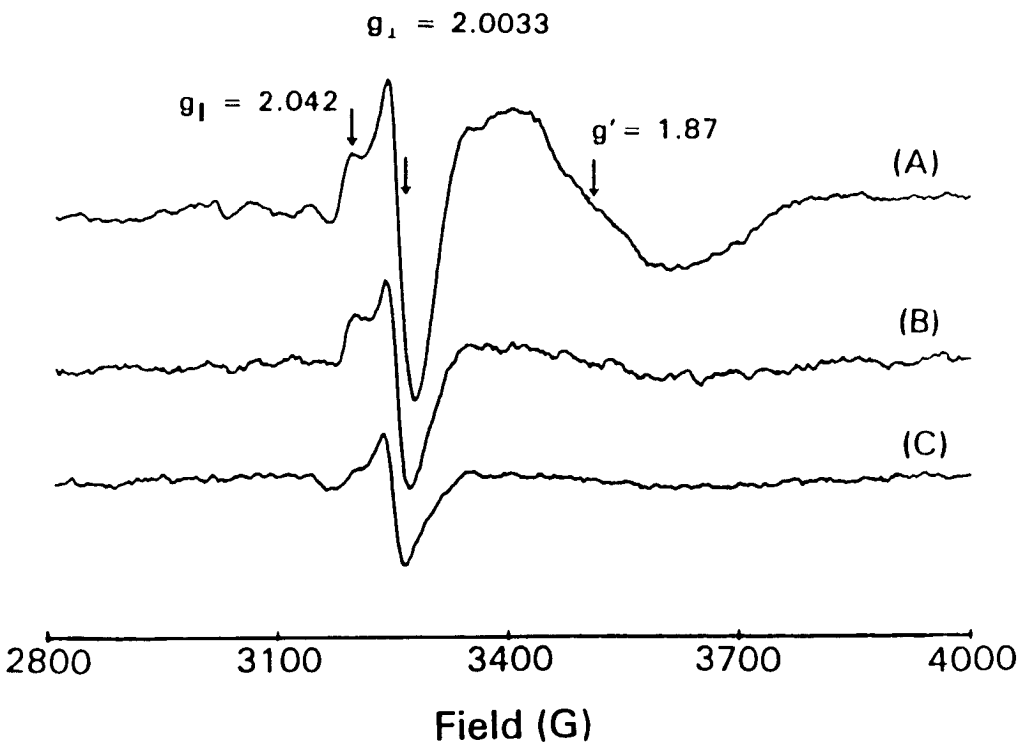

Figure 3.14. Dependence of the EPR spectra of the radical I and the mixed-valence signals on the initial Fe^{2+} concentrations. Conditions: [apoferritin] = 1.0 mM, $[O_2]_0$ = 0.25 mM in 80 mM Mops buffer, pH 7.1, $[Fe^{2+}]_0$ = 2.0 mM for (A), 0.8 mM for (B) and 0.4 mM for (C), reaction temperature 23 ^{0}C, reaction time = 5.4 seconds, prepared by rapid-mixing freeze quench. Instrument settings as listed in Figure 3.4. File name: "93ja29g1 (A), 93ma16c1 (B), and 93ap203 (C)"

to apoferritin makes no difference to the line-shape of the radical II signal, the intensity of the radical II signal produced by anaerobic addition of Fe^{2+} to apoferritin followed by admission of pure O_2 (Fig. 3.7, C) was larger than the one produced by the reversed addition of Fe^{2+} to apoferritin solution containing O_2 (Fig. 3.7, E) (see Materials and Methods). This result suggests that prior binding of Fe^{2+} to apoferritin is important in the radical II signal formation. Similarly, the intensity of the radical signal produced by stir-mixing H_2O_2 with a Fe^{2+}-protein solution (Fig. 3.7, B) is about 4 times stronger than the one generated by mixing Fe^{2+} with an apoferritin-H_2O_2 solution (Fig. 3.7, A).

Figure 3.15 shows the EPR spectra of the superoxide radical (spectra A and B), the radical I produced during fast-mixing of Fe^{2+} with apoferritin solution in the presence of O_2 (spectrum C) as well as the radical formed during the fast-mixing of H_2O_2 with the Fe^{2+}-protein solution (spectrum D). Evidently, radical I is neither a superoxide radical nor a hydroxyl-induced protein radical. This result is consistent with the observation that neither superoxide dismutase nor catalase has any significant effect on the formation of radical I (or the mixed-valence signal) during iron uptake in ferritin (Fig. 3.16).

Formation Kinetics of the Three EPR-Active Species

The Mononuclear Fe^{3+}-Protein Complex: Figure 3.17

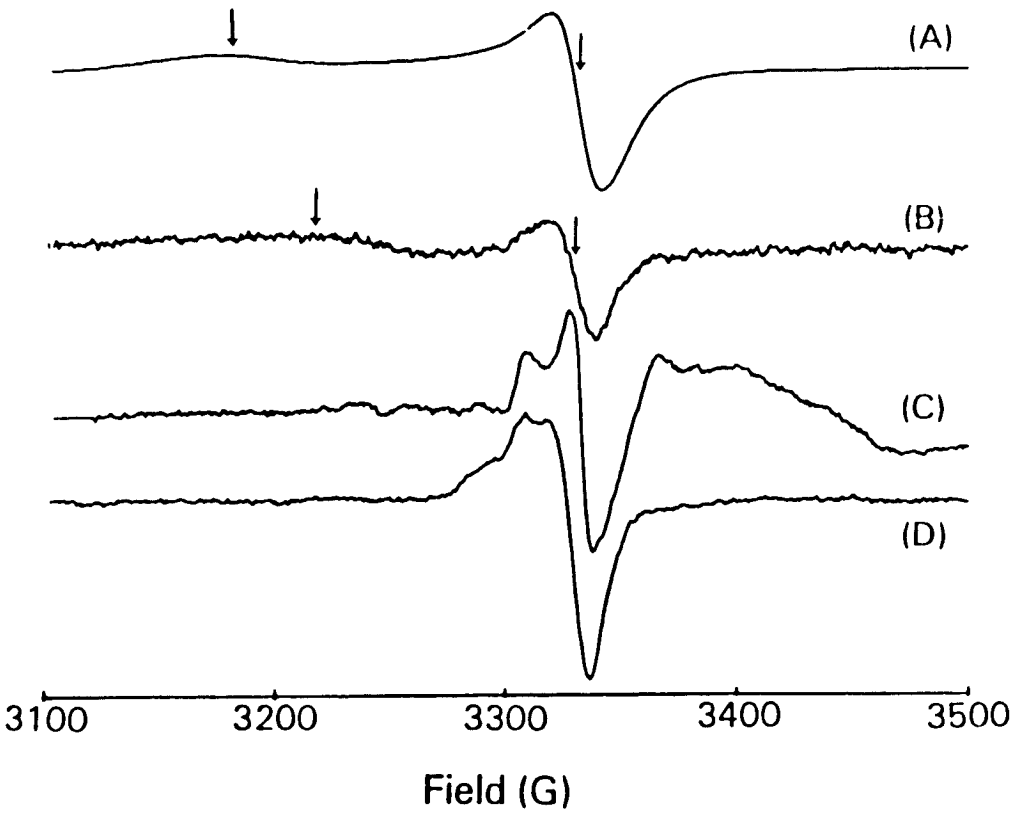

Figure 3.15. Comparison of radical I signal with superoxide radical and the hydroxyl induced protein signals. (A) [KO_2] = 2.0 mM, [d-18-crown-6] = 2.0 mM in DMSO; (B) [H_2O_2] = 0.14 M, [$NaIO_4$] = 70 mM in 50 mM Sodium Carbonate, pH 9.5; (C) as described in spectrum A of Figure 3.5; (D) [H_2O_2] = 7.6 mM, [apoferritin] = 0.1 mM, [Fe^{2+}]0 = 2.0 mM, $[O_2]_0$ = 0.0 in 80 mM Mops. See Materials and Methods for detailed experimental procedures. EPR measurments were performed on the Varian E-9 spectrometer at 8.3 K for (B)-(D) and on the Varian E-4 spectrometer at 77 K for (A). File name: "93jy231 (A), 93se30j2 (B), 93se30c2 (C), and 93se30b1 (D)"

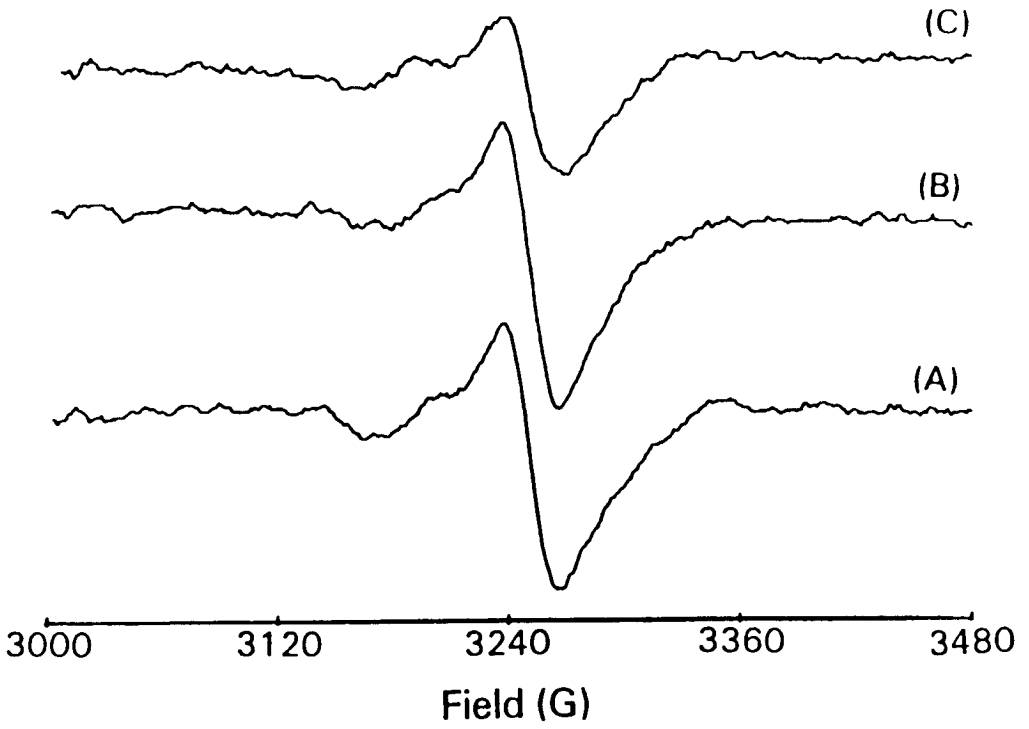

Figure 3.16. Effect of superoxide dismutase and catalase on the radical I signal. Conditions: (A) [apoferritin] = 1.0 mM, $[O_2]_0$ = 0.25 mM in 80 mM Mops, pH = 7.1, $[Fe^{2+}]_0$ = 0.4 mM, reaction time = 5.4 sec; (B) (A) + 380 U/ml superoxide dismutase; (C) (A) + 380 U/ml catalase. Instrument setting as listed in Figure 3.4. File name: "93ap203 (A), 93ap213 (B), and 93ap215 (C)"

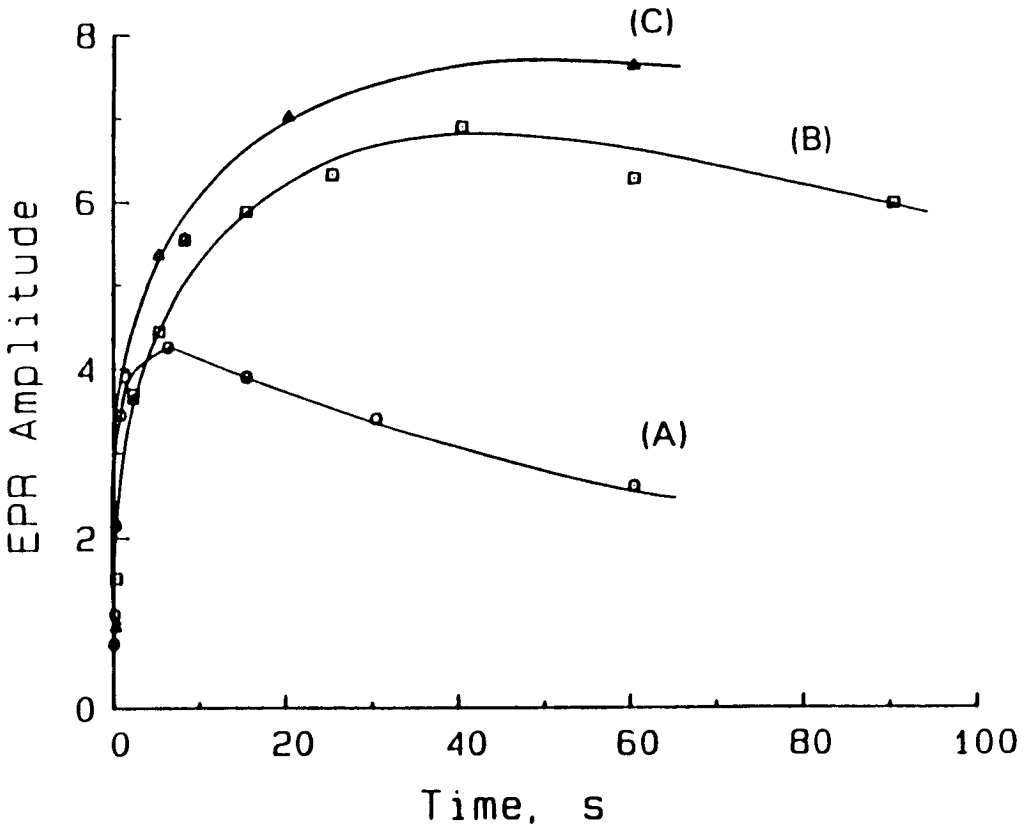

Figure 3.17. EPR amplitude versus time for the mononuclear Fe^{3+}-protein signal at g′= 4.3. Conditions: [Mops] = 80 mM, [apoferritin] = 1.0 mM subunit, pH = 7.1, reaction temperature = 23 ^{0}C, $[Fe^{2+}]_0$ = 2.0 mM (curve A), 0.8 mM (curve B) and 0.4 mM (curve C). Instrument settings are the same as in Figure 3.4. File name: "93ma107 (A), 93ma304 (B), and 93ju093 (C)"

shows the formation kinetics of the EPR species at g′ = 4.3 under different initial Fe^{2+} concentrations. The concentration of the dissolved dioxygen is about 0.25 mM at room temperature. In the presence of excess ferrous ion ($[Fe^{2+}]_0$ = 2.0 mM), the g′ = 4.3 EPR signals were formed within milliseconds, reached a maximum at around 10 seconds, and then rapidly decayed (Fig. 3.17, curve A). At lower concentration of $[Fe^{2+}]_0$ (0.80 mM), a maximum in EPR amplitude was observed at a reaction time of about 40 seconds followed by a slow decay (Fig. 3.17, curve B). A hyperbolic relation of the EPR amplitude versus time was observed at $[Fe^{2+}]_0$ = 0.40 mM (Fig. 3.17, curve C). In this case, no remaining Fe^{2+} was present in solution since sufficient O_2 was present to consume all the added Fe^{2+}.

The Mixed-valence Fe^{2+}-Fe^{3+} Species: The EPR amplitude versus time for the mixed-valence (g =1.87) signals were quite distinctive for each initial Fe^{2+} concentration (Fig. 3.18). While it followed the same trend as the g′= 4.3 signal at $[Fe^{2+}]_0$ = 2.0 mM, that is, an initial burst in EPR amplitude followed by an immediate rapid decrease of the signal (Fig. 3.18, curve A), the maximum point in the EPR amplitude at $[Fe^{2+}]_0$ = 0.8 mM was not so pronounced and the subsequent signal decay was quite slow (Fig. 3.18, curve B). In addition, the mixed-valence Fe^{2+}-Fe^{3+} species was not detectable at even lower Fe^{2+} concentration (for example, $[Fe^{2+}]_0$ = 0.4 mM).

The Free Radical I at g = 2.0033: Figure 3.19

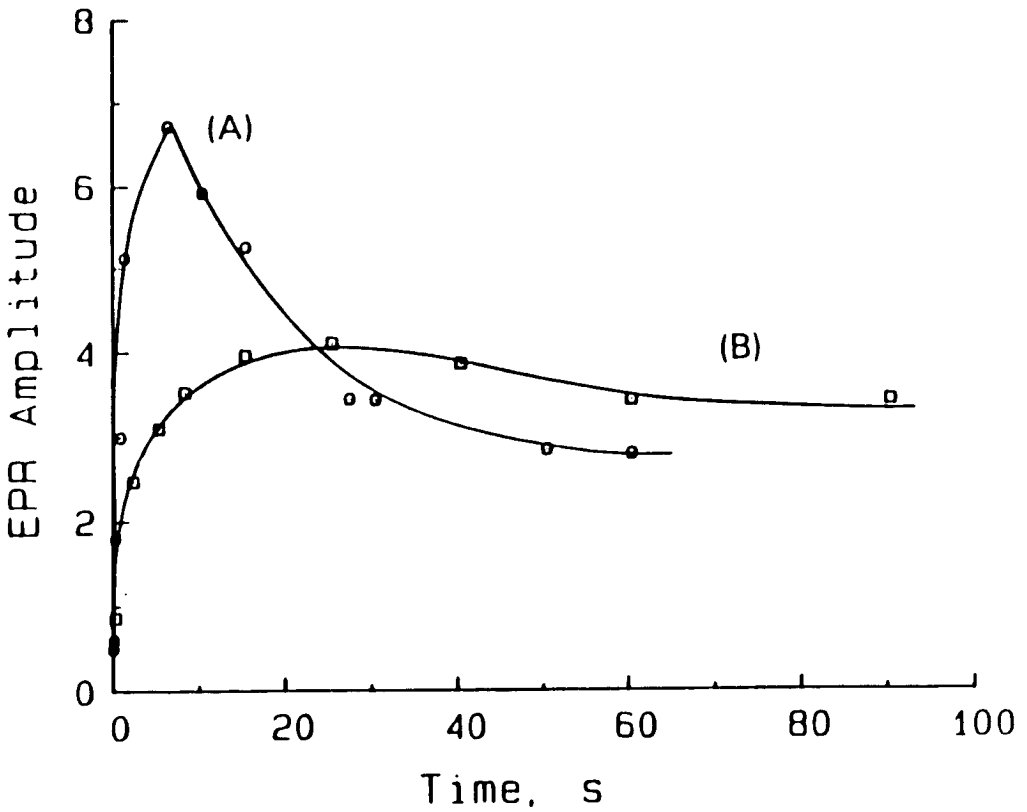

Figure 3.18. EPR amplitude versus time for the mixed-valence signal at g'= 1.87. Conditions: [Mops] = 80 mM, pH = 7.1, [apoferritin] = 1.0 mM subunit, reaction temperature = 23 ^{0}C, $[Fe^{2+}]_0$ = 2.0 mM (curve A), 0.8 mM (curve B). Instrument settings are the same as in Figure 3.4 except that microwave power = 90 mW. File name: "93ma108 (A) & 93ma306 (B)"

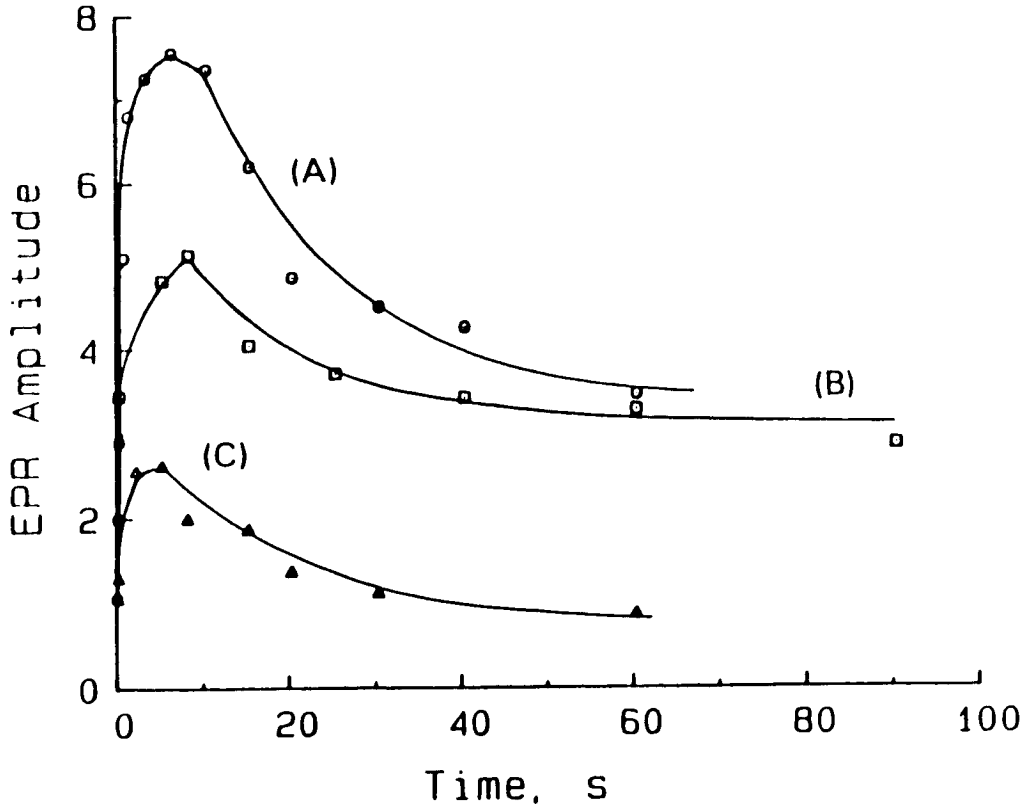

Figure 3.19. EPR amplitude versus time for the radical I signal at g = 2.0033. Experimental conditions and instrument settings are as listed in Figure 3.17. File name: "93ma109 (A), 93ma305 (B), and 93ju094 (C)"

illustrates the time dependence of the radical signal at various Fe^{2+} concentrations. Regardless of the amount of Fe^{2+} initially present in solution, the radical signal increased rapidly with time, reached a maxima at about 10 seconds, then decayed away in two phases, a faster phase and a slower phase. For example, about 40 % of the EPR signal decayed within 10 seconds in the fast phase, while in the slower phase, it took 70 seconds to bring about only a 20 % decline in the signal intensity. Nevertheless, the maximum intensity of the signal at a particular time is proportional to the initial Fe^{2+} concentrations. Figure 3.20 shows the EPR spectra of the radical I signal at different reaction time. The line shape is time independent.

The maximum spin concentrations of the three EPR-active species formed at various initial Fe^{2+} concentrations were calculated by a double integration of the EPR signal using the standard solutions described in Materials and Methods. The results are summarized in Table 3.1.

Metal Ions Inhibiting Effect

Zn^{2+} and Tb^{3+} inhibition of the formation of various EPR species as well as the effect of these metal ions on iron oxidation were studied. Figures 3.21, 3.22 and 3.23 illustrate Zn^{2+} inhibition of the formation of three EPR species, at $g' = 4.3$, $g' = 1.87$ and $g = 2.0033$ respectively. A total of twenty-four Zn^{2+} per protein molecule were employed in each experiment. In addition, Zn^{2+} inhibition

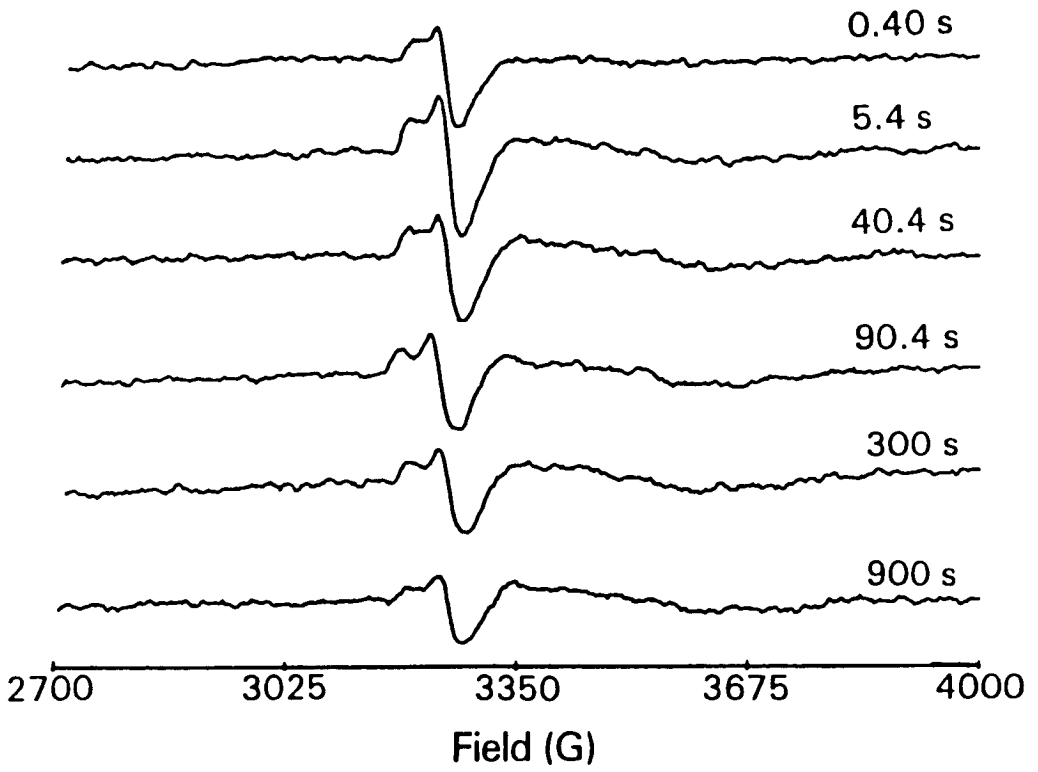

Figure 3.20. The lineshape of the radical I signal at different reaction times. Condition: [Mops] = 80 mM, [apoferritin] = 1.0 mM subunit, pH = 7.1, reaction temperature = 23 ^{0}C, $[Fe^{2+}]_0$ = 0.80 mM. EPR parameters as indicated in Figure 3.4. File name: "93ma16a1, 93ma16c1, 93ma16g1, 93ma16i1, 93ma16k1, and 93ma16l1"

Table 3.1

The Maximum Signal Intensities of the Three EPR-Active Species at different initial Fe^{2+} concentrations[1,2,3]

$[Fe^{2+}]_0$, mM	2.0	0.8	0.4
$[C]_{g'=4.3}$, μM	70	100	120
$[C]_{g'=1.87}$, μM	51	23	0
$[C]_{g=2.0033}$, μM	20	10	8

[1]Conditions: [apoferritin] = 1.0 mM, $[O_2]_0$ = 0.25 mM in 80 mM Mops, pH 7.1 at 23^0 C.

[2]The field ranges for the double integrations of the g′ = 4.3, g′ = 1.87, and the g = 2.0033 signals are approximately 1200 - 2300 G, 3020 - 4100 G and 3020G - 3360 G respectively. EPR microwave frequency is 9.36 GHz.

[3]Errors in each data are about ± 10 %.

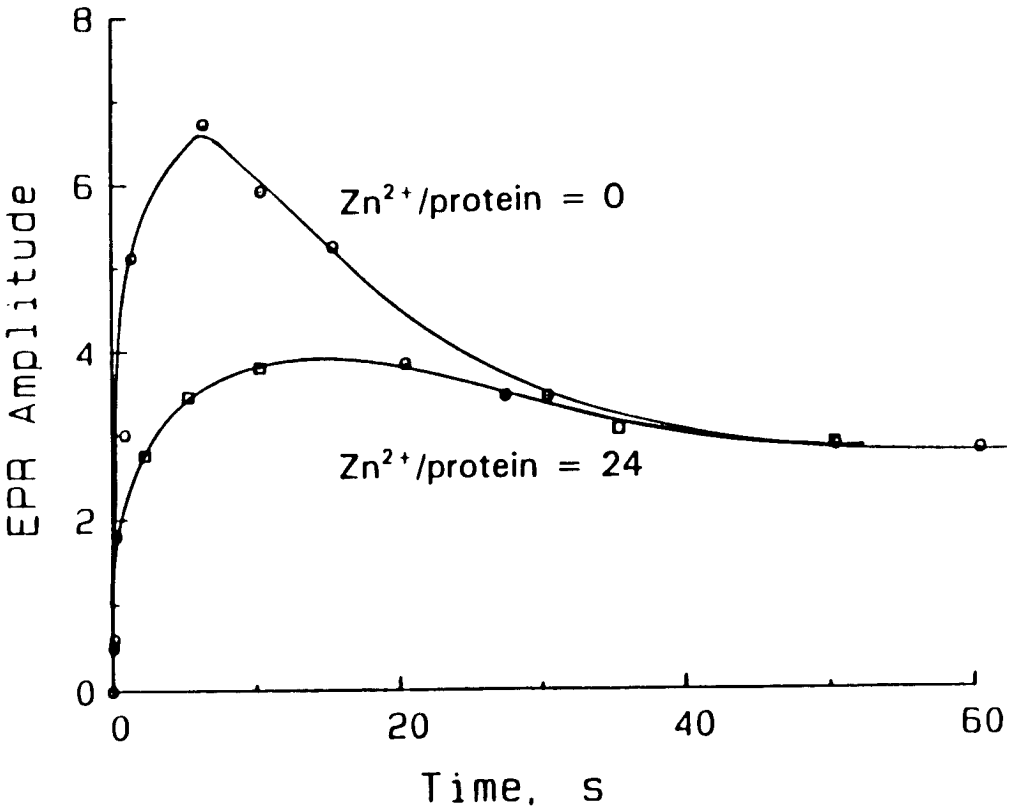

Figure 3.21. Zn^{2+} inhibition on the formation of the g '= 4.3 signal. Conditions: [Mops] = 80 mM, [apoferritin] = 1.0 mM subunit, pH = 7.1, reaction temperature = 23 ^{0}C, $[Fe^{2+}]_0$ = 2.0 mM. EPR parameters are as described in Figure 3.4. File name: "93ma107 (A) & 93ju284 (B)"

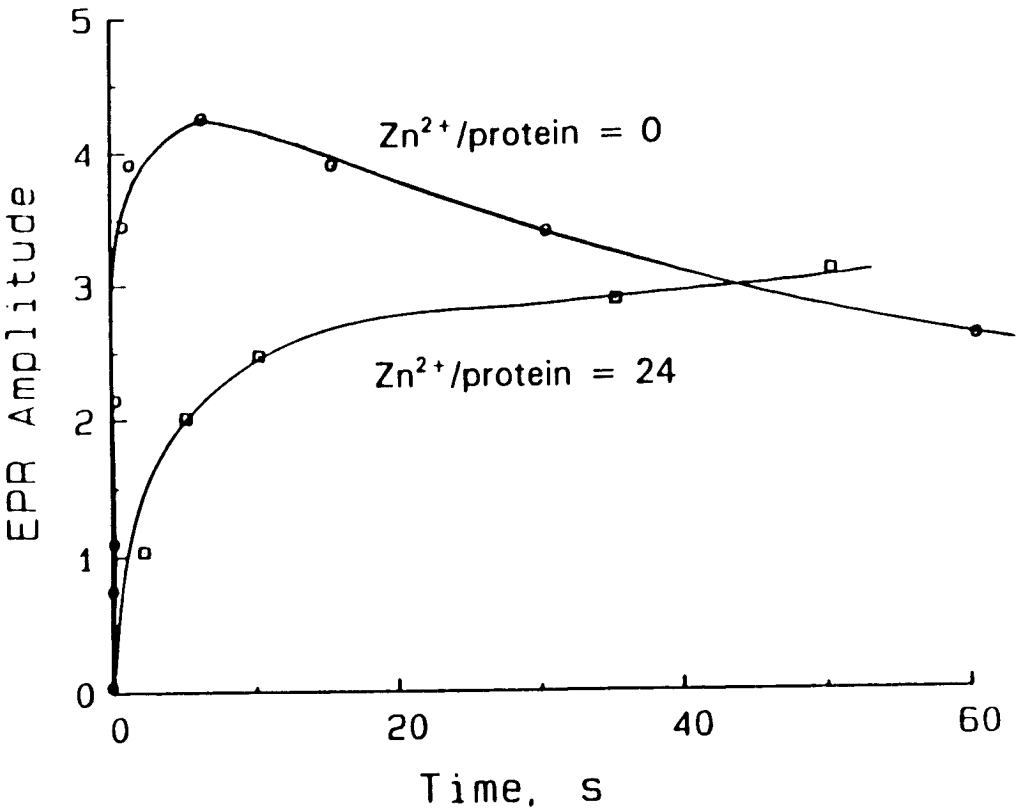

Figure 3.22. Zn^{2+} inhibition on the formation of the g′ = 1.87 mixed-valence signal. Experimental conditions and EPR parameters are the same as listed in Figure 3.21. File name: "93ma108 & 93ju286"

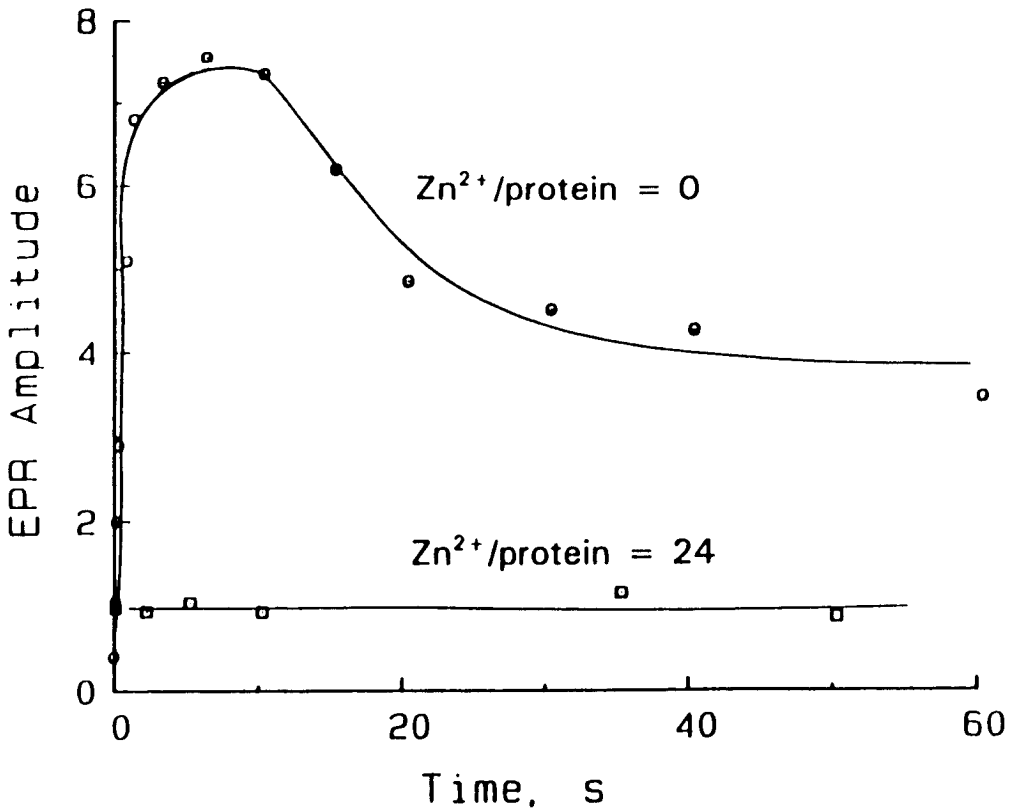

Figure 3.23. Zn^{2+} inhibition on the formation of the radical I signal at g = 2.0033. Experimental conditions and EPR parameters are the same as listed in Figure 3.21. File name: "93ma109 & 93ju285"

of the iron(II) oxidation reaction was measured with micro-electrode oximetry under the same reaction conditions and the results were shown in Figure 3.24. It is evident that the presence of Zn^{2+} significantly retards iron oxidation (Fig. 3.24). The effect of Zn^{2+} on the three EPR active species are quite different, however. It appears that the rates of formation of the g′= 4.3 and g′= 1.87 signals are significantly decreased by the presence of Zn^{2+} (Fig. 3.21 and 3.22) while the radical signal at g = 2.0033 is almost completely eliminated (Fig. 3.23).

Experiments on Tb^{3+} inhibition of the formation of the EPR-active species were performed by the stir-mixing method. The observed radical signal is from radical II (Fig. 3.25). The effects of Tb^{3+} on the formation of the g′= 4.3 and the radical II signals are shown in Figures 3.26 and 3.27 respectively. Only a 0.4 mM initial Fe^{2+} concentration was used in the Tb^{3+} inhibition experiments, thus the mixed-valence signal was not observable. The corresponding oxygen consumption versus time data are plotted in Figure 3.28. Although the initial rate of iron oxidation is only slightly slower in the presence of 24 Tb^{3+} in apoferritin (Fig. 3.28, II), the g′= 4.3 signal is greatly decreased by Tb^{3+} binding (Fig. 3.26) (note: the almost same initial rate of oxygen consumption in the presence or absence of Tb^{3+} at higher apoferritin and initial Fe^{2+} concentration is probably caused by the slower response of the oxygen electrode to a faster reaction (Fig. 3.28, I)). The inhibiting effect of

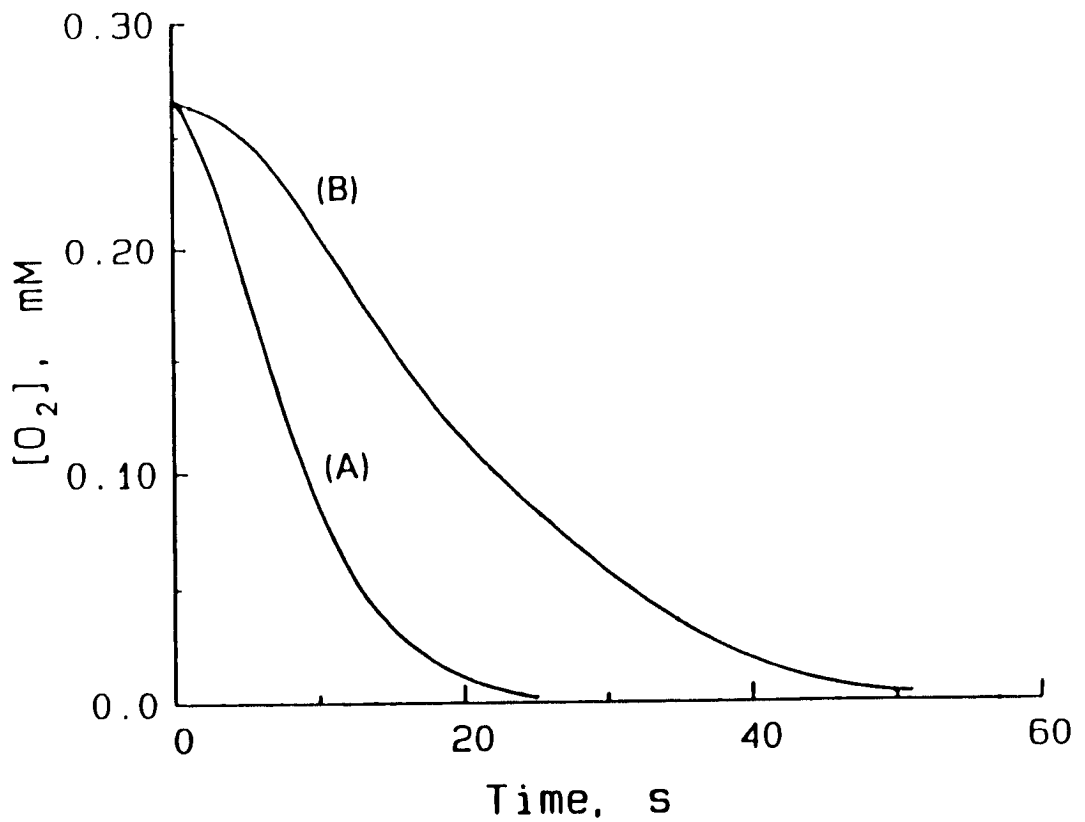

Figure 3.24. Oxygen consumption versus time for the oxidation of Fe^{2+} in the absence (curve A) and presence (curve B) of Zn^{2+}. Conditions: [Mops] = 80 mM, [apoferritin] = 1.0 mM subunit, pH = 7.1, reaction temperature = 23 ^{0}C, $[Fe^{2+}]_0$ = 2.0 mM. (A) Zn^{2+}/protein = 0; (B) Zn^{2+}/protein = 24. File name: "93jy151 (A) & 93jy152 (B)"

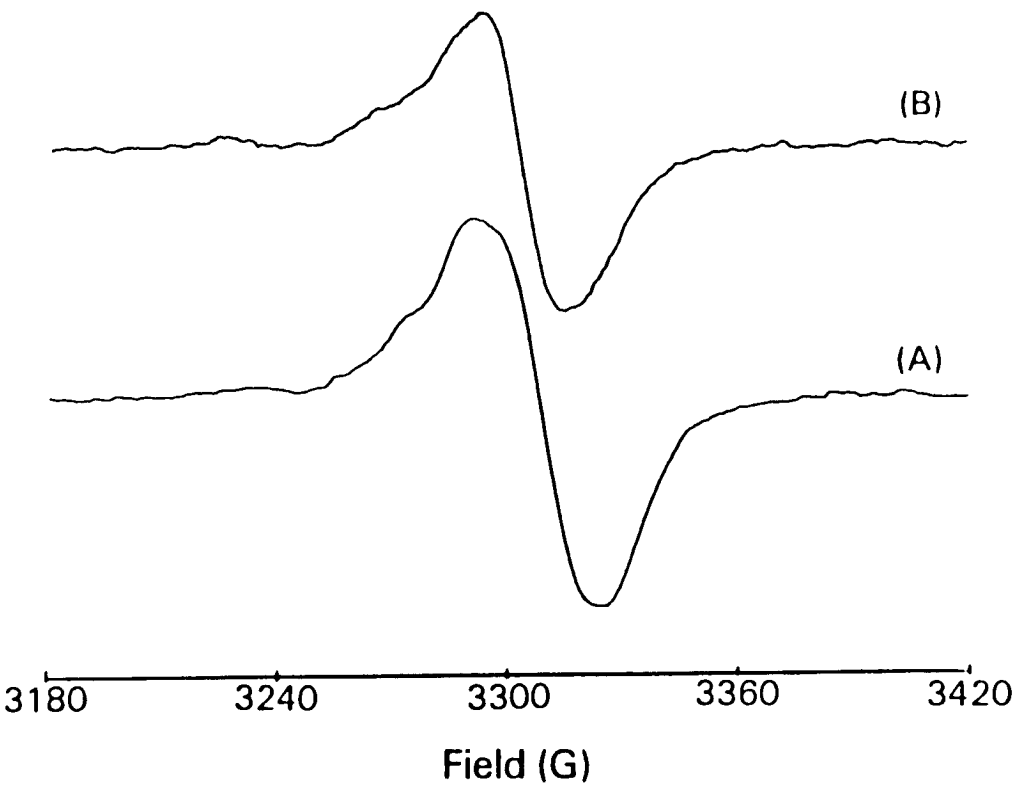

Figure 3.25. The radical II signal observed in the Tb^{3+} inhibition experiments. Conditions: [Mops] = 80 mM, [apoferritin] = 1.0 mM, $[Fe^{2+}]_0$ = 0.4 mM, pH = 7.1, reaction temperature = 23 ^{0}C, and reaction time = 37 seconds. (A) Tb^{3+}/protein = 0; (B) Tb^{3+}/protein = 24. Instrument settings: modulation amplitude = 10 G; time constant = 1 s; frequency = 9.15 GHz; receiver gain = 8000; scan rate = 4000 G/8 min; microwave power = 5 mW. File name: "93jy069 & 93jy063"

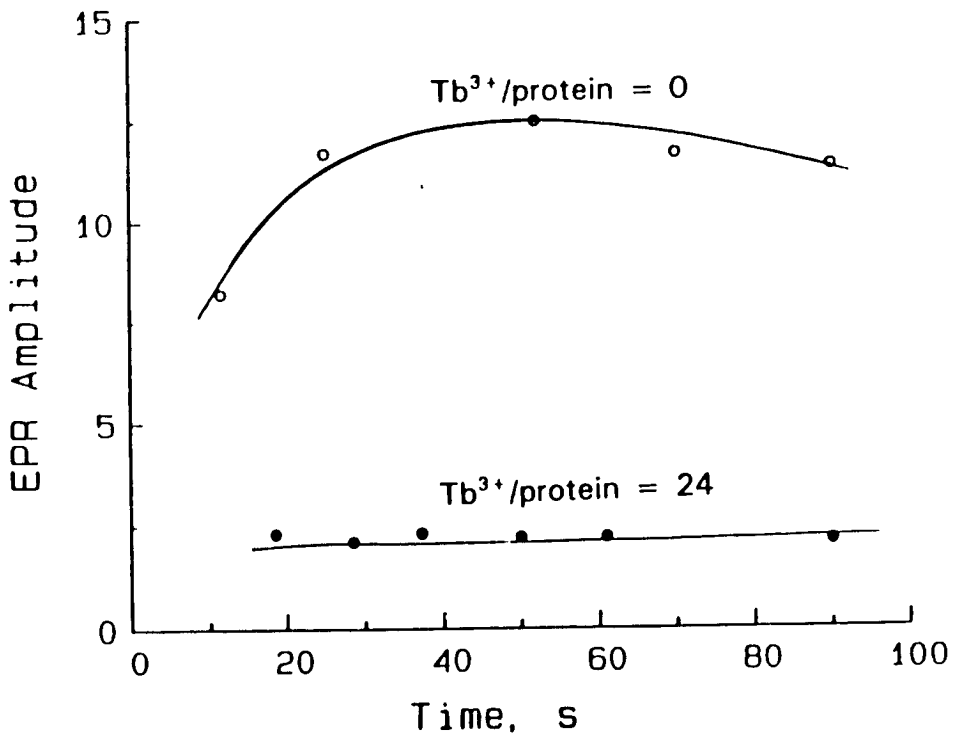

Figure 3.26. Inhibition effect of Tb^{3+} on the EPR intensities of the g′= 4.3 Fe^{3+}-protein signal. Experimental conditions and EPR parameters are the same as listed in Figure 3.25. File name: "93jy093 & 93jy091"

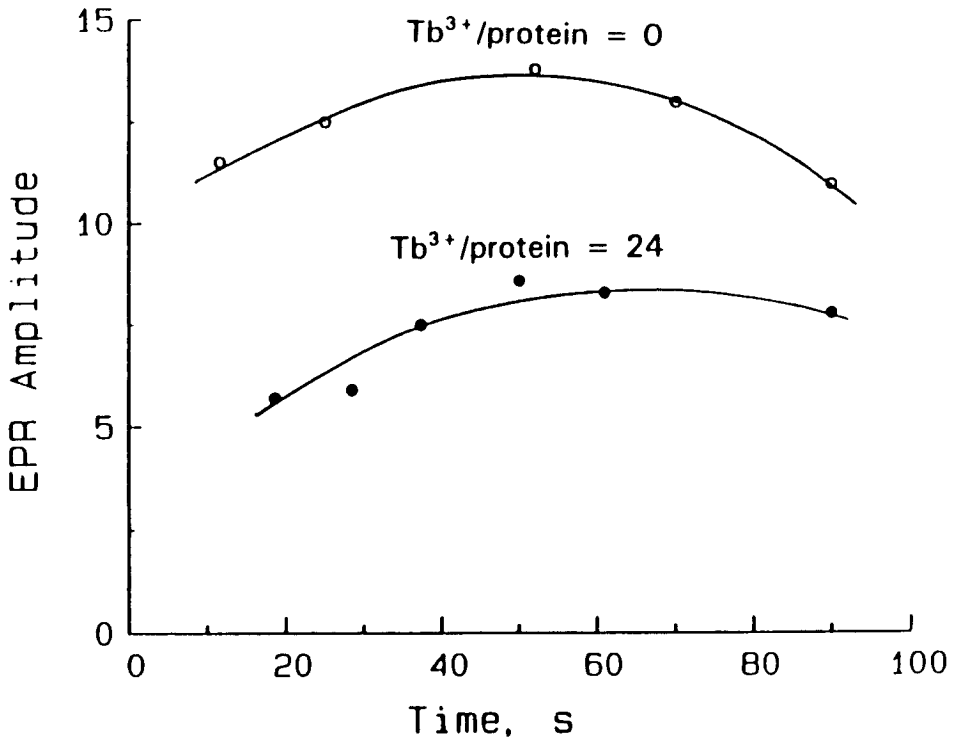

Figure 3.27. Inhibition effect of Tb^{3+} on the EPR intensities of the radical II signal. Experimental conditions and EPR parameters are the same as listed in Figure 3.24. File name: "93jy094 & 93jy092"

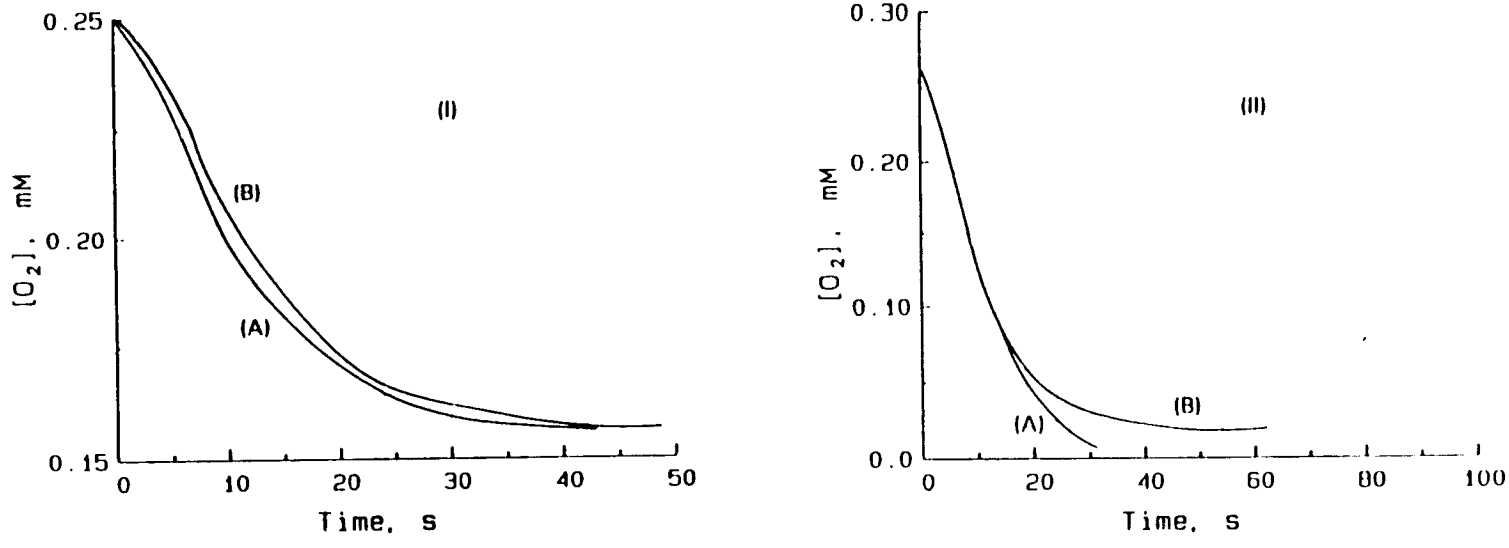

Figure 3.28. Oxygen consumption versus time for Fe^{2+} oxidation in the absence (curve A) and presence (curve B) of Tb^{3+}. Conditions: (I) [Mops] = 80 mM, [apoferritin] = 1.0 mM, $[Fe^{2+}]_0$ = 0.4 mM, pH = 7.1 and reaction temperature = 23 ^{0}C. (A) Tb^{3+}/protein = 0; (B) Tb^{3+}/protein = 24; (II) [Mops] = 80 mM, [apoferritin] = 0.2 mM, $[Fe^{2+}]_0$ = 0.22 mM, pH = 7.25 and reaction temperature = 23 ^{0}C. (A) Tb^{3+}/protein = 0; (B) Tb^{3+}/protein = 24. File name: "93jy121 (IA), 93jy122 (IB), 93se10a (IIA), and 93se10b (IIB)"

Tb^{3+} on the radical II signal is not quite as strong (Fig. 3.27).

Interaction of Mononuclear Fe^{3+}-protein and Dimeric Fe^{2+}-Fe^{3+} Species

Anaerobic fast-mixing of samples containing 6 Fe^{3+}'s per protein molecule with the Fe^{2+} solution in 0.01 M HCl (Fig. 3.29, spectra B & C) led to dramatic attenuation of the g'= 4.3 signal observed in the control experiment in which ferritin containing 6 Fe^{3+}'s per protein molecule was shot against 0.01 M HCl (Fig. 3.29, spectrum A). Meanwhile, the mixed-valence Fe^{2+}-Fe^{3+} signal at g = 1.87 appeared. Under the experimental conditions, the interaction between those two species took place within a second. The spin concentrations of the S = 1/2 Fe^{3+}-Fe^{2+} dimer (≈ 0.02 mM at reaction time of 0.17 second and ≈ 0.04 mM at reaction time of 0.33 seconds) are very close to the corresponding decrease of ≈ 0.024 and 0.05 mM in the concentrations of the Fe^{3+}-protein monomer.

Apoferritin as an Oxidant

Addition of 0.5 mM Fe^{2+} to 1.0 mM apoferritin solution under strictly anaerobic conditions produced a small amount of mononuclear Fe^{3+}-protein complex. The g'= 4.3 EPR signal was observed at 9.3 K (Fig. 3.30, spectrum A). The signal intensities are approximately the same at different reaction times of 5 and 15 minutes respectively, demonstrating that

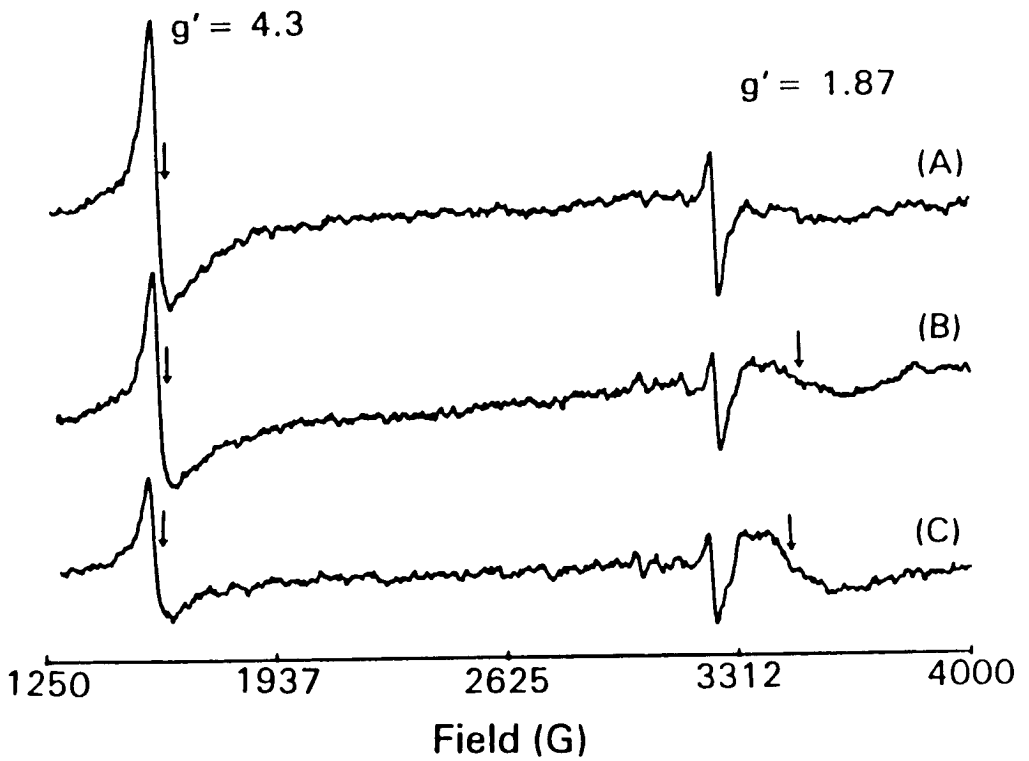

Figure 3.29. EPR spectra of ferritin containing 6 Fe^{3+} per protein in the absence (spectrum A) and presence (spectra B & C) of 48 Fe^{2+} per protein molecule. Conditions: [Mops] = 80 mM, [apoferritin] = 1.0 mM subunit, [Fe^{3+}] = 0.25 mM, [Fe^{2+}] = 0 (spectrum A) and 2.0 mM (spectra B & C), [glucose] = 49.2 mM, [glucose oxidase] = 0.58 mg/ml, [catalase] = 380 U/ml, pH = 7.15, reaction temperature: 23 ^{0}C. Aging time after anaerobically mixing Fe^{2+} with the protein solution: 0.17 s (spectrum B) and 0.33 s (spectrum C). Instrument settings are equivalent with those described in Figure 3.4 except T = 11.3 K. File name: "93au03a (A), 93au03d (B), and 93au03e (C)"

Figure 3.30. Evidence of the redox property of apoferritin. Conditions:2 [Mops] = 0.10 M, [apoferritin] = 1.0 mM subunit, [glucose] = 61.5 mM, [glucose oxidase] = 0.72 mg/ml, [catalase] = 0.75 mg/ml, [Fe^{3+}] = 0 for spectrum A and 0.5 mM for spectrum B. Instrument settings: see Figure 3.4, T = 10 K. File name: "93my28a (A) & 93my28b (B)"

the iron oxidation by apoferritin progressed within 5 minutes and the Fe^{3+} EPR signal didn't significantly decline with time under the experimental conditions. The g'= 4.3 signal in the control experiments devoid of Fe^{2+} (Fig. 3.30, spectrum B) or of apoferritin (data not shown) may be from impurity in the reagents or from a small amount of residual Fe^{3+} in the apoprotein. Spin quantitation of the EPR signal showed that only 0.15 Fe^{3+}/protein molecule was formed. The EPR line shape of the g'= 4.3 signals formed during iron oxidation by O_2 and by apoferritin are compared in Fig. 3.31.

EPR spectra of Iron Oxidation in rLF, rHF and Site-directed Mutants

Figure 3.32 shows the g' = 4.3 and g' = 1.87 signals formed during iron oxidation in mutants 222 (ferroxidase site mutated) and S1 (ferroxidase and nucleation sites mutated). A strong signal from the Fe^{3+}-protein complex (g' = 4.3) was observed in both instances. As a much stronger mixed-valence signal was observed in mutant 222 compared to the one in S1, the Fe^{2+}-Fe^{3+} species may be related to the nucleation sites. If so, there should be more than one kind of binding sites for the mixed-valence complex, since mutation of the nucleation site does not completely eliminate the signal. A similar experiment with mutant A2 in which only the nucleation site is altered will need to be done to test this postulate. Both the Fe^{3+}-protein complex

and the mixed-valence species are formed in rHF and in rLF (Fig. 3.33), indicating that the two iron intermediate species are not subunit-specific.

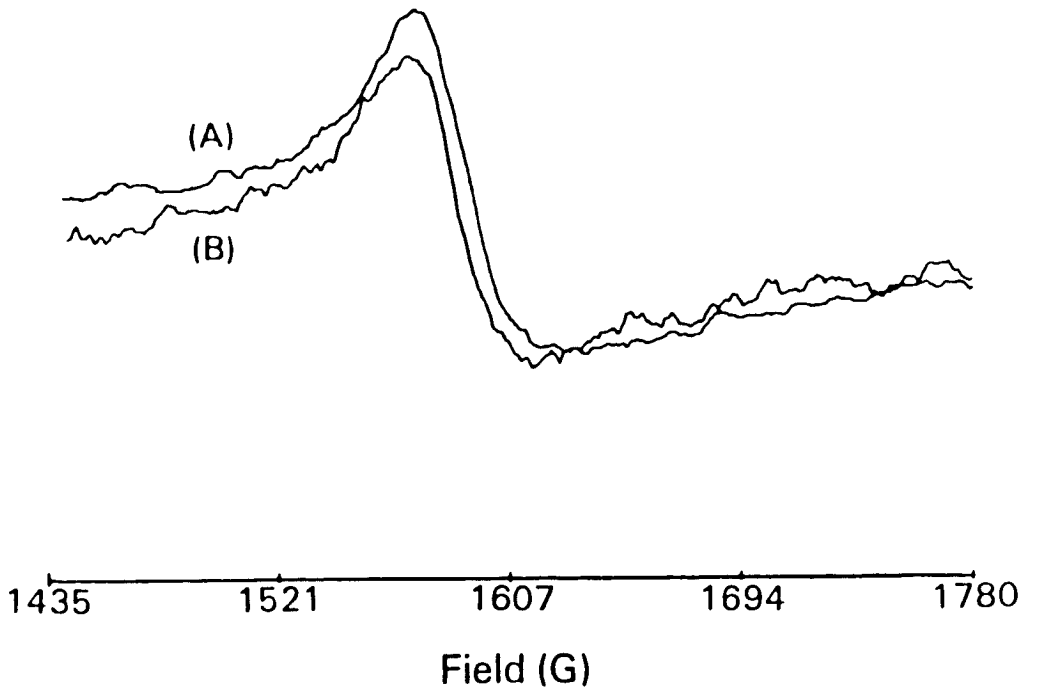

Figure 3.31. Comparison of the line shape and linewidth of the g′= 4.3 monomeric Fe^{3+}-protein signal formed during iron oxidation by dioxygen (spectrum A) and by apoferritin (spectrum B). Conditions: (A) [Mops] = 0.10 M, [apoferritin] = 0.1 mM, $[Fe^{2+}]_0$ = 0.4 mM, $[O_2]_0$ = 0.25 mM; (B) [Mops] = 0.10 M, [apoferritin] = 0.1 mM subunit, [glucose] = 61.5 mM, [glucose oxidase] = 0.72 mg/ml, [catalase] = 0.75 mg/ml, $[Fe^{3+}]$ = 0.5 mM. Instrument settings: see Figure 3.4, T = 10 K. File name: "93ja29e1 (A) & 93my28b (B)"

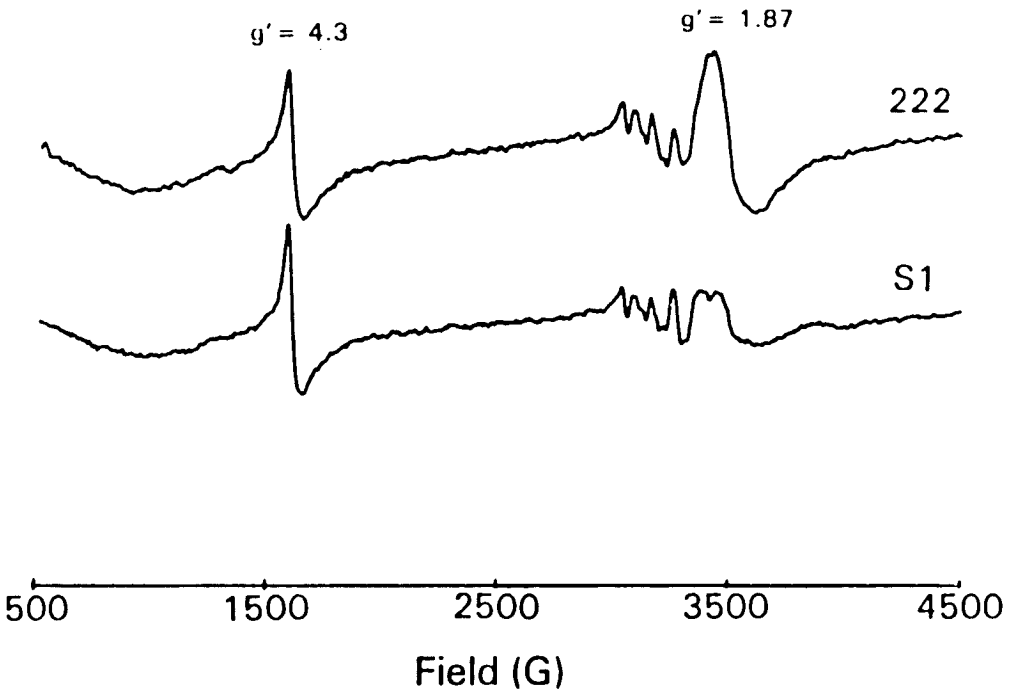

Figure 3.32. EPR spectra of mutants 222 and S1 containing 0.5 Fe^{3+} and 5 Fe^{2+} per subunit. Conditions: 0.5 mM apoferritin in 0.1 M Hepes and 0.1 M NaCl, pH 7.1. EPR parameters: SR = 4000, MA = 10, RG = 4000, MP = 10, MF = 9.36, TC = 1 s, and T = 7.5 K. File name: "mut2221 & muts1"

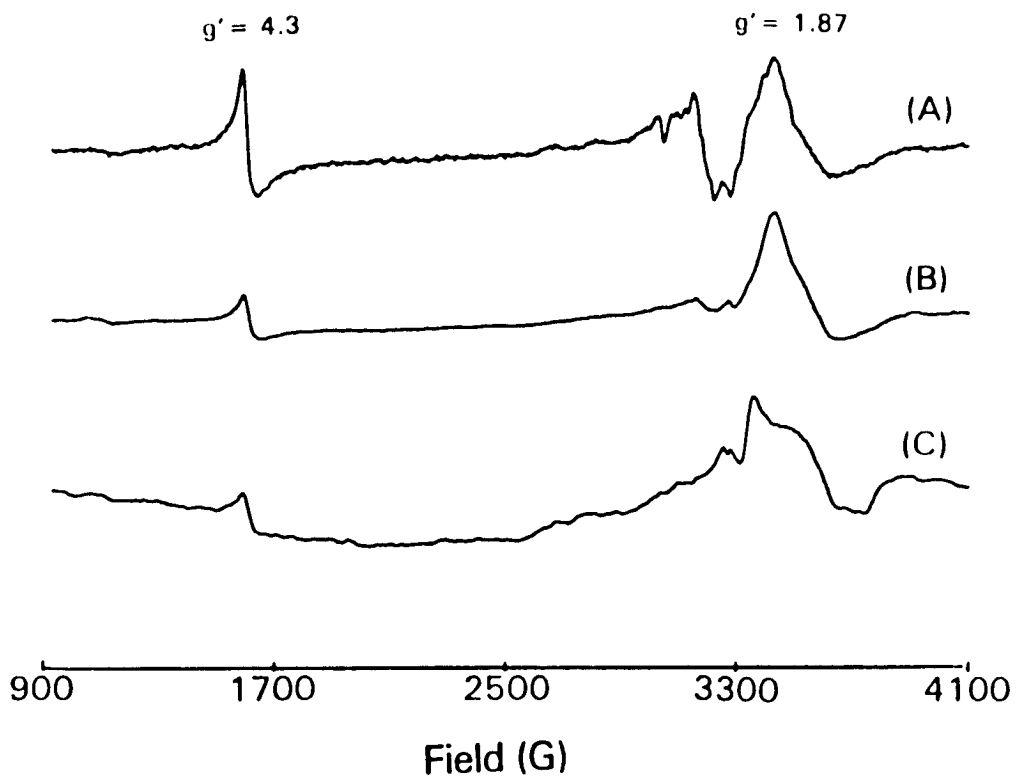

Figure 3.33. EPR spectra of rHF (A & B) and rLF (C) containing 0.25 Fe^{3+} and 2.5 Fe^{2+} per subunit . Conditions: 0.5 mM apoferritin in 0.1 M Hepes and 0.1 M NaCl, pH 7.1. EPR parameters: SR = 4000, MA = 10, RG = 6300 (A), 500 (B) and 2000 (C), MP = 1 (A), 200 (B & C), MF = 9.36, TC = 3 s, and T = 10 K. File name: "mrhf3 (A), mrhf3a (B), and mix3 (C)"

Discussion

EPR-active species (Fig. 3.4), including the solitary high spin Fe^{3+} ion bound to apoferritin (g'= 4.3), the dimeric Fe^{2+}-Fe^{3+} (g'= 1.87), as well as the organic radical ($g_{\perp}$ = 2.0033, $g_{\parallel}$ = 2.042), are three intermediates produced during the iron oxidative deposition in apoferritin. A binding site for monomeric Fe^{3+} on the L-subunit of horse spleen apoferritin has been found previously, which probably involves a mixture of oxygen and nitrogen donor ligands (Hanna et al., 1991; Gerfen et al., 1991). The observation of a monomeric Fe^{3+}-protein signal at g' = 4.3 on the recombinant H-chain ferritin indicates a similar Fe^{3+} binding site on the H-subunit of ferritin. Due to the rapid formation of iron clusters, the EPR detectable Fe^{3+}-protein complexes only account for a percentage of the total Fe^{3+} present in ferritin, depending on the Fe^{3+} to protein ratio. For example, around 20 % of the total iron is EPR detectable at Fe^{3+}/subunit = 0.5 (Rosenberg & Chasteen, 1982). Previous studies suggested that the g'= 1.87 signal was a transient species observed only in the presence of excess Fe^{2+} (Chasteen et al., 1985).

The radical II signal produced during iron oxidation and deposition has been studied previously. This signal may arise from more than one radical species since it decays with time in three phases (Grady et al., 1989). The lineshape of the radical II signal also changes somewhat

with reaction time (data not shown), and better resolution is observed at longer reaction time (Barrett & Chasteen, to be published). Radical II may be a tyrosine-derived radical (Barrett & Chasteen, to be published). This tyrosine radical may be formed by interaction between a tyrosine residue on the apoferritin shell and the hydroxyl radical generated by the Fenton reaction.

Under aerobic conditions, the time profile of the g′= 4.3 signal amplitude depends markedly on the initial Fe^{2+} concentration (Fig. 3.17). It is clear, however, that the onset of the g′= 4.3 signal occurred within milliseconds after initiation of iron oxidation, followed by slow growth (Fig. 3.17, curve B, C) or decline (curve A) in the signal intensities. The initial burst in the intensity of the monomeric Fe^{3+}-complex implies that all the Fe^{3+} oxidized at the very beginning of the reaction is in the form of the isolated Fe^{3+}-protein complex, in agreement with previously reported results (Rosenberg & Chasteen, 1982).

The observations that the maximum g′ = 4.3 signal amplitude decreased with increasing initial Fe^{2+} concentration, and that the presence of a large excess of Fe^{2+} led to decay of the EPR intensity immediately after the maximum point demonstrates that Fe^{2+} in solution interacts with the Fe^{3+}-protein complex, so that the monomeric Fe^{3+}-protein signal is unable to reach its full intensity. On the other hand, when there was no excess Fe^{2+} present in solution, the EPR signal continued to increase up to a

period of 60 seconds (Fig. 3.17, curve C), at which time all the Fe^{2+} has been oxidized to Fe^{3+} (Fig. 3.28, I, curve A). The largest spin concentration at $[Fe^{2+}]_0$ = 0.40 mM accounts for about 30 % of the total Fe^{3+} in the protein.

Under strictly anaerobic conditions, the interaction of ferrous ion with the solitary Fe^{3+}-protein complex was confirmed upon introduction of Fe^{2+} into a Fe^{3+}-apoferritin sample (Fig. 3.29). It was evident that the significant attenuation of the g′= 4.3 signal was directly caused by the advent of the g′= 1.87 signal and this interchange occurred in less than a second (Fig. 3.29). Spin quantitations indicate a simple 1:1 stoichiometric relationship between the two species, demonstrating that in such a short time interval, the dimeric mixed-valence species at g′= 1.87 is directly formed from interaction of the Fe^{2+} with Fe^{3+}-protein complex which gives rise to the g′= 4.3 signal or the Fe^{3+} in the Fe^{2+}-Fe^{3+} species is derived from the Fe^{3+}-protein complex. However, previous studies have shown that at a longer time interval of around 10 minutes, the increase in the spin concentration of the S = 1/2 dimer is much larger than the corresponding decrease in those of the S = 5/2 monomer (Hanna et al., 1991). In this instance, some of the mixed-valence species was probably formed from Fe^{2+} binding at or near the monomeric Fe^{3+} binding site or Fe^{3+} migrating to the binding sites of Fe^{2+}, while others may be produced by Fe^{2+} coupling to the Fe^{3+} located on the surface of Fe^{3+} clusters. These results reveal that interactions

between the monomeric and the dimeric species occur immediately after the onset of reaction, and the remaining Fe^{2+} then gradually interact with other Fe^{3+} species such as the Fe^{3+}-Fe^{3+} dimer or Fe^{3+} cluster. Electron transfer between the ferrous and ferric ions in ferritin has already been demonstrated by Mössbauer spectroscopy (Jacobs et al., 1989).

The radical II signal observed in this work has an apparent g factor of g = 2.0084 (Fig. 3.5, spectrum B) and exhibits a triplet hyperfine splitting. The line shape of radical II is very similar to that of the radical produced during the reaction of H_2O_2 with Fe^{2+}-protein (Fig. 3.7, spectrum B) where Fenton reaction occurs and thus the observed radical is probably induced by the hydroxyl radical. The hydroxyl radical has been detected by EPR spin-trapping during reaction of ferrous ion with hydrogen peroxide (Yamazaki & Piette, 1991). The nature of this protein-derived radical II has been suggested to be a tyrosyl radical (Barrett & Chasteen, to be published), based on the line shape and g factors of the reported tyrosyl radical from other protein systems (Hoganson & Babcock, 1992; Barry et al., 1990; Bender et al., 1989). The temperature-dependent behavior of radical II is particularly fascinating (Fig. 3.11). It neither follows Curie's Law (Equation 3.3) nor the Curie-Weiss Law (Equation 3.9):

$$\text{EPR Intensity} = \text{Constant}/(T + \Delta) \qquad (3.9)$$

where Δ is also a constant. The temperature dependence experiments need to be repeated before further rationalization of the results is warranted.

Unlike radical II, the radical I signal or signals observed during ferritin reconstitution in Mops buffer by the fast-mixing freeze-quench method exhibited apparent axial symmetry with $g_{\parallel}$ = 2.0418 and $g_{\perp}$ = 2.0033 (Fig. 3.5, spectrum A). Radical I was formed at the onset of iron oxidation in apoferritin. The conclusion that more than one radical contributed to the signal in the radical I region was made based on the following observations: firstly, the initial burst of the signal was followed by a rapid decay and then a slow decaying away (Fig. 3.19), indicating that some radicals decayed faster than others. Secondly, in the O_2 and temperature dependence experiments, two samples were prepared at initial oxygen concentrations of 0.25 mM and 1.27 mM. The difference in EPR intensities of these two samples at 8.3 K (Fig. 3.12, spectrum A and E) was disproportionately larger than that at 77 K, demonstrating that some of the radical signal at g = 2.0033 was not EPR detectable at higher temperature.

The possibility that radical I was the superoxide radical was ruled out by comparing the g factors of this radical with that of the superoxide ion ($g_{\perp}$ = 2.0078, $g_{\parallel}$ = 2.11 or $g_{\perp}$ = 2.0011, $g_{\parallel}$ = 2.076) (Fig. 3.15, spectra A and B respectively). The g-factors of 2.01 and 2.11 are reported in the literature as the g values of a superoxide radical in

crown-ether and DMSO medium (Oldfield & Allerhand, 1975), while the g values of 2.0011 and 2.076 of the superoxide ion produced by reaction of H_2O_2 and $NaIO_4$ at pH 9.5 are consistent with previously reported results (Knowles et al., 1969). Moreover, the superoxide radical signal generated in the protein vicinity by the catalytic xanthine/O_2/xanthine oxidase system has a g-factor of $g_{\parallel} = 2.081$ and $g_{\perp} = 2.001$ (Knowles et al., 1969), which likewise is not close to the g factors of the radical I. On the other hand, radical I is not a hydroxyl-induced radical since the line shape of the hydroxyl-induced radical (Fig. 3.15 D) is markedly different from that of radical I.

The fact that the maximum intensity of the radical signal increases with increasing added Fe^{2+} (Fig. 3.19), and that, like the mixed-valence Fe^{2+}-Fe^{3+} species, part of the signal at g = 2.0033 is not detectable at higher temperature due to fast spin relaxation, suggest that radical I is probably closely associated with a ferrous or ferric ion. A normal magnetically dilute free radical would not exhibit the temperature-dependent behavior observed for radical I. Similar properties have been reported for other radicals in the vicinity of Fe^{2+}, for example, the ubisemiquinone radicals near Fe^{2+} in the bacterial photosynthetic reaction center (Butler et al., 1984).

Zn^{2+}, an inhibitor of iron(II) oxidation (Sun & Chasteen, 1992), blocks the initial burst of Fe^{3+}-protein complex formation (Fig. 3.21), presumably by binding at an

Fe^{2+} ferroxidase site located on the H-subunit and reducing the initial rate of iron oxidation (Fig. 3.24), or by direct binding to ligands at the monomeric Fe^{3+} binding site situated on the L-subunit near the 3-fold channels (Hanna et al., 1991; Wardeska et al., 1986; Stefanini et al., 1989). In the latter case, Zn^{2+} must bind weakly at the monomeric Fe^{3+} binding site, since the incoming Fe^{3+} gradually replaced Zn^{2+} and formed the g'= 4.3 signal (Fig. 3.21, B). In addition, Zn^{2+} may just bind somewhere between the ferroxidase site and the binding site of the Fe^{3+}-protein complex and therefore slow down the Fe^{3+} migration. Zn^{2+} also inhibits the initial formation of the mixed-valence Fe^{2+}-Fe^{3+} species (Fig. 3.22), probably by the same mechanism.

The effect of Zn^{2+} on the formation of the radical I signal is striking and significant (Fig. 3.23). The intensity of the radical I signal observed in the presence of Zn^{2+} was very small and did not change with reaction time. Moreover, this signal exhibited no axial symmetry in its EPR feature which was similar to the one observed in the sample of apoferritin (the control experiment) (Fig. 3.34, spectrum A). Therefore, the radical I signal with an axial symmetry, generated during iron oxidation, must be completely eliminated by the presence of 24 Zn^{2+} per apoferritin molecule. The Zn^{2+} inhibitionary effect on the formation of the radical II signal has also been studied previously (Barrett & Chasteen, to be published). A

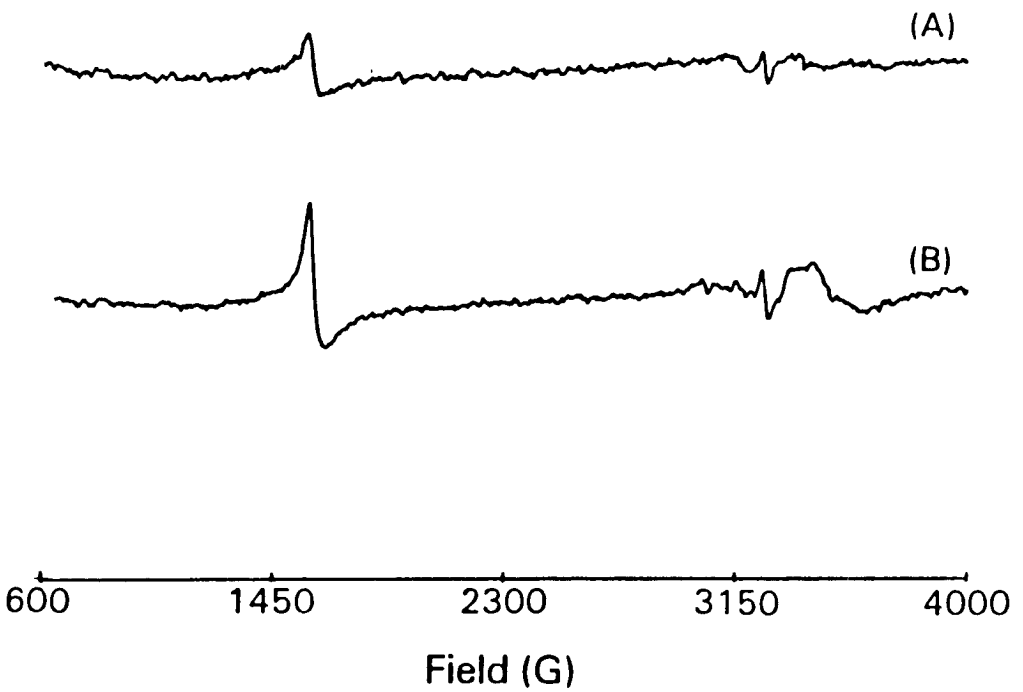

Figure 3.34. Comparison of the EPR spectra obtained in the control and Zn^{2+} inhibition experiments. Conditions: (A) [apoferritin] = 1.0 mM in 80 mM Mops, pH = 7.1; (B) [Mops] = 80 mM, [apoferritin] = 1.0 mM, pH = 7.1, reaction temperature = 23 ^{0}C, $[Fe^{2+}]_0$ = 2.0 mM, $[Zn^{2+}]$ = 1.0 mM. EPR parameters are as described in Figure 3.4. File name: "93ja29l1 (A) & 93ju17h1 (B)"

possible explanation for the inhibition effect of Zn^{2+} on the formation of radical I is that Zn^{2+} is bound directly to the ligand which is a precursor of the organic radical so that this amino acid residue is unable to interact with the oxygen-derived radical formed during iron oxidation.

The present work failed to identify the nature and location of this amino acid on the protein shell responsible for the radical I signal. X-ray crystallographic studies have revealed several Zn^{2+} binding sites on horse spleen apoferritin (Harrison et al., 1985; 1986). There are two Zn^{2+} binding sites on the protein shell, which may be possible locations of radical I. One is the ferroxidase site located on the H-subunit including one histidine and two glutamates residues as ligands. The other site (Asp-38, Glu-45 and Cys-46) is situated inside the protein shell near the 2-fold axis. To date, no histidine-centered protein radical has been reported. However, the EPR feature and the g-factors of $g_{\parallel}$ = 2.038 and $g_{\perp}$ = 2.005 of the compound I radical on cytochrome c peroxidase are very similar to those of the radical I signal (Hori & Yonetani, 1985; Hoffman et al., 1981). In addition, the temperature-dependent properties of the compound I radical (Figure 2 in Scholes et al., 1989), located in the vicinity of heme iron, are also similar to those of the radical I reported here (Fig. 3.6). The compound I radical has been previously suggested as a sulfur-centered species (Hoffman et al., 1981) but has been recently identified as a tryptophan-centered radical

(Scholes et al., 1989; Fishel et al., 1991). Thus, it is possible that tryptophan may directly participate in the formation of radical I, even though no tryptophan-related Zn^{2+} binding sites have been observed so far. Trp-93 (human liver apoferritin H-chain sequence) is conserved among ferritins of different sources. It is located close to the outer surface and between the loop and the four helices bundle on the three-dimensional structure of apoferritin. Like the indole ring of tryptophan, the imidazole ring of histidine is also a candidate for the site of the axially-symmetric radical I signal and the histidine residue at the ferroxidase site of the H-subunit is one of the possible locations for forming such a radical.

The addition of one Tb^{3+} per subunit reduced the intensity of the g'= 4.3 signal by a factor of 0.2 - 0.3 (Fig. 3.26), consistent with the previously reported result (Rosenberg & Chasteen, 1982). Thus, Tb^{3+} must bind at or near the sites where the monomeric Fe^{3+}-protein complex forms. In addition, the dramatic inhibition effect of Tb^{3+} on the formation of the mixed-valence species (Hanna et al., 1991) has shown that Tb^{3+} also binds to the Fe^{2+}-Fe^{3+} binding site. The effect of Tb^{3+} on the rate of iron oxidation, however, is insignificant (Fig. 3.28). These results demonstrate that the Fe^{3+} binding sites as well as the dimeric Fe^{2+}-Fe^{3+} binding sites from which the g'= 4.3 signal and the g'= 1.87 signal arise, are away from the ferroxidase sites since Tb^{3+} does little to inhibit Fe^{2+} oxidation (Fig.

3.28). Further, the ferroxidase sites in horse spleen ferritin should have low affinity toward Tb^{3+} compared to other Tb^{3+} binding sites since 24 Tb^{3+} per protein molecule were employed in the Tb^{3+} inhibition of iron(II) oxidation experiment. The location of the EPR-active Fe^{3+} monomer binding site in horse spleen ferritin can be postulated to be inside the protein shell and near the 3-fold channel based on the following observations: (1) one possible Tb^{3+} binding site located inside the protein shell near the 3-fold channel of horse spleen ferritin involves His-132 and Asp-135′ as ligands (Harrison et al., 1985); (2) studies of the ligand environment of the vanadyl complex of apoferritin with ESEEM have revealed a nitrogen donor residue as a ligand of the monomeric Fe^{3+}-protein complex (Gerfen et al., 1991); (3) Tb^{3+} is a competitive inhibitor of Fe^{3+}-protein formation.

Competitive binding experiments with Tb^{3+} resulted in only 40 % reduction in the intensity of the radical II signal (Fig. 3.27), showing that Tb^{3+} may not bind at or near the specific amino acid residues which are the location of the radical II.

There are six redox centers per apoferritin molecule and the redox properties of apoferritin have been investigated previously (Watt et al., 1992). The g′= 4.3 signal observed in this work under strictly anaerobic conditions is not as strong as the one reported previously at similar apoferritin concentrations (see Results). This

may be due to trace amounts of thioglyclic acid present in our sample. Some of the redox centers, therefore, are in reducing states. The line-shape and linewidth of the g'= 4.3 signal formed are similar to that of the common g'= 4.3 signal produced during iron oxidation with dioxygen (Fig. 3.31), indicating similar or equivalent binding sites for the monomeric Fe^{3+}.

In summary, the Fe^{3+}-protein monomer detected by EPR spectroscopy is an intermediate product of the iron oxidation occurring on the ferroxidase sites of naturally developed ferritins. However, the ferroxidase site is not crucial in the formation of the Fe^{3+}-apoferritin complex since this monomer was observed during iron oxidation in both mutant 222 and rLF, which are devoid of the ferroxidase sites. It could be speculated that there is more than one pathway leading from the Fe^{2+} oxidation sites on the protein shell to the Fe^{3+} mineralization sites in the interior of the ferritin cavity since the EPR-observable Fe^{3+}-protein complex accounts for only a small fraction of total oxidized iron. When all the isolated Fe^{3+} binding sites are occupied by Fe^{3+}, the incoming Fe^{3+} could, therefore, travel to the interior of the protein cavity by an alternative mechanism. For instance, an incoming Fe^{3+} could be coupled to the Fe^{3+}-protein complex and then the resultant Fe^{3+}-Fe^{3+} dimer migrate to the nucleation sites followed by Fe^{3+} hydrolysis and polymerization. Subsequently, the regenerated Fe^{3+} binding site could accept another incoming Fe^{3+}, and so

forth.

At least two kinds of free radicals are produced during iron oxidation in apoferritin. Radical I is closely associated with a ferric or ferrous ion center and is probably either a histidine-centered protein radical or a tryptophan-centered radical, while radical II, the more stable radical, is formed from interaction of the protein shell with the hydroxyl radical generated in the Fenton reaction. This radical may be a tyrosyl radical.

SUGGESTIONS FOR FUTURE WORK

Kinetic Studies of Recombinant Apoferritins

Recently, a series of apoferritins containing different compositions of H-chain and H-chain mutant which lacks the ferroxidase site as well as an apoferritin sample containing 29.5 % H subunit and 70.5 % L subunit have become available. Kinetic studies of iron(II) oxidation in these reconstructed proteins need to be performed. Initial rate of O_2 consumption versus H-chain % for the recombinant apoferritin containing H-chain and H-chain mutant can then be plotted. Comparison of the obtained result with Figure 2.4 in which the recombinant proteins are mixtures of varying amounts of H and L subunits would provide us with information about whether the H chain without the ferroxidase site can function as the L chain in the process of iron(II) uptake in ferritin. Kinetic studies of iron(II) oxidation in the recombinant apoferritin of 29.5 % H and 70.5 % L subunits also need to be performed and k_{cat} and K_m calculated. Based on the results of Figure 2.4, the k_{cat} and K_m obtained can be expected to be close to those of Fe^{2+} oxidation in rHF.

Identification of Radical I

Site-directed mutagenesis: As suggested in the Discussion of Chapter III, radical I might arise from a well-conserved amino acid residue, the tryptophan-93. This

hypothesis can be directly tested by site-directed mutation of the Trp-93 of human liver apoferritin. In addition, mutation of Cys-90 which is in the vicinity of Trp-93 should help to identify the nature of the radical. Since the radical I EPR signal is almost completely eliminated in the presence of 24 Zn^{2+} per protein molecule, it can be speculated that one or more of the Zn^{2+} binding sites may be the location of the radical I. His-65 at the ferroxidase site as well as His-118 and His-128 which are the Fe^{2+} binding sites should also be tested as alternative locations of the radical I.

Electron-nuclear Double Resonance(ENDOR) Spectroscopy: Hyperfine structure of a protein-centered radical is rarely resolved in an EPR spectrum due to the relative immobilization of the paramagnetic center by the large protein molecule. It is therefore difficult to identify the nature of a radical signal in EPR. Fortunately, this problem can be solved by ENDOR spectroscopy. ENDOR observes nuclei which are coupled to the electron spin, and therefore provides localized information. Thus, studies of the radical I with ENDOR will help to clarify the nature of the radical. For example, ENDOR can unequivocally distinguish whether the radical is carbon-centered, nitrogen-centered or sulfur-centered.

Zn^{2+} Titration: The number of the radical I per protein molecule may be obtained by titration of Zn^{2+}. A series of apoferritin samples containing 0 - 24 Zn^{2+}/protein should be

fast-mixed with a given amount of Fe^{2+} solution. A plot of the EPR amplitude of the radical I signal versus Zn^{2+}/protein may reveal the number of radical sites.

Tb^{3+} Inhibition: An attempt to perform the Tb^{3+} inhibition experiment on the fast-mixing freeze quench instrument using apoferritin containing 24 Tb^{3+}/protein and Fe^{2+} was unsuccessful. The crystals formed after freezing were too hard and too large to be packed into the EPR tube. However, the experiment may be done by changing the experimental conditions such as the ram velocity and Tb^{3+} concentration. Unlike Zn^{2+}, Tb^{3+} has little inhibitionary effect on the initial rate of Fe^{2+} oxidation in horse spleen apoferritin. Thus, the inhibition effect of Tb^{3+} on the formation of the radical I can be used to test if the radical I is formed at or near the ferroxidase site of apoferritin.

Investigation of the Mixed-valence Species

Figure 3.32 of Chapter III suggested that some of the mixed-valence Fe^{2+}-Fe^{3+} species may be formed at the nucleation site of the protein shell. Thus experiment should be performed with mutant A2 in which the nucleation site is mutated to test if the hypothesis is valid. Additionally, mutant 206 in which the carboxyl residues in the three-fold channel have been varied can be used to examine if these residues inside the 3-fold channel are alternative locations of the mixed-valence species.

REFERENCES

Adelman, T. G., Arosio, P. and Drysdale, J. (1975) *Biochem. Biophys. Res. Commun.* **63**, 1056-1062.

Arosio, P., Adelman, T. G., and Drysdale, J. W. (1978) *J. Biol. Chem.* **253**, 4451-4458.

Artymiuk, P. J., Bauminger, E. R., Harrison, P. M., Lawson, D. M., Nowik, I., Treffry, A. and Yewdall, S. J. (1991) in *Iron Biominerals* (R. Frankel and R. P. Blakemore, eds.), pp 269 Plenum Press, NY.

Bakker, G. R. and Boyer, R. F. (1986) *J. Biol. Chem.* **261**, 13182-13185.

Ballou, D. P. and Palmer, G. A. (1974) *Anal. Chem.* **46**, 1248-1253.

Barry B. A. El-Deeb, M. K., Sandusky P. O., and Babcock, G. T. (1990) *J. Biol. Chem.* **265**, 20139-20143.

Bauminger, E. R., Harrison, P. M., Nowik, I., and Treffry, A. (1989) *Biochemistry* **28**, 5486-5493.

Bauminger, E. R., Harrison, P. M., Hechel, D., Nowik, I. and Treffry A. (1991) *Biochim. Biophys. Acta* **1118**, 48-58.

Bender, C. J., Sahlin, M., Babcock, G. T., Barry, B. A., Chandrashekar, T. K., Salowe, S. P., Stubbe, J., Lindstrom, B., Peterson, L., Ehrenberg, A., and Sjoberg, B. M. (1989) *J. Am. Chem. Soc.* **111**, 8076-8083.

Borggaard, O. K. (1972) *Acta Chem. Scand.* **26**, 393-414.

Bremmer, M. C., Murray, C. J., and Klinman, J. P. (1989) *Biochemistry* **28**, 4656-4664.

Bryce, C. F. A. and Crichton, R. R. (1973) *Biochem. J.* **133**, 301-309.

Burkitt, M. J., and Gilbert, B. C., (1991) *Free Rad. Res. Comms.* **14**, 107-123.

Butler, W. F., Calvo, R., Fredkin, D. R., Isaacson, R. A., Okamura, M. Y., and Feher, G. (1984) *Biophys. J.* **45**, 947-973.

Chasteen, N. D. and Theil, E. C. (1982), *J. Biol. Chem.* **257**, 7672-7677.

Chasteen, N. D., Antanaitis, B. C. and Aisen, P. (1985) *J. Biol. Chem.* **260**, 2926-2929.

Cheng, Y. and Chasteen, N. D. (1990) *Biochemistry* **30**, 2947-2953.

Clegg, G. A., Fitton, J. E., Harrison, P. M. and Treffry, A. (1980) *Prog. Biophys. Molec. Biol.* **36**, 001-034.

Crichton, R. R., Roman, F. and Roland, F. (1980) *J. Inorg. Biochem.* **13**, 305-316.

Crichton, R. R. & Roman, F. (1978) *J. Mol. Catal.* **4**, 75-82.

Crichton, R. R. (1979) in *Oxygen Free Radicals and Tissue Damage,* pp. 57-76, Excerpta Medica, Amsterdam

Dallman, P. R., (1974) in *Iron and Biochemistry in Medicine*, Jacobs, A. and Worwood, M. eds., pp 375-437, New York: Academic Press.

de Silva, D., Miller, D. M., Reif, D. W., and Aust, S. D. (1992) *Arch. Biochem. Biophys.* **293**, 409-415.

Eigen, M. and Wilkins, R. A. (1965) *Adv. Chem. Ser.* **49**, 55-80.

Fishel, L. A., Farnum, M. F., Mauro, J. M., Miller, M. A., Kraut, J., Liu, Y., Tan, X., and Scholes, C. P. (1991) *Biochemistry* **30**, 1986-1996.

Ford, G. C., Harrison, P. M., Rice, D. W., Smith, J. M. A., Treffry, A., White, J. L., and Yariv, J. (1984) *Phil. Trans. R. Soc. Lond.* **304**, 551-565.

Gerfen, G. J., Hanna, P. M., Chasteen, N. D., and Singel, D. J. (1991) *J. Am. Chem. Soc.* **113**, 9513-9519.

Grady, J. K., Chen, Y., Chasteen, N. D., and Harris, D. C.(1989) *J. Biol. Chem.* **264**, 20224-20229.

Grady, J. K. and Chasteen, N. D. (1991) in *Iron Biominerals* (Frankel, R. B. and Blakemore, R. P. eds.) pp. 315-323, Plenum Press, New York

Granick, S. (1946) *Chem. Rev.* **38**, 379-403.

Hanna, P. M., Chasteen, N. D., Rottman, G. A., & Aisen, P. (1991) *Biochemistry* **30**, 9210-9216.

Hanna, P. M., Chen Y., and Chasteen, N. D. (1991) *J. Biol. Chem.* **266**, 886-893.

Harris, D. C. and Aisen, P. (1973) *Biochim. Biophys. Acta* **329**, 156-158.

Harrison, P. M., Fischback, F. A., Hoy, T. G., and Haggis, G. H., (1967) *Nature* **216**, 1188-1190.

Harrison, P. M. and Gregory, D. W. (1968) *Nature* **220**, 578-580.

Harrison, P. M., White, J. L., Smith, J. M. A., Farrants, G. W., Ford, G. C., Rice, D. W., Addison, J. M., and Treffry, A. (1985) in *Proteins of Iron Storage and Transport* (Spik, G., Montreuil, J., Crichton, R. R., and Mazurier, J., eds.) pp. 67-79, Elsevier Science Publishers, Amsterdam

Harrison, P. M., Treffry, A., and Lilley, T. H. (1986) *J. Inorg. Biochem.* **27**, 287-293.

Harrison, P. M., Ford, G. C., Rice, D. W., Smith, J. M. A., Treffry, A. and White, J. L. (1986) in *Frontiers in Bioinorganic Chemistry* (Xavier, A., ed.) pp 268, VCH, Verlagsgesellschaft, Weinheim, Germany.

Harrison, P. M. and Lilley, T. H. (1989) in *Iron Carrier and Iron Protein*, (Loehr, T. M., ed.) pp. 123-239, VCH, New York.

Harrison, P. M., Andrews, S. C., Artymiuk, P. J., Ford, G. C., Guest, J. R., Hirzmann, J., Lawson, D. M., Livingstone, J. C., Smith, J. M. A, Treffry, A., and Yewdall, S. J. (1991) *Adv. Inorg. Chem.* **36**, 449-486.

Heusterspreute, M. and Crichton, R. R. (1981) *FEBS Lett.* **129**, 322-327.

Hewkin, D. J. and Prince, R. H. (1970) *Coord. Chem. Rev.* **5**, 45-73.

Hoffman, B. M., Roberts, J. E., Kang, C. H., and Margoliash, E. (1981) *J. Biol. Chem.* **256**, 6556-6564.

Hoganson C. W. and Babcock, G. T. (1992) *Biochemistry* **31**, 11874-11880.

Hori, H., and Yonetani, M. (1985) *J. Biol. Chem.* **260**, 349-355.

Huang, H., Watt, R. D., Frankel, R. B., and Watt, G. D. (1993) *Biochemistry* **32**, 1681-1687.

Jacobs, D., Watt, G. D., Frankel, R. B., and Papaefthymiou, G. C. (1989) *Biochemistry* **28**, 9216-9221.

Judson, H. F. (1979) in *The Eighth Day of Creation*, Chapter 9 and 10, Simon & Schuster

Knowles, P. F., Gibson, J. F., Pick, F. M., and Bray, R. C. (1969) *Biochem. J.* **111**, 53-58.

Kurimura, Y., Ochiai, R., and Matsuura, N. (1968) *Bull. Chem. Soc. Jpn.* **41**, 2234-2239.

Kurimura, Y. and Kuriyama, H. (1969) *Bull. Chem. Soc. Jpn.* **42**, 2238-2242.

Lawson, D. M., Treffry, A., Artymiuk, P. J., Harrison, P. M., Yewdall, S. J., Luzzago, A., Cesareni, G., Levi, S., & Arosio, P. (1989) *FEBS Lett.* **254**, 207-210.

Lawson, D. M., Artymiuk, P. J., Yewdall, S. J., Smith, J. M. A., Livingstone, J. C., Treffry, A., Luzzago, A., Levi, S., Arosio, P., Cesareni, G., Thomas, C. D., Shaw, W. V., & Harrison, P. M. (1991) *Nature* **349**, 541-544.

Lee, M., Arosio, P., Levi, S., and Chasteen, N. D. (1993) *Biochemistry* submitted.

Leibold, E. A., and Guo, B. (1992) *Annu. Rev. Nutr.* **12**, 345-368.

Levi, S., Luzzago, A., Cesareni, G., Cozzi, A., Franceschinelli, F., Albertini, A., & Arosio, P. (1988) *J. Biol. Chem.* **263**, 18086-18092.

Levi, S., Salfeld, J., Franceschinelli, F., Cozzi, A., Dorner, M. H., & Arosio, P. (1989) *Biochemistry* **28**, 5179-5184.

Levi, S., Yewdall, S. J., Harrison, P. M., Santambrogio, P., Cozzi, A., Rovida, E., Albertini, A., & Arosio, P. (1992) *Biochem. J.* **288**, 591-596.

Levi, S., Cozzi, A., Santambrogio, P. and Arosio, P. (1991), "Study of the Sequences Involved in Ferritin Iron Incorporation", *10th International Conference on Iron and Iron Proteins*, Oxford, U.K., July 27 - July 31, paper # 015.

Loeb, L. A., James, E. A., Waltersdorph, A. M., Klebanoff, S. J., (1988) *Proc Natl Acad Sci USA*, 85, 3918-3922.

LaCross, D. M., Linder, M. C., (1980) *Biochem. Biophys. Acta* **633**, 45-55.

Macara, I. G., Hoy, T. G., & Harrison, P. M. (1972) *Biochem. J.* **126**, 151-156.

Macara, I. G., Hoy, T. G., & Harrison, P. M. (1973) *Biochem. J.* **135**, 343-348.

Martell, A. E. & Smith (1977) *Critical Stability Constants* Vol. 3, pp 1-171, Plenum Press, N.Y..

Mathews, C. K. and van Holde, K. E. (1990) in *Biochemistry*, p. 533, The Benjamin/Cummings Publishing Company, Inc.

McClune, G. J., Fee, J. A., McCluskey, G. A. and Groves, J. T. (1977) *J. Am. Chem. Soc.* **99**, 5220-5222.

Merritt, M. V. and Johnson, R. A. (1977) *J. Am. Chem. Soc.* **99**, 3713-3719.

Murray, M. T., White, K., and Munro, H. N. (1987) *Proc. Natl. Acad. Sci. USA* **84**, 7438-7442.

Naqui, A., Chance, B., and Cadenas, E. (1986), *Annu. Rev. Biochem.* **55**:137-166.

Ng, F. T. T. and Henry, P. M. (1980) *Can. J. Chem.* **58**, 1773-1779.

Oldfield, E., and Allerhand, A. (1975) *J. Am. Chem. Soc.* **97**, 224-226.

Rice, D. W., Ford, G. C., White, J. L., Smith, J. M. A., and Harrison, P. M. (1983) *Adv. Inorg. Biochem.* **5**, 39-50.

Roberts, D. V. (1977) *Enzyme Kinetics*, pp 65 & 83, Cambridge University Press, Cambridge.

Rohrer, J. S., Joo, M. S., Dartyge, E., Sayers, D. E., Fontaine, A., and Theil, E. C. (1987) *J. Biol. Chem.* **262**, 13385-13387.

Sada, E., Kumazawa H., and Machida, H. (1987) *Ind. Eng. Chem. Res.* **26**, 1468-1472.

Sawyer, D. T. and Valentine, J. S. (1991) *Acc. Chem. Res.* **14**, 393-400.

Scholes, C. P., Liu, Y., Fishel, L. F., Farnum, M. F., Mauro, J. M., and Kraut, J. (1989) *Isr. J. Chem.* **29**, 85-92.

Segel, I. H. (1975) *Enzyme Kinetics*, pp 884 & 941, Wiley-Interscience, New York.

Stefanini, S., Desideri, A., Vecchini, P., Drakenberg, T., and Chiancone, E. (1989) *Biochemistry* **28**, 378-382.

Stevens, P. W., Dodgson, J. B., and Engel, J. D. (1987) *Mol. Cell. Biol.* **7**, 1751-1757.

St. Pierre, T. G., Bell, S. H., Dickson, D. P. E., Mann, S., Webb, J., Moor, G. R., and Williams, R. J. (1986) *Biochem. Biophys. Acta* **870**, 127-134.

Subcommittee on Iron (1979) *Iron* pp. 1-38, 39-78, University Park Press, Baltimore.

Sun, S. & Chasteen, N. D. (1992) *J. Biol. Chem.* **267**, 25160-25166.

Theil, E. C.(1983) *Adv. Inorg. Biochem.* **5**, 1-38.

Theil, E. C. (1987) *Annu. Rev. Biochem.* **56**, 289-315.

Theil, E. C. (1989) *Adv. Enzymol. Relat. Areas Mol. Biol.* **63**, 421-449.

Thomas, C. D., Shaw, W. V., Lawson, D. M., Treffry, A., Artymiuk, P. J., and Harrison, P. M., (1988) *Biochem. Soc. Trans.* **16**, 838-839.

Towe, K. M., (1981) *J. Biol. Chem.* **256**, 9377-9378.

Treffry, A. Banyard, S. H., Hoare, R. J., and Harrison, P. M. (1977) in *Proteins of Iron Metabolism* (Brown, E. B., Aisen, P., Fielding, J., and Crichton, R. R., eds) pp. 3-11, Grune & Stratton, New York.

Trefrry, A., and Harrison, P. M. (1978) *Biochem. J.* **171**, 313-320.

Treffry, A., and Harrison, P. M. (1979) *Biochem. J.* **181**, 709-716.

Treffry, A. & Harrison, P. M. (1984) *J. Inorg. Biochem.* **21**, 9-20.

Treffry, A., Harrison, P. M., Cleton, M. I., de Bruijn, W. C., and Mann, S. (1987) *J. Inorg. Biochem.* **31**, 1-6.

Treffry, A., Hirzmann, J., Yewdall, S. J., & Harrison, P. M. (1992) *FEBS Lett.* **302**, 108-112.

Ulvik, R., (1982) *Biochem. Biophys. Acta* **715**, 42-51.

Voet, D., and Voet, J. G., (1990) in *Biochemistry*, Chapter 9, John Willey & Sons.

Wade, V. J., Levi, S., Arosio, P., Treffry, A., Harrison, P. M., & Mann, S. (1991) *J. Mol. Biol.* **221**, 1443-1452.

Wagstaff, M. M. and Jacobs, A. (1978) *Biochem. J.* **173**, 969-977.

Waldo, G. S., Ling, J., Sanders-Leoehr, J., and Theil, E. C. (1993) *Science* **259**, 796-798.

Walsh, C. (1979) *Enzymatic Reaction Mechanisms*, pp. 33, 79, W. H. Freeman, New York.

Wardeska, J. G., Viglione, B. and Chasteen, N. D. (1986) *J. Biol. Chem.* **261**, 6677-6683.

Watt, R. K., Frankel, R. B., and Watt, G. D. (1992) *Biochemistry* **31**, 9673-9679.

Wilkins, R. G. (1991) *Kinetics and Mechanisms of Reactions of Transition Metal Ions*, 2nd Ed, pp. 202, 393, VCH Publishers, Weinheim, Germany.

Williams, R. J. P. (1982) *FEBS Lett.* **140**, 3-10.

Williams, R. J. P. (1985) *Eur. J. Biochem.* **150**, 231-248.

Williams, R. J. P. (1989) *Biomineralization* (Mann, S., Webb, J., and Williams, R. J. P. eds), pp. 1 VCH Publ., Weinheim

Williams, R. J. P. (1990) *Biochem. Soc. Trans.* **18**, 689-705.

Worwood, M. (1990) *Blood Rev.* **4**, 259-269.

Xu, B. & Chasteen, N. D. (1991) *J. Biol. Chem.* **266**, 19965-19970.

Yamazaski, I. and Piette, L. H. (1991) *J. Am. Chem. Soc.* **113**, 7588-7593.

Yang, Cy. Y., Meagher, A., Huynh, B. H., Sayers, D. E., Theil, E. C. (1987) *Biochemistry* **26**, 497-503.

Yewdall, S. J., Lawson, D. M., Artymiuk, P. J., Treffry, A., Harrison, P. M., Luzzago, A., Cesaeni, G., Levi, S., and Arosio, P., (1990) *Biochem. Soc. Trans.* **18**, 658-659.

Zerner, B., Bond, R. P. M. and Bender, M. (1964) *J. Am. Chem. Soc.* **86**, 3674-3680.

APPENDIX I

MECHANISM I

Iron(II) Oxidation:

Fe^{2+} binding:

$$Fe^{2+} + P \underset{k_{-1}}{\overset{k_1}{\rightleftarrows}} Fe^{2+}\text{-}P \qquad (1)$$

Dioxygen binding and Fe^{2+} oxidation:

$$Fe^{2+}\text{-}P + O_2 \underset{k_{-2}}{\overset{k_2}{\rightleftarrows}} Fe^{2+}\text{-}P\text{-}O_2 \overset{k_3}{\rightarrow} Fe^{3+}\text{-}P + O_2^- \qquad (2)$$

Iron(III) core formation:

$$Fe^{3+}\text{-}P + 2H_2O \overset{k_4}{\rightarrow} FeOOH_{core} + P + 3H^+ \qquad (3)$$

Fate of superoxide:

$$2O_2^- + 2H^{2+} \overset{k_4}{\rightarrow} O_2 + H_2O_2 \qquad (4)$$

$$V = d[Fe^{2+}]/(2dt) = k_3[Fe^{2+}\text{-}P\text{-}O_2] \qquad (5)$$

$$d[Fe^{2+}\text{-}P]/dt = k_1[Fe^{2+}][P]-k_{-1}[Fe^{2+}\text{-}P]-$$
$$k_2[Fe^{2+}\text{-}P][O_2]+k_{-2}[Fe^{2+}P\text{-}O_2]=0 \qquad (6)$$

$$d[Fe^{2+}\text{-}P\text{-}O_2]/dt = k_2[Fe^{2+}\text{-}P][O_2]-k_{-2}[Fe^{2+}\text{-}P\text{-}O_2]$$
$$-k_3[Fe^{2+}\text{-}P\text{-}O_2]=0 \qquad (7)$$

from equation (6) and (7), we get

$$[Fe^{2+}\text{-}P] = \frac{k_1[Fe^{2+}][P]}{k_{-1}+(k_2-k_{-2}k_2/(k_3+k_{-2}))[O_2]} \quad (8)$$

$$[Fe^{2+}\text{-}P\text{-}O_2] = \frac{(k_1k_2/(k_3+k_{-2}))[Fe^{2+}][P][O_2]}{k_{-1} + (k_2-k_{-2}k_2/(k_3+k_{-2}))[O_2]} \quad (9)$$

The rate equation from the rate limiting equation (2) is given by

$$V = k_3[Fe^{2+}\text{-}P\text{-}O_2]/2 = \frac{(k_1k_2/(k_3+k_{-2}))[Fe^{2+}][P][O_2]/2}{k_{-1} + k_2-k_{-2}k_2/(k_3+k_{-2})[O_2]} \quad (10)$$

$$P_0 = P + [Fe^{2+}\text{-}P] + [Fe^{2+}\text{-}P\text{-}O_2]$$

$$= P + \frac{k_1[Fe^{2+}][P]}{k_{-1}+k_2-k_{-2}k_2/(k_3+k_{-2})[O_2]}$$

$$+ \frac{(k_1k_2/(k_3+k_{-2}))[Fe^{2+}][P][O_2]}{k_{-1} + k_2-k_{-2}k_2/(k_3+k_{-2})[O_2]} \quad (11)$$

$$P = \frac{P_0(k_{-1}+k_2-k_2k_{-2}/(k_3+k_{-2})[O_2])}{(k_{-1}+k_2-k_2k_{-2}/(k_3+k_{-2})[O_2])+k_1[Fe^{2+}]+(k_1k_2/(k_3+k_{-2}))[Fe^{2+}][O_2]} \quad (12)$$

$$V = \frac{(1/2)k_1k_2k_3[Fe^{2+}][P][O_2]}{k_{-1}(k_3+k_{-2})+k_2k_3[O_2]+k_1(k_3+k_{-2})[Fe^{2+}]+k_1k_2[Fe^{2+}][O_2]} \quad (13)$$

$$1/V = 2/P_0 \left\{\frac{1}{k_1[Fe^{2+}]} + \frac{k_3+k_{-2}}{k_2k_3[O_2]} + \frac{k_{-1}(k_3+k_{-2})}{k_1k_2[Fe^{2+}][O_2]} + \frac{1}{k_3}\right\} \quad (14)$$

Assuming $k_2 >> k_{-1}$, then

$$1/V = 2/P_0 \left\{ \frac{1}{k_1[Fe^{2+}]} + \frac{k_3+k_{-2}}{k_2k_3[O_2]} + \frac{1}{k_3} \right\} \quad (15)$$

which is the equation 1.8 in the main text. On the other hand, If $k_3 << k_{-2}$ is assumed, equation (8) & (9) will become the corresponding equations (16) & (17):

$$[Fe^{2+}\text{-}P] = K_1[Fe^{2+}][P] \tag{16}$$

$$[Fe^{2+}\text{-}P\text{-}O_2] = K_1K_2[Fe^{2+}][P][O_2] \tag{17}$$

$$V = (1/2)k_3[Fe^{2+}\text{-}P\text{-}O_2] = k_3K_1K_2[Fe^{2+}][P][O_2]/2 \tag{18}$$

$$[P_0] = [P] + [Fe^{2+}\text{-}P] + [Fe^{2+}\text{-}P\text{-}O_2]$$
$$= [P] + K_1[Fe^{2+}][P] + K_1K_2[Fe^{2+}][P][O_2]$$

$$[P] = \frac{[P_0]}{1 + K_1[Fe^{2+}] + K_1K_2[Fe^{2+}][O_2]} \tag{19}$$

Substituting equation (19) to (18), we obtain:

$$V = \frac{k_3K_1K_2[Fe^{2+}][O_2][P_0]/2}{1 + K_1[Fe^{2+}] + K_1K_2[Fe^{2+}][O_2]} \tag{20}$$

$$1/V = \frac{2}{K_1K_2P_0}\left\{\frac{1}{k_3[Fe^{2+}][O_2]} + \frac{K_1}{K_3[O_2]} + \frac{K_1K_2}{k_3}\right\} \tag{21}$$

Competitive Zn(II) Inhibition:

Zn(II) binding:

$$Zn^{2+}\text{-}P \overset{K_I}{\rightleftarrows} Zn^{2+} + P \tag{22}$$

From reactions (1)-(4) and (22) with the same steady-state approximation method, we obtain

$$[P_0] = [P] + [Fe^{2+}\text{-}P] + [Fe^{2+}\text{-}P\text{-}O_2] + [Zn^{2+}\text{-}P]$$

$$= P + \frac{k_1[Fe^{2+}][P]}{k_{-1}+(k_2-k_{-2}k_2/(k_3+k_{-2}))[O_2]}$$

$$+ \frac{(k_1k_2/(k_3+k_{-2}))[Fe^{2+}][P][O_2]}{k_{-1} + (k_2-k_{-2}k_2/(k_3+k_{-2}))[O_2]} + \frac{[Zn^{2+}][P]}{K_I} \qquad (23)$$

Let $k_2-k_{-2}k_2/(k_3+k_{-2}) = A$

$$P = \frac{P_0(k_{-1}+A[O_2])}{(k_{-1}+A[O_2])(1+1/K_I)[Zn^{2+}][P]+k_1[Fe^{2+}]+k_1k_2/(k_3+k_2)[Fe^{2+}][O_2]} \qquad (24)$$

$$V = k_3[Fe^{2+}\text{-}P\text{-}O_2]/2 = \frac{(k_1k_2k_3/(k_3+k_{-2}))[Fe^{2+}][P][O_2]/2}{k_{-1} + (k_2-k_{-2}k_2/(k_3+k_{-2}))[O_2]}$$

$$= \frac{(k_1k_2k_3/(k_3+k_{-2}))[Fe^{2+}][P_0][O_2]/2}{(k_{-1}+A[O_2])(1+1/K_I)[Zn^{2+}][P]+k_1[Fe^{2+}]+k_1k_2/(k_3+k_{-2})[Fe^{2+}][O_2]} \qquad (25)$$

$$1/V = 2/P_0\{(1+[Zn^{2+}]/K_I)/k_1[Fe^{2+}] + (k_3+k_{-2})/k_2k_3[O_2] + 1/k_3$$

$$+ k_{-1}(k_3+k_{-2})(1+[Zn^{2+}]/K_I)/k_1k_2[Fe^{2+}][O_2]\} \qquad (26)$$

If $k_2 >> k_{-1}$, we obtain the following equation for competitive Zn^{2+} inhibition:

$$1/V = 2/P_0\{(1+[Zn^{2+}]/K_I)/k_1[Fe^{2+}] + (k_3+k_{-2})/k_2k_3[O_2] + 1/k_3\} \qquad (27)$$

<u>Curve Fitting of the Initial Rate of Iron(II) Oxidation vs. $[Zn^{2+}]_0$</u>

The following rate equation (equation 34) as a

function of initial Zn^{2+} concentration is derived based on the competitive Zn^{2+} inhibition mechanism. Equations (28)-(30) are obtained from equations (6), (7) and (22) with an assumption of $k_2 >> k_{-1}$.

$$[Fe^{2+}\text{-}P] = k_1[Fe^{2+}][P]/k_2[O_2] + k_{-2}k_1[P][Fe^{2+}]/k_2k_3[O_2] \quad (28)$$

$$[Fe^{2+}\text{-}P\text{-}O_2] = k_1/k_3[Fe^{2+}][P] \quad (29)$$

$$[Zn^{2+}\text{-}P] = K[P][Zn^{2+}]_0/(1+K[P]) \quad (30)$$

where $K = 1/K_I$

$$\begin{aligned}[P] &= [P_0] - [Fe^{2+}\text{-}P] - [Fe^{2+}\text{-}P\text{-}O_2] - [Zn^{2+}\text{-}P] \\ &= [P_0] - k_1[Fe^{2+}][P]/k_2[O_2] - k_{-2}k_1[P][Fe^{2+}]/k_2k_3[O_2] \\ &\quad - k_1/k_3[Fe^{2+}][P] - K[P][Zn^{2+}]_0/(1+K[P]) \\ &= \{P_0(1+K[P]) - \alpha[Fe^{2+}][P](1+K[P]) - K[P][Zn^{2+}]\}/(1+K[P])\end{aligned} \quad (31)$$

where $\alpha = k_1/k_3 + (k_1/k_2 + k_{-2}k_1/k_2k_3)/[O_2]_0$

Rearranging equation (31), the following quadratic equation is obtained:

$$(K+\alpha K[Fe^{2+}])P^2 + (1+\alpha[Fe^{2+}] - P_0K + K[Zn^{2+}]_0)P - P_0 = 0 \quad (32)$$

$$P = (-b + (b^2 - 4ac)^{1/2})/2a \quad (33)$$

$$\begin{aligned}V &= d[Fe^{2+}]/(2dt) = k_3[Fe^{2+}\text{-}P\text{-}O_2]/2 = k_1[Fe^{2+}][P]/2 \\ &= k_1[Fe^{2+}](-b + (b^2 - 4ac)^{1/2}/4a\end{aligned} \quad (34)$$

where

$$a = (1 + \alpha[Fe^{2+}])/K_I$$

$$b = 1+\alpha[Fe^{2+}] + (-P_0 + [Zn^{2+}]_0)/K_I$$

$$c = -[P_0]$$

when $V = V_0$, the initial rate, $[Fe^{2+}] = [Fe^{2+}]_0$.

Non-competitive and Mixed-Inhibition by Zn^{2+}

The mechanism I for iron oxidation modified to include the noncompetitive and mixed inhibitions by Zn^{2+} are given below where the rate constants for the added elementary steps involving Zn^{2+} are designated by primes.

Zn^{2+} binding:
$$Zn^{2+}\text{-}P \overset{K_I}{\rightleftarrows} Zn^{2+} + P \qquad (35)$$

Fe^{2+} binding:
$$Fe^{2+} + P \underset{k_{-1}}{\overset{k_1}{\rightleftarrows}} Fe^{2+}\text{-}P \qquad (36)$$

$$Fe^{2+} + Zn^{2+}\text{-}P \underset{k_{-1}'}{\overset{k_1'}{\rightleftarrows}} Fe^{2+}\text{-}P\text{-}Zn^{2+} \qquad (37)$$

Dioxygen binding and Fe^{2+} oxidation:

$$Fe^{2+}\text{-}P + O_2 \underset{k_{-2}}{\overset{k_2}{\rightleftarrows}} Fe^{2+}(O_2)\text{-}P \overset{k_3}{\rightarrow} Fe^{3+}\text{-}P + O_2^- \qquad (38)$$

$$Fe^{2+}\text{-}P\text{-}Zn^{2+} + O_2 \underset{k_{-2}'}{\overset{k_2'}{\rightleftarrows}} Fe^{2+}(O_2)\text{-}P\text{-}Zn^{2+}$$

$$\overset{k_3'}{\rightarrow} Fe^{3+}\text{-}P\text{-}Zn^{2+} + O_2^- \qquad (39)$$

Iron(II) core formation:

$$Fe^{3+}\text{-}P + 2H_2O \overset{k_4}{\rightarrow} FeOOH_{core} + P + 3H^+ \qquad (40)$$

$$Fe^{3+}\text{-}P\text{-}Zn^{2+} + 2H_2O \xrightarrow{k_4'} FeOOH_{core} + Zn^{2+}\text{-}P + 3H^+ \quad (41)$$

Fate of superoxide:

$$2O_2^{\cdot-} + 2H^+ \xrightarrow{k_5} H_2O_2 + O_2 \quad (42)$$

The steady-state approximation is used to derive the various rate equations.

$$d[Fe^{2+}\text{-}P]/dt = k_1[P][Fe^{2+}] - k_{-1}[Fe^{2+}\text{-}P] - k_2[O_2][Fe^{2+}\text{-}P] - k_{-2}[Fe^{2+}(O_2)P] = 0 \quad (43)$$

$$d[Fe^{2+}\text{-}P\text{-}Zn^{2+}]/dt = k_1'[Zn^{2+}\text{-}P][Fe^{2+}] - k_{-1}'[Fe^{2+}\text{-}P\text{-}Zn^{2+}] - k_2'[Fe^{2+}\text{-}P\text{-}Zn^{2+}][O_2] + k_{-2}'[Fe^{2+}(O_2)\text{-}P\text{-}Zn^{2+}] = 0 \quad (44)$$

$$d[Fe^{2+}(O_2)\text{-}P]/dt = k_2[Fe^{2+}\text{-}P][O_2] - (k_{-2} + k_3)[Fe^{2+}(O_2)\text{-}P] = 0 \quad (45)$$

$$d[Fe^{2+}(O_2)\text{-}P\text{-}Zn^{2+}]/dt = k_2'[Fe^{2+}\text{-}P\text{-}Zn^{2+}][O_2] - (k_{-2}' + k_3')[Fe^{2+}(O_2)\text{-}P\text{-}Zn^{2+}] = 0 \quad (46)$$

From equations (43) & (45), we get

$$[Fe^{2+}(O_2)\text{-}P] = k_2[Fe^{2+}\text{-}P][O_2]/(k_{-2}+k_3) \qquad \text{let } k_3 << k_{-2}$$

$$\approx k_2[Fe^{2+}\text{-}P][O_2]/k_{-2} = K_1K_2[Fe^{2+}][P][O_2] \quad (47)$$

$$[Fe^{2+}\text{-}P] = K_1[Fe^{2+}][P] \quad (48)$$

where $K_1 = k_1/k_{-1}$, $K_2 = k_2/k_{-2}$.

Likewise, the following expressions are obtained from equations (44) & (46):

$$[Fe^{2+}(O_2)\text{-}P\text{-}Zn^{2+}] = K_1'K_2'[Fe^{2+}][P\text{-}Zn^{2+}][O_2] \quad (49)$$

$$[Fe^{2+}\text{-}P\text{-}Zn^{2+}] = K_1'[Fe^{2+}][P\text{-}Zn^{2+}] \quad (50)$$

where $K_1' = k_1'/k_{-1}'$, and $K_2' = k_2'/k_{-2}'$.

The rate expression from the rate limiting equations (38) and (39) is given by

$$\begin{aligned} V = d[Fe^{2+}]/2dt &= k_3[Fe^{2+}(O_2)\text{-}P]/2 \\ &\quad + k_3'[Fe^{2+}(O_2)\text{-}P\text{-}Zn^{2+}]/2 \\ &= k_3K_1K_2[Fe^{2+}][P][O_2] + k_3'K_1'K_2'[Fe^{2+}][P\text{-}Zn^{2+}][O_2] \end{aligned} \quad (51)$$

where V $(= d[O_2]/dt = (1/2)d[Fe^{2+}]/dt)$ is the net velocity for the reaction given by equation 2.1 of the main text.

If $K_1 = K_1'$ and $K_2 = K_2'$, then

$$V = (1/2)(k_3 + k_3'[Zn^{2+}]/K_1)K_1K_2[Fe^{2+}][P][O_2] \quad (52)$$

$$\begin{aligned} [P_0] &= [P] + [P\text{-}Zn^{2+}] + [Fe^{2+}\text{-}P] + [Fe^{2+}(O_2)\text{-}P] \\ &\quad + [Fe^{2+}\text{-}P\text{-}Zn^{2+}] + [Fe^{2+}(O_2)\text{-}P\text{-}Zn^{2+}] \end{aligned} \quad (53)$$

$$V = \frac{(1/2)(k_3 + k_3'[Zn^{2+}]/K_1)K_1K_2[Fe^{2+}][P_0][O_2]}{(1+[Zn^{2+}]/K_1) + (1+[Zn^{2+}]/K_1)(1+K_2[O_2])K_1[Fe^{2+}]} \quad (54)$$

$$1/V = (2/P_0K_1K_2)\left\{\frac{(1+[Zn^{2+}]/K_1)}{\alpha[Fe^{2+}]} + \frac{(1+[Zn^{2+}]/K_1)(1+K_2[O_2])K_1}{\alpha}\right\} \quad (55)$$

where $\alpha = (k_3 + k_3'[Zn^{2+}]/KI)[O_2]$.

When $[Zn^{2+}] = 0$, equation (55) reduces to:

$$1/V = \frac{2}{K_1K_2P_0}\left\{\frac{1}{k_3[Fe^{2+}][O_2]} + \frac{K_1}{K_3[O_2]} + \frac{K_1K_2}{k_3}\right\} \quad (56)$$

which is the same as equation (21).

In deriving the rate equation 2.3 in the main text for noncompetitive inhibition, several assumptions have been made in order to obtain a linear equation consistent with the observed data: (1) the binding of Zn^{2+} to protein does not affect the affinities of Fe^{2+} and O_2 binding to protein, *i.e.*, the equilibrium constants $K_1 = K_1'$ and $K_2 = K_2'$, (2) the rate constant of the one-electron transfer step is reduced by Zn^{2+} binding so that $k_3' < k_3$, (3) a preequilibrium condition exists for O_2 binding in equations 38 and 39, *i.e.* $k_3 << k_{-2}$, $k_3' << k_{-3}'$, and (4) the one-electron transfer reaction for oxidation of the first Fe^{3+} is rate-determining (steps 38 and 39). Under these assumptions, the same double-reciprocal rate equation (equation 2.3, main text) is obtained for both Mechanisms I and II except the factor of 2 is absent for Mechanism II. In deriving the rate equation for mixed inhibition (equation 2.4, main text), the first assumption is changed such that the equilibrium constants for Fe^{2+} and O_2 binding to the protein are altered upon Zn^{2+} binding, *i.e.* $K_1 \neq K_1'$ and $K_2 \neq K_2'$. The second through fourth assumptions are unchanged. The corresponding reciprocal rate equation for mixed

inhibition of Zn^{2+} can be described in the following equation:

$$1/V = 2/P_0[O_2]\cdot\left\{\frac{(1+[Zn^{2+}]/K_I)}{(A+B[Zn^{2+}]/K_I)[Fe^{2+}]} + \frac{C+D[Zn^{2+}]/K_I}{A+B[Zn^{2+}]/K_I}\right\} \quad (57)$$

where $A = k_3K_1K_2$, $B = k_3'K_1'K_2'$, $C = K_1(1 + K_2[O_2])$ and $D = (1 + K_2'[O_2])K_1'$.

Kinetic Parameters

The apparent values of $K_{m,Fe}$ and $K_{m,O2}$ obtained from the intercept of the abscissa of the 1/V versus $1/[Fe^{2+}]$ and 1/V versus $1/[O_2]$ plots of equation (14) are given by

$$K_{m,Fe} = \frac{k_2k_3[O_2] + k_{-1}k_3(k_3 + k_{-2})}{k_1k_2[O_2] + k_1(k_3 + k_{-2})} \longrightarrow \frac{k_3}{k_1} \quad (58)$$

at saturating O_2 levels, *i.e.* $[O_2] \longrightarrow \infty$, and

$$k_{m,O2} = \frac{(k_3 + k_{-2})k_1[Fe^{2+}] + k_{-1}k_3(k_3 + k_{-2})}{k_2k_1[Fe^{2+}] + k_3k_2} \longrightarrow \frac{k_1 + k_{-2}}{k_2} \quad (59)$$

at saturating Fe^{2+} levels, *i.e.* $[Fe^{3+}] \longrightarrow \infty$.

MECHANISM II

Iron(II) Oxidation:

Fe^{2+} binding:

$$Fe^{2+} + P \underset{k_{-1}}{\overset{k_1}{\rightleftarrows}} Fe^{2+}\text{-}P \qquad (60)$$

Dioxygen binding and 1st Fe^{2+} oxidation:

$$O_2 + Fe^{2+}\text{-}P \underset{k_{-2}}{\overset{k_2}{\rightleftarrows}} Fe^{2+}(O_2)P \overset{k_3}{\rightarrow} Fe^{3+}(O_2^{-})P \qquad (61)$$

2nd Fe^{2+} binding/oxidation:

$$Fe^{3+}(O_2^{-})P + Fe^{2+} \overset{k_4}{\rightarrow} Fe^{3+}(O_2^{=})Fe^{3+}\text{-}P$$

$$\overset{k_5,\ H_2O}{\text{-------}\rightarrow} Fe^{3+}(O^{=})Fe^{3+}\text{-}P + H_2O_2 \qquad (62)$$

Fe(III) core formation:

$$Fe^{3+}(O^{=})Fe^{3+}\text{-}P + 3H_2O$$

$$\overset{k_6}{\text{---}\rightarrow} 2FeOOH_{core} + P + 4H^{+} \qquad (63)$$

The following expressions are combined to obtain the rate equations for mechanism II:

$$d[Fe^{2+}\text{-}P]/dt = k_1[Fe^{2+}][P] - k_{-1}[Fe^{2+}\text{-}P] - k_2[Fe^{2+}\text{-}P][O_2] + k_{-2}[Fe^{2+}\text{-}P\text{-}O_2] = 0 \qquad (64)$$

$$d[Fe^{2+}\text{-}P\text{-}O_2]/dt = k_2[Fe^{2+}\text{-}P][O_2] - k_{-2}[Fe^{2+}\text{-}P\text{-}O_2] - k_3[Fe^{2+}\text{-}P\text{-}O_2] = 0 \qquad (65)$$

$$d[Fe^{3+}(O_2^{\cdot})P]/dt = k_3[Fe^{2+}\text{-}P\text{-}O_2] - k_4[Fe^{3+}(O_2^{\cdot})P][Fe^{2+}] = 0 \quad (66)$$

$$d[Fe^{3+}(O_2^{=})Fe^{3+}\text{-}P]/dt = k_4[Fe^{3+}(O_2^{\cdot})P][Fe^{2+}] - k_5[Fe^{3+}(O_2^{=})Fe^{3+}\text{-}P] = 0 \quad (67)$$

$$d[Fe^{3+}(O^{=})Fe^{3+}\text{-}P]/dt = k_5[Fe^{3+}(O_2^{=})Fe^{3+}\text{-}P] - k_6[Fe^{3+}(O^{=})Fe^{3+}\text{-}P] = 0 \quad (68)$$

From rate equation (64) and (65), we obtained

$$[Fe^{2+}\text{-}P] = \frac{k_1[Fe^{2+}][P]}{k_{-1}+(k_2-k_{-2}k_2/(k_3+k_{-2}))[O_2]} \quad (69)$$

$$[Fe^{2+}\text{-}P\text{-}O_2] = \frac{k_1k_2/(k_3+k_{-2})[Fe^{2+}][P][O_2]}{k_{-1} + (k_2-k_{-2}k_2/(k_3+k_{-2}))[O_2]} \quad (70)$$

Likewise, from equation (66), (67) and (68), we obtain:

$$[Fe^{3+}(O_2^{\cdot})\text{-}P] = k_3[Fe^{2+}\text{-}P\text{-}O_2]/(k_4[Fe^{2+}]) \quad (71)$$

$$[Fe^{3+}(O_2^{=})Fe^{3+}\text{-}P] = k_3[Fe^{2+}\text{-}P\text{-}O_2]/(k_5[Fe^{2+}]) \quad (72)$$

$$[Fe^{3+}(O^{=})Fe^{3+}\text{-}P] = k_3[Fe^{2+}\text{-}P\text{-}O_2]/(k_6[Fe^{2+}]) \quad (73)$$

Since k_4, k_5 and k_6 are much larger than k_3, which is the rate constant for the rate determining step, It is feasible that the concentrations of the three intermediates in equations (71) - (73) are negligible. Thus,

$$P_0 = P + [Fe^{2+}\text{-}P] + [Fe^{2+}\text{-}P\text{-}O_2]$$

$$= P + \frac{k_1[Fe^{2+}][P]}{k_{-1}+(k_2-k_{-2}k_2/(k_3+k_{-2}))[O_2]}$$

$$+ \frac{k_1k_2/(k_3+k_{-2})[Fe^{2+}][P][O_2]}{k_{-1} + (k_2-k_{-2}k_2/(k_3+k_{-2}))[O_2]} \quad (74)$$

$$P = \frac{P_0[k_{-1}+k_2-k_2k_{-2}/(k_3+k_{-2})[O_2]}{(k_{-1}+k_2-k_2k_{-2}/(k_3+k_{-2})[O_2])+k_1[Fe^{2+}]+k_1k_2/(k_3+k_{-2})[Fe^{2+}][O_2]} \quad (75)$$

$$V = k_3[Fe^{2+}-P-O_2]/2 = \frac{(k_1k_2/(k_3+k_{-2}))[Fe^{2+}][P][O_2]/2}{k_{-1} + (k_2-k_{-2}k_2/(k_3+k_{-2}))[O_2]}$$

$$= \frac{k_1k_2k_3[Fe^{2+}][P][O_2]/2}{k_{-1}(k_3+k_{-2})+k_2k_3[O_2]+k_1(k_3+k_{-2})[Fe^{2+}]+k_1k_2[Fe^{2+}][O_2]} \quad (76)$$

$$1/V = 2/P_0\{\frac{1}{k_1[Fe^{2+}]} + \frac{k_3+k_{-2}}{k_2k_3[O_2]} + \frac{k_{-1}(k_3+k_{-2})}{k_1k_2[Fe^{2+}][O_2]} + \frac{1}{k_3}\} \quad (77)$$

Assuming $k_2 >> k_{-1}$, then

$$1/V = 2/P_0 \{ \frac{1}{k_1[Fe^{2+}]} + \frac{k_3+k_{-2}}{k_2k_3[O_2]} + \frac{1}{k_3} \} \quad (78)$$

Equations (77) and (78) are exactly the same as Equations (14) and (15) in Mechanism I, respectively. On the other hand, if assumption of $k_2[O_2] >> k_{-1}$ is used, an alternative rate equation will be obtained from Mechanism II. The following equations elaborate these procedures: from equation (64), we obtain:

$$[Fe^{2+}-P] = \frac{k_1[Fe^{2+}][P] + k_{-2}[Fe^{2+}-P-O_2]}{k_{-1} + k_2[O_2]} \quad (79)$$

assuming that $k_2[O_2] >> k_{-1}$, then

$$[Fe^{2+}\text{-}P] = \frac{k_1[Fe^{2+}][P] + k_{-2}[Fe^{2+}P\text{-}O_2]}{k_2[O_2]} \quad (80)$$

The following expression for species $[Fe^{2+}P\text{-}O_2]$ can be derived from equation (65) & (80),

$$[Fe^{2+}P\text{-}O_2] = k_1/k_3\ [Fe^{2+}][P] \quad (81)$$

Substituting (81) into (80), we obtain:

$$[Fe^{2+}\text{-}P] = (k_3k_1 + k_1k_{-2})[Fe^{2+}][P]/k_2k_3[O_2] \quad (82)$$

Then, combining equation (66) & (81), we obtain:

$$[Fe^{3+}(O_2^-)P] = k_1[P]/k_4 \quad (83)$$

Likewise, from equation (67) & (83), equation (84) is derived:

$$[Fe^{3+}(O_2^{=})Fe^{3+}\text{-}P] = k_1[Fe^{2+}][P]/k_5 \quad (84)$$

$$P_0 = P + [Fe^{2+}\text{-}P] + [Fe^{2+}P\text{-}O_2] + [Fe^{3+}(O_2^-)P] + [Fe^{3+}(O_2^{=})Fe^{3+}\text{-}P]$$

$$= P + (k_3k_1 + k_1k_{-2})[Fe^{2+}][P]/k_2k_3[O_2] + (k_1/k_3)[Fe^{2+}][P] + k_1[P]/k_4 + k_1[Fe^{2+}][P]/k_5 \quad (85)$$

$$P = k_2k_3k_4k_5[O_2][P_0] \,/\, \{k_2k_3k_4k_5[O_2] + (k_3+k_2)k_1k_4k_5[Fe^{2+}] + k_1k_2k_4k_5[O_2]Fe^{2+}] + k_1k_2k_3k_5[O_2] + k_1k_2k_3k_4[Fe^{2+}][O_2]\} \quad (86)$$

$$V = k_3[Fe^{2+}\text{-}P\text{-}O_2]/2 \quad (87)$$

Combining equation (81) and (87), then

$$V = k_1[Fe^{2+}][P]/2 \qquad (88)$$

Substituting (86) into (88), we obtain

$$V = k_1k_2k_3k_4k_5[O_2][Fe^{2+}][P_0]/2\{k_2k_3k_4k_5[O_2]+(k_3+k_2)k_1k_4k_5[Fe^{2+}] + k_1k_2k_4k_5[O_2]Fe^{2+}]+k_1k_2k_3k_5[O_2]+k_1k_2k_3k_4[Fe^{2+}][O_2]\} \qquad (89)$$

$$1/V = 2/P_0\{ \frac{k_1+k_4}{k_1k_4[Fe^{2+}]} + \frac{k_3+k_{-2}}{k_2k_3[O_2]} + \frac{k_3+k_5}{k_3k_5} \} \qquad (90)$$

Equation (90) is the double-reciprocal equation 1.14 in Chapter I.

Competitive Zn^{2+} Inhibition

$$Zn^{2+} \text{ binding: } Zn^{2+}\text{-}P \overset{K_I}{\rightleftarrows} Zn^{2+} + P \qquad (91)$$

Combining reactions (60)-(63) in Mechanism II with reaction (90) and use the same steady-state approximation expressions of equations (64)-(68), the following expression for P_0 is obtained under assumption of k_4, k_5, and $k_6 >> k_3$. See derivations of equations (69)-(73).

$$P_0 = P + [Fe^{2+}\text{-}P] + [Fe^{2+}\text{-}P\text{-}O_2] + [Zn^{2+}\text{-}P]$$

$$= P + \frac{k_1[Fe^{2+}][P]}{k_{-1}+(k_2-k_{-2}k_2/(k_3+k_{-2}))[O_2]}$$

$$+ \frac{k_1k_2/(k_3+k_{-2})[Fe^{2+}][P][O_2]}{k_{-1} + (k_2-k_{-2}k_2/(k_3+k_{-2}))[O_2]} + \frac{[Zn^{2+}][P]}{K_I} \qquad (92)$$

Let $k_2-k_{-2}k_2/(k_3+k_{-2}) = A$

$$P = \frac{P_0(k_{-1}+A[O_2])}{(k_{-1}+A[O_2])(1+1/K_I)[Zn^{2+}][P]+k_1[Fe^{2+}]+k_1k_2/(k_3+k_2)[Fe^{2+}][O_2]} \qquad (93)$$

$$V = k_3[Fe^{2+}-P-O_2]/2 = \frac{k_1k_2k_3/(k_3+k_{-2})[Fe^{2+}][P][O_2]}{2(k_{-1} + (k_2-k_{-2}k_2/(k_3+k_{-2}))[O_2])}$$

$$= \frac{(k_1k_2k_3/(k_3+k_{-2}))[Fe^{2+}][P_0][O_2]/2}{(k_{-1}+A[O_2])(1+1/K_I)[Zn^{2+}][P]+k_1[Fe^{2+}]+k_1k_2/(k_3+k_2)[Fe^{2+}][O_2]} \qquad (94)$$

$$1/V = 2/P_0\{(1+[Zn^{2+}]/K_I)/k_1[Fe^{2+}] + (k_3+k_{-2})/k_2k_3[O_2] + 1/k_3$$
$$+ k_{-1}(k_3+k_{-2})(1+[Zn^{2+}]/K_I)/k_1k_2[Fe^{2+}][O_2]\} \qquad (95)$$

If $k_2>>k_{-1}$ is assumed, we will obtain the following equation for competitive Zn^{2+} inhibition:

$$1/V = 2/P_0\{(1+[Zn^{2+}]/K_I)/k_1[Fe^{2+}] + (k_3+k_{-2})/k_2k_3[O_2] + 1/k_3\} \qquad (96)$$

Equations (95) and (96) are identical to equations (26) and (27) respectively.

Non-competitive and Mixed Zn^{2+} Inhibitions

Zn^{2+} binding:

$$Zn^{2+}\text{-}P \overset{K_1}{\rightleftarrows} Zn^{2+} + P \quad (97)$$

Fe^{2+} binding:

$$Fe^{2+} + P \underset{k_{-1}}{\overset{k_1}{\rightleftarrows}} Fe^{2+}\text{-}P \ (A1) \quad (98)$$

$$Fe^{2+} + Zn^{2+}\text{-}P \underset{k_{-1}'}{\overset{k_1'}{\rightleftarrows}} Zn^{2+}\text{-}P\text{-}Fe^{2+} \ (A1') \quad (99)$$

Dioxygen binding and 1st Fe^{2+} oxidation:

$$O_2 + Fe^{2+}\text{-}P \underset{k_{-2}}{\overset{k_2}{\rightleftarrows}} Fe^{2+}(O_2)P \ (A2)$$

$$\overset{k_3}{\rightarrow} Fe^{3+}(O_2^-)P \ (A3) \quad (100)$$

$$O_2 + Fe^{2+}\text{-}P\text{-}Zn^{2+} \underset{k_{-2}'}{\overset{k_2'}{\rightleftarrows}} Fe^{2+}(O_2)P\text{-}Zn^{2+} \ (A2')$$

$$\overset{k_3'}{\rightarrow} Fe^{3+}(O_2^-)P\text{-}Zn^{2+} \ (A3') \quad (101)$$

2nd Fe^{2+} binding/oxidation:

$$Fe^{3+}(O_2^-)P + Fe^{2+} \overset{k_4}{\rightarrow} Fe^{3+}(O_2^=)Fe^{3+}\text{-}P \ (A4)$$

$$\overset{k_5,\ H_2O}{\text{-------}\rightarrow} Fe^{3+}(O^=)Fe^{3+}\text{-}P \ (A5) + H_2O_2 \quad (102)$$

$$Fe^{3+}(O_2^-)P\text{-}Zn^{2+} + Fe^{2+} \overset{k_4'}{\rightarrow} Fe^{3+}(O_2^=)Fe^{3+}\text{-}P\text{-}Zn^{2+} \ (A4')$$

$$\overset{k_5',H_2O}{\text{--------}\rightarrow} Fe^{3+}(O^=)Fe^{3+}\text{-}P\text{-}Zn^{2+} \ (A5') + H_2O_2 \quad (103)$$

The following steady-state approximation equations

are combined to derive rate equation for the noncompetitive inhibition or mixed inhibition of Zn^{2+} on iron oxidation.

$$d[A1]/dt = k_1[Fe^{2+}][P]-k_{-1}[A1]-k_2[O_2][A1]+k_{-2}[A2] = 0 \quad (104)$$

$$d[A1']/dt = k_1'[Fe^{2+}][Zn^{2+}-P]-k_{-1}'[A1']-k_2'[O_2][A1'] + k_{-2}'[A2'] = 0 \quad (105)$$

$$d[A2]/dt = k_2[O_2][A1] - k_{-2}[A2] - k_3[A2] = 0 \quad (106)$$

$$d[A2']/dt = k_2'[O_2][A1'] - k_{-2}'[A2'] - k_3'[A2'] = 0 \quad (107)$$

$$d[A3]/dt = k_3[A2] - k_4[A3][Fe^{2+}] = 0 \quad (108)$$

$$d[A3']/dt = k_3'[A2'] - k_4'[A3'][Fe^{2+}] = 0 \quad (109)$$

$$d[A4]/dt = k_4[A3][Fe^{2+}] - k_5[A4] = 0 \quad (110)$$

$$d[A4]/dt = k_4'[A3'][Fe^{2+}] - k_5'[A4'] = 0 \quad (111)$$

From equations (108) and (110), we obtain

$$[A4] = (k_3/k_5)[A2] \approx 0 \qquad k_3 << k_5 \quad (112)$$

then combining equations (108), (110) and (112), we obtain

$$[A3] = (k_3[A2])/(k_4[Fe^{2+}]) \approx 0 \quad k_3 << k_4 \quad (113)$$

Similarly, equations (114) and (115) are obtained from equations (109) and (111).

$$[A4'] = (k_3'/k_5')[A2'] \approx 0 \qquad k_3' << k_5' \quad (114)$$

$$[A3'] = (k_3'[A2'])/(k_4'[Fe^{2+}]) \approx 0 \quad k_3' << k_4' \tag{115}$$

By combining equation (104) with (106), and (105) with (107), equation (116)-(119) are obtained under assumption of $k_{-2} >> k_3$, and $k_{-2}' >> k_3'$.

$$[A1] = K_1[Fe^{2+}][P] \tag{116}$$

$$[A1'] = K_1'[Fe^{2+}][Zn^{2+}-P] \tag{117}$$

$$[A2] = K_1K_2[Fe^{2+}][O_2][P] \tag{118}$$

$$[A2'] = K_1'K_2'[Fe^{2+}][O_2][Zn^{2+}-P] \tag{119}$$

where, $K_1 = k_1/k_{-1}$, $K_2 = k_2/k_{-2}$, $K_1' = k_1'/k_{-1}'$, and $K_2' = k_2'/k_{-2}'$. The rate of reaction is determined by the rate-limiting steps in the reaction mechanism II. Therefore,

$$\begin{aligned} V &= (1/2)(k_3[A2] + k_3'[A2']) \\ &= (1/2)\{k_3K_1K_2[Fe^{2+}][O_2][P] + k_3'K_1'K_2'[Fe^{2+}][O_2][Zn^{2+}-P] \\ &= (1/2)\left\{k_3K_1K_2 + \frac{k_3'K_1'K_2'[Zn^{2+}]}{K_1}\right\}[Fe^{2+}][O_2][P] \end{aligned} \tag{120}$$

$$[P_0] = [P] + [Zn^{2+}-P] + [A1] + [A2] + [A1'] + [A2']$$

$$\begin{aligned} [P] = P_0/\{&1 + [Zn^{2+}]/K_1 + K_1[Fe^{2+}] + \\ &K_1'[Zn^{2+}][Fe^{2+}]/K_1 + K_1K_2[O_2][Fe^{2+}] \\ &+ K_1'K_2'[Zn^{2+}][O_2][Fe^{2+}]/K_1\} \end{aligned} \tag{121}$$

Combining equations (120) and (121), we obtain equation (122) for the mixed-inhibition of Zn^{2+}.

$$1/V = 2/P_0[O_2]\cdot\left\{\frac{(1+[Zn^{2+}]/K_I)}{(A+B[Zn^{2+}]/K_I)[Fe^{2+}]} + \frac{C+D[Zn^{2+}]/K_I}{A+B[Zn^{2+}]/K_I}\right\} \quad (122)$$

where $A = k_3K_1K_2$, $B = k_3'K_1'K_2'$, $C = K_1(1 + K_2[O_2])$ and $D = (1 + K_2'[O_2])K_1'$.

Alternatively, substituting equation (121) into equation (120), and assuming $K_1 = K_1'$ and $K_2 = K_2'$, the rate equation for the noncompetitive Zn^{2+} inhibition is obtained.

$$V = \frac{(1/2)(k_3 + k_3'[Zn^{2+}]/KI)K_1K_2[Fe^{2+}][P_0][O_2]}{(1+[Zn^{2+}]/K_I) + (1+[Zn^{2+}]/K_I)(1+K_2[O_2])K_1[Fe^{2+}]} \quad (123)$$

$$1/V = (2/P_0K_1K_2)\left\{\frac{(1+[Zn^{2+}]/K_I)}{\alpha[Fe^{2+}]} + \frac{(1+[Zn^{2+}]/K_I)(1+K_2[O_2])K_1}{\alpha}\right\} \quad (124)$$

where $\alpha = (k_3 + k_3'[Zn^{2+}]/K_I)[O_2]$.

APPENDIX II

The following are the detailed experimental procedures for a typical freeze-quench experiment.

(1) Fill syringes with reactants. Two syringes with volumes of 0.5 ml and 2.0 ml are used in the kinetic experiments. Usually the smaller syringe (0.5 ml) contains Fe(II) solution, ranging from 10.0 mM to 2.0 mM, pH = 2, while the larger one (2.0 ml) contains 1.0 mM apoferritin in 0.1 M Mops buffer.

(2) Install the syringes on the up panel of the ram, and then attach the syringes to the mixer which is coupled to the aging hose, and finally the aging hose is connected to the spray nozzle.

(3) Set parameters on the front panel of ram controller, such as number of program, ram velocity, displacement of syringe plunger as well as delay time.

(4) Make an almost full dry ice-acetone slush. Cover it with a sponge-like cap and make a few holes of EPR tube size through the cap.

(5) Fill the inner tank with isopentane to the edge, and

then slowly pour about 2 to 3 liters of liquid N_2 through a funnel into the outer tank. Turn on the motor mounted on top of the inner tank to stir the isopentane.

(6) Monitor the temperature of isopentane using a copper-constant thermocouple, with one end of the thermocouple inside the isopentane and the other in ice water. The voltage measured on the detector can be converted to temperature according to a table listing the voltage-temperature correlation. Usually, temperature is kept around 135K.

(7) As the volume of isopentane decreases due to the lowered temperature, add more isopentane to the inner bath to maintain total volume. After the added liquid N_2 is completely vaporized, continue to add more of it to the outer bath, 1/2 liter at a time, until the required temperature was reached. Then, add about half liter liquid N_2 periodically to maintain the temperature.

(8) Attach a specially made EPR tube to a funnel using a piece of rubber tubing. Make the EPR tube as close as possible to the funnel **(Caution: don't break the funnel).** Fasten a piece of wire around the rubber tubing on the bottom of the funnel (this has been proved to be very successful to prevent the EPR tube from sliding off the funnel during the process of sample packing). Then insert

the EPR tube and funnel into the isopentane bath. Fill the funnel with clean isopentane. Top off from time to time as the isopentane in the funnel contracts.

(9) Take out the tube and funnel combination and hold it under the spray nozzle on the syringe ram.

(10) Execute the System 1000 program to mix the sample ad shoot it into the funnel.

(11) Return the tube and funnel to the isopentane bath.

(12) Immediately pack the frozen crystals in the bottom of the EPR tube with a pre-cooled packer. Push down a little bit of sample at each packing operation until a sample height of around 2 cm has been collected. Generally, this will require 5 to 10 times of the packing operation. The packing procedure needs a great deal of patience. Too hard or too soft packing will lead to incorrect changes in the EPR signal amplitudes. Therefore, one needs to apply strength as evenly as possible during each sample packing. Moreover, the hardness of packing also depends on the property of the crystals harvested. The characteristics of the crystals formed in each experiment varies with the chemical nature of the solution crystallized, the ram velocity, as well as the static electrical charge gained during freezing. The ionic strength and the nature of the

ions in the solution is very important in the success of crystal packing. For example, samples in 0.1 M Mops buffer is much easier to pack than those in 0.1 M NaCl. Usually, ram velocity can be chosen according to the instructions described in System 1000 operator's manual.

(13) After sample packing has been completed, remove funnel and tube combination from isopentane bath and insert the EPR tube in the dry ice slush through the hole in the sponge cap prepared in step (4).

(14) Disconnect the funnel from the EPR tube. This step is done by taking off the funnel from the rubber tubing (**Note: be careful not to break the funnel**).

(15) Evacuate the isopentane out of the frozen EPR tube using a normal mechanic pump for about 20 minutes.

(16) Attach a piece of quartz tube about 6 inches long to the EPR tube with an 1.5 inches long heat shrink tubing.

(17) Store the sample at -126 ^{0}C for later EPR measurement.